

Light Propagation in Optical Metamaterials – A Bloch Modal Approach –

Dissertation
zur Erlangung des akademischen Grades

doctor rerum naturalium (Dr. rer. nat.)

vorgelegt dem Rat der Physikalisch-Astronomischen-Fakultät
der Friedrich-Schiller-Universität Jena

von Diplom-Physiker Thomas Paul
geboren am 02.03.1979 in Saalfeld/Saale

1. **Gutachter:** Prof. Dr. Falk Lederer, Friedrich-Schiller-Universität Jena
2. **Gutachter:** Prof. Dr. Kurt Busch, Humboldt-Universität zu Berlin
3. **Gutachter:** Dr. Nicolae Coriolan Panoiu, University College London

Tag der öffentlichen Verteidigung: 15.03.2012

Contents

1	Introduction	3
1.1	Motivation	4
1.2	Aim and structure of this thesis	5
2	Numerical modeling of periodically arranged metamaterials	9
2.1	General statement of the problem	10
2.1.1	Maxwell's equations	11
2.1.2	Stack of periodically modulated layers	12
2.2	Fourier modal method	13
2.2.1	Bloch theorem and Fourier-Floquet eigenmodes	13
2.2.2	The scattering matrix	17
2.2.3	Solving for Bloch eigenmodes	18
2.3	Chapter summary and concluding remarks	20
3	Bulk metamaterials and Bloch eigenmodes	21
3.1	Orthogonality relations of Bloch modes	21
3.1.1	Decomposition of beams	25
3.2	The single interface between bulk metamaterials	26
3.2.1	General description	26
3.2.2	Fundamental mode approximation	29
3.3	Beam propagation in metamaterials	30
3.3.1	Inclination and diffraction coefficients	33
3.4	Chapter summary and concluding remarks	35
4	Investigation of bulky fishnet-like metamaterials	37
4.1	The fishnet structure	40
4.2	Frequency dispersion of a fishnet	42
4.3	Beam propagation in a fishnet	44
4.3.1	Iso-frequency contours of a fishnet	45
4.3.2	The fishnet slab and imaging of beams	48

4.3.3	Refraction of paraxial beams	56
4.4	Advanced metamaterials – the super-cell approach	59
4.4.1	A fishnet exhibiting a circular angular dispersion	61
4.4.2	A fishnet exhibiting a flat angular dispersion	64
4.5	Reflection and transmission at a planar interface	66
4.5.1	Interface between a homogeneous dielectric and a metamaterial . . .	67
4.5.2	Interface between two dissimilar metamaterials	74
4.6	Chapter summary and concluding remarks	77
5	Higher harmonic generation by plasmonic nanostructures	79
5.1	Statement of the problem	80
5.2	Extended Fourier modal method	83
5.2.1	The nonlinear source term	84
5.2.2	Solution within a single layer	85
5.2.3	The boundary conditions	86
5.3	Second-harmonic generation at a single-wire structure	88
5.4	Third-harmonic generation at a coupled plasmonic-dielectric structure	92
5.5	Chapter summary and concluding remarks	96
6	Summary and conclusion	98
	Acknowledgements	I
	Material parameters	III
	Zusammenfassung	VI
	Ehrenwörtliche Erklärung	VIII
	Publications	IX
	List of references	XVII

1 Introduction

The manipulation of the flow of light is intimately linked to the technological development of mankind and it has a strong and long-standing history over several centuries. Although, the usage of magnifying vision aids is already reported in antiquity [1], the initial point of modern optics is nowadays attributed to the work of the arabian scholar *Ibn-al-Haytham* [2]. He described the applicability of convex glass surfaces for the purpose of magnification. By that, he set the basis for the invention of spectacles (in the 13th century) or that of the telescope and microscope in the 17th century. Nowadays, optical technology has become indispensable for everyday life. Apart from genuine optical elements (such as lenses, lasers, etc.), especially artificially *structured materials* became very important, e.g. optical fibres, optical gratings, artificially generated holograms and photonic crystals; just to mention some of them. Such media have significantly affected the development of optics itself. Moreover, they have considerably contributed to the general technological development when thinking on, e.g., telecommunication, data-storage devices, semi-conductor industry (fabrication processes) and even medicine (modern imaging techniques), so their further development is an essential and continuous process.

In that sense, the rise of metamaterials (MMs) with the beginning of this millennium is the next leap forward in the development of artificially *structured materials*. The date of birth of MMs was mainly influenced by two different subjects. On the one hand, there was a seminal proposal by J. B. Pendry in the year 2000 [3] demonstrating the possibility to achieve a perfect lens (circumventing the diffraction limit) just by a slab of a homogeneous material exhibiting a relative permittivity ϵ and permeability μ of -1. At the same time, the great progress in nano-fabrication technologies has facilitated the manufacturing of tiny sub-wavelength artificial structures. Henceforth, these nano-fabrication technologies promised to open up a way to attain the building blocks (meta-atoms) for effective homogeneous media – essentially MMs – able to arbitrarily influence the electric (via the permittivity) as well as magnetic (via the permeability) response of the medium. Consequentially, the utilization of MMs promises to enter novel and previously foreign terrain in optics, because materials possessing a reasonable permeability (magnetic response) are not available in nature so far. As it was already pointed out by V. Veselago in the middle of the last

century [4], a negative permittivity and permeability give reason to a negative refractive index which amongst others results in the phenomenon of negative refraction. A few decades later, exactly these ideas were then recycled and further developed by J. B. Pendry in his proposal of the perfect lens as already mentioned above. This work produced a strong interest within the optical community and, henceforward, there was a strong increase in theoretical predictions about the potential applications of MMs. Particularly to note, the rich field of transformation optics [5–8] started to develop from that time resulting in new and interesting proposals such as the cloaking device [5,9–11] or even more general concepts to induce optical illusions [12–16]. Despite these ideas, the proposals for MMs have also penetrated into the field of nonlinear optics leading to interesting phenomena, e.g. counter-directed, phase-matched second-harmonic generation [17], counter-propagating entangled photons [18,19] or new conditions for the existence of solitons [20].

However, in trying to elaborate a clear classification of MMs, it appears to be best to return to the entire class of *structured materials*. Then, it must be recognized that a unique definition of MMs is rather impossible and even not suggested. Two examples shall be given to substantiate that statement. In case that the meta-atoms are arranged on a regular lattice, there appears a strong overlap to the field of photonic crystals [21,22] and a distinction is cumbersome. Second and to go even further, in case of thin layered MM films – up to now they are state-of-the-art – these devices may be simply considered as optical (multi-layer) gratings. However, a differentiation may be elaborated by the choice of the elementary building blocks (meta-atoms) as well as the effects/reponse one aims to achieve. In that sense, MMs rather rely on the unique electromagnetic response of a single meta-atom and do not explicitly rely on the collective response of the entire lattice (which is the case for photonic crystals). Consequentially, the used meta-atoms have to provide a strong dispersion of the electromagnetic response themselves. Today, metallic meta-atoms have become widely accepted by taking advantage of plasmon-polariton excitations. Along this route, MMs were already successfully demonstrated to work as hyperlenses [23,24], perfect absorbers [25], artificial blackbodies [26], negative-refracting materials [27,28], materials possessing a negative phase and group velocity [29] and even as flat lenses beating the diffraction limit [30,31]. Moreover, they were applied to mimic very effective chiral media resulting in a huge optical activity [TP00,32] or they were used to achieve asymmetric transmission [33].

1.1 Motivation

Since the beginnings of research on MMs roughly one decade ago, there was a continuous urge, maybe even a compulsion, to finally have effective homogeneous media at hand ex-

hibiting purposely designed material properties, i.e. $\epsilon(\omega)$ and $\mu(\omega)$. The dependence on the frequency ω accounts for a potential frequency dispersion; well known from ordinary, natural materials. Of course, this fact is mainly driven by the aforementioned proposals for extra-ordinary optical devices – all of them relying on the assumption that homogeneous MMs become available.

However, as already stated above, most contemporary MMs rely on resonant excitations of (intrinsically non-magnetic) metallic nano-structures, namely meta-atoms. In general, the extend of such meta-atoms is sub-wavelength. However, the typical ratio between the wavelength and the size of a meta-atom is considerably smaller than one order of magnitude; especially in the optical domain. Then, the assignment of effective material parameters, e.g. a permittivity and a permeability, that enter suitable macroscopic (averaged) Maxwell's equations (as a result of a homogenization process), comes at the cost of non-locality or spatial dispersion, respectively [34]. This means that the effective material response of a meta-atom is not only determined by the exciting field itself, but it rather depends on its derivatives, too. With respect to the effective material parameters, this entails an additional dependence on the wave-vector \mathbf{k} in general – a drawback which can be lifted only for very limited scenarios (so-called weak spatial dispersion). At first glance, this circumstance does not much matter, but with closer inspection there are some problems arising. They are mainly attributed to the boundary of a MM specimen, where the usual boundary conditions (continuity of the tangential electromagnetic field components) lose their validity. Then, the correct treatment of the boundary conditions becomes a serious problem with unambiguous solution [35]. Moreover, such a description would lose its connection to the initial purpose which is to make MMs available free of spatial dispersion, i.e. $\epsilon(\omega, \mathbf{k})$ and $\mu(\omega, \mathbf{k})$.

Regardless of the aforementioned problems, a reasonable approach which serves for the characterization of MMs remains one of the important topics. Consequentially, one may conclude that a more fundamental approach is needed to describe light interaction with MMs.

1.2 Aim and structure of this thesis

The following thesis exclusively concentrates on periodic MMs. Thus, the meta-atoms are located on a regular lattice; the prototypical situation for the arrangement of real atoms in natural crystals. It is the aim of this thesis to characterize and describe light propagation thoroughly on grounds of the *true* mesoscopic fields in these media without applying any conceptual approximation or better averaging to them, e.g. in terms of a homogenization approach. But, when speaking about the *true* mesoscopic fields, the question arises: What

are these fields, or better: What are the true mesoscopic eigenmodes of a periodic MM? The eigenmodes are Bloch modes and they fully reflect the precise structure and shape of the meta-atoms, so they account for the inhomogeneities that light experiences in such media*. This approach might be best understood with respect to photonic crystals. This is the prototypical example where light propagation is described in terms of Bloch eigenmodes and, to put it briefly, this approach exactly defines the framework of this thesis. However, losses are a key property of contemporary MMs. Thus, concepts developed in context of dielectric photonic crystals have to be modified such that they become generally applicable for MMs. Summarizing the guideline of this thesis, it deals with the thorough description and characterization of light propagation in and light scattering (reflection/transmission) at periodic, generally absorbing MMs in terms of a Bloch modal description[†]. This approach appears to be important and necessary especially in those cases when the characteristic size of the meta-atoms cannot be neglected in comparison with the wavelength of the exciting light field.

It is the aim of this thesis to deduce known and well-expected phenomena commonly attributed to MMs, like a left-handed behavior[‡] or negative refraction, solely from the properties of the Bloch eigenmodes of the considered media. Moreover, the differences to an effective medium description, particularly with respect to prospective observations, are highlighted whenever they appear and emphasis is put on their interpretation. In the light of the above explanations it might appear evident, that the studies of this work will rather rely on known and well-established MM layouts, than to come up with new proposals for their design. However, this does not imply that the present thesis is restricted to a pure characterization of known structures. On the one hand, the elaborated theoretical concepts are very general covering a broad range of applications and, on the other hand, it turns out that some of the known MM design concepts can be further adapted or optimized in the light of the presented theoretical treatment. In particular, the so-called fishnet structure and its derivations were chosen for explicit investigations because this class of MMs is well investigated in literature and it represents a low-loss medium with a left-handed behavior at optical frequencies.

*The term "mesoscopic" refers to the fact, that a structured medium is described by the spatial permittivity distribution of its constituents, i.e. $\epsilon(\omega, \mathbf{r})$, where all constituent materials are assumed to be local, homogeneous materials.

[†]At first glance, the term 'scattering' sounds very general in this context, but throughout this work it must be rather understood as the reflection and transmission of light at planar interfaces.

[‡]May \mathbf{k} , \mathbf{E} , \mathbf{H} and \mathbf{S} denote the wave-vector, the electric and magnetic field as well as the Poynting vector of a propagating plane wave (\mathbf{k} is real) in a certain homogeneous medium. Then, the term 'left-handed behavior' refers to the property, that the triple $\{\mathbf{k}, \mathbf{E}, \mathbf{H}\}$ establishes a left-handed trihedron, i.e. $\mathbf{k} \parallel \mathbf{S}$.

The present thesis is structured as follows. The introduction is followed by a brief summary of the precise and rigorous numerical modeling, as it was used for this work. In particular, the focus lies on the *Fourier modal method* (sometimes also referred as *rigorous coupled wave approach*) which allows for the calculation of the Bloch eigenmodes of three-dimensional, absorbing, periodic nano-structures. Right after that, the Bloch eigenmodes of an absorbing medium are thoroughly characterized in Chap. 3, where the deduced properties are independent on the scheme of their actual numerical determination. Instead, and that is important, they are generally applicable. At first, orthogonality relations are outlined which amongst others allow to specify the general decomposition of beams (propagating within a periodic medium) into Bloch modes. The orthogonality relations are further used in Sec. 3.2 to describe scattering at the interface between two dissimilar periodic media. By that, closed-form expressions are derived for the reflection and transmission coefficients of all modes excited at the interface. In this context, a very useful approximation, namely the *fundamental mode approximation* is introduced. It allows for a reasonable simplification of both problems, namely propagation through the bulk as well as coupling at the interfaces. Eventually, the chapter closes with the introduction of diffraction and inclination coefficients in Sec. 3.3. The first quantity is useful to describe the effective propagation characteristics of paraxial beams over macroscopic distances. The latter quantity is related to a beam's major direction of propagation and can be exploited to establish a law of refraction. In particular, it can be used to distinguish between positive (ordinary) and negative refraction.

In Chap. 4 the developed theoretical concepts are applied to realistic MMs. The focus will lie on fishnet MMs which are introduced in Sec. 4.1. Henceforth, reasonable paths through the dispersion relation of their Bloch eigenmodes are discussed and the consequences for beams propagating through the bulk are analyzed. At first, the frequency dispersion of the fishnet MM reveals a fundamental Bloch mode which exhibits a left-handed behavior. This observation agrees with precedent effective medium descriptions of the fishnet MM. However, the thorough analysis of the angular dispersion of that mode reveals that the left-handed behavior is largely disconnected and cannot be associated with anomalous diffraction and negative refraction in general. These findings are attributed to the strong (angular and frequency) dispersion of the fishnet structure and they are further supported by numerical experiments which study the imaging/focusing capabilities of properly designed fishnet MM slabs. To make the topic bold, Sec. 4.4 introduces a generic design approach of super-cell fishnet structures. With such approach, it is shown that the dispersion relation of the fundamental Bloch mode can be purposely tailored to match a predefined shape. Two examples demonstrate the achievement of a circular as well as a flat angular dispersion relation. The first one mimics that of a homogeneous, isotropic and left-handed MM, and

the second dispersion relation allows for the propagation of beams without experiencing any diffraction. Finally, the chapter closes with studies of reflection and transmission of Bloch modes at the planar boundary of a MM half-space. It is shown that a Swiss cross MM, which is appropriately diluted with respect to the longitudinal period, can be treated as homogenous while it still supports the dispersive effects of interest, i.e. a left-handed behavior.

Chapter 5 deals with the description and observation of nonlinear optical effects. There, the attention is devoted to the investigation of second and third-harmonic generation supported by metallic nano-structures. In this context, nonlinear frequency conversion processes are suggested to benefit from the high electrical field confinement in the vicinity of the metallic structures. In that sense, these schemes promise to outperform classical configurations for nonlinear frequency conversion, at first, with respect to the achievable efficiencies and, secondly, with respect to the effective interaction lengths. Last but not least, all results are summarized and perspectives are discussed.

2 Numerical modeling of periodically arranged metamaterials

The great progress in research and development of optical MMs during the last decade was mainly driven by the continuous evolution of nano-fabrication technologies, as there are, e.g., electron beam lithography [36] or focused ion beam milling [37]. Very recently, also new techniques are coming in sight which, e.g., try to construct MMs by means of self-organization mechanisms [38–42]. These so-called *bottom-up* MMs* most often possess low symmetries because they consist of randomly distributed meta-atoms and, hence, they possess amorphous characteristics up to a certain degree. Although the influence of disorder is worth studying from a fundamental point of view [43–47], rigorous electromagnetic calculations of large configurations of bottom-up MMs require the application of all-purpose numerical techniques. Usually, they discretize Maxwell’s equations in space and/or time. Examples that can be cited are the finite-difference time-domain method [48, 49], the finite-element method [50–52] or Galerkin methods [53, 54]. However, these methods typically require a huge amount of computational resources in memory and time, which makes them unfavorable to use. On the contrary, the so-called *top-down* MMs† designated to operate in the optical domain, originate from coated wafers whose surface is manipulated on a nanometer scale by the techniques mentioned above. Consequently, the desired meta-atoms are formed out of a thin stack of homogeneous layers and their arrangement can be controlled to a very large extent. In particular, choosing a periodic distribution of meta-atoms the entire structure will be determined by a single unit cell. However, the concrete spatial arrangement is considered to be of minor importance and the desired optical properties are still assumed to be controlled by the special shape of the unit cell (meta-atom) itself. Due to these reasons we will henceforth restrict all considerations to periodically arranged MMs since this is an important and widely investigated class of optical MMs. The concrete geometrical

*The term "bottom-up" accounts for the synthesis of this class of MMs. Typically, pre-fabricated or pre-processed meta-atoms are continuously deposited on a substrate such that the actual MM grows with time.

†The term "top-down" accounts for the fact, that these MMs are fabricated in a way typically starting from a pre-processed wafer, e.g. a stack of layers. Afterwards, the meta-atoms are developed by nano-structuring processes, e.g. electron beam lithography.

layout will be discussed in the upcoming section in more detail. However, with respect to the computational effort it would be desirable to have a numerical method at hand which exploits the basic symmetries (e.g. the periodicity) of the structure and takes advantage of it. Several rigorous methods exist for that purpose which have their roots in the rigorous analysis of light scattering and diffraction at optical gratings. Among others, there exist for example differential methods [55–59], integral methods [60–62], the C-method [63–65] and the finite element method [66]. Nevertheless, the most relevant method for this thesis is the Fourier modal method (FMM) which will be briefly reviewed in Sec. 2.2. It dates back to the beginnings of the eighties [67,68] and it was then continuously improved over the last two decades by stably analyzing three-dimensional and multi-layer structures [69–72], by establishing adapted Fourier factorization rules [73–78] and, eventually, by the introduction of adaptive spatial resolution [79–83] to improve the convergence. The usage of perfectly matched layers even allows for the modeling of non-periodic structures [84–87].

In this chapter the FMM is outlined for an application to periodic structures. It will be discussed how to use this method for the calculation of the optical response (reflection/transmission) of a finite thin film MM embedded in an arbitrary surrounding. Moreover, the FMM can be adapted to calculate the Bloch eigenmodes of a bulk MM. An approach to this treatment will be given in Sec. 2.2.3. Combining both possibilities finally allows for the rigorous calculation of the reflection and transmission coefficients between two dissimilar MMs. The chapter closes with a short summary to highlight the important elements.

Eventually, there is a short note which has to be provided with respect to the chosen nomenclature. Although this thesis is dedicated to light propagation in MMs, the methods presented in the following two chapters will also apply for all kinds of lossy, periodic structures. Thus, the methods can be applied to MMs (absorbing or not) as well as photonic crystals. Specific properties which are only attributed to a special class of these structures will be clearly stated if necessary.

2.1 General statement of the problem

Within this thesis all considerations are relying on classical, macroscopic electrodynamics. All constituent materials that are used to assemble a MM are assumed to be local, homogeneous and non-magnetic media. Hence, Maxwell’s equations together with meaningfully chosen constitutive relations provide the fundamental framework to describe classical optics. At first, all important quantities and equations are introduced in the current section. Furthermore, the most general geometrical layout for all further considerations will be discussed

and the basic notation, used in the succeeding sections, is clarified.

2.1.1 Maxwell's equations

Throughout the remaining part of this thesis all considerations are performed in the spectral domain. Then, Maxwell's equations, excluding free charges and currents, read as

$$\begin{aligned}\nabla \times \mathbf{E}(\mathbf{r}, \omega) &= +i\omega\mathbf{B}(\mathbf{r}, \omega) , & \nabla \cdot \mathbf{B}(\mathbf{r}, \omega) &= 0 , \\ \nabla \times \mathbf{H}(\mathbf{r}, \omega) &= -i\omega\mathbf{D}(\mathbf{r}, \omega) , & \nabla \cdot \mathbf{D}(\mathbf{r}, \omega) &= 0.\end{aligned}\quad (2.1)$$

The real and time dependent electrical field components can be calculated according to

$$\mathbf{E}(\mathbf{r}, t) = \int_0^{\infty} d\omega [\mathbf{E}(\mathbf{r}, \omega) \exp(-i\omega t) + \mathbf{E}^*(\mathbf{r}, \omega) \exp(+i\omega t)] \quad (2.2)$$

where the asterisk denotes the complex conjugate. Analogue relations hold for the fields \mathbf{D} , \mathbf{H} and \mathbf{B} , too. In what follows, the two curl-equations of Eqs. (2.1) are used to solve for the electromagnetic problem under consideration, however, keeping in mind the constraints implied by the two div-equations[‡].

The four electromagnetic fields contained within Maxwell's Eqs. (2.1) are not independent from each other and their mutual dependency comes into the game by the respective constitutive relations. In the following, we will consider only non-magnetic materials

$$\mathbf{B}(\mathbf{r}, \omega) = \mu_0\mathbf{H}(\mathbf{r}, \omega) \quad (2.3)$$

with μ_0 being the vacuum permeability. It has to be stressed that this assumption reflects the natural choice of available materials for optical frequencies but it can be easily lifted [88]. The dielectric response is considered to be

$$\mathbf{D}(\mathbf{r}, \omega) = \epsilon_0\epsilon(\mathbf{r}, \omega)\mathbf{E}(\mathbf{r}, \omega) \quad (2.4)$$

where all linear material properties are collected into the permittivity function $\epsilon(\mathbf{r}, \omega)$ and ϵ_0 denotes the permittivity of vacuum. The present chapter exclusively concentrates on light-matter interactions in the linear regime, however, in Chap. 5 also nonlinear optical properties of nano-structured materials will be discussed. Then, an additional term, namely the nonlinear polarization, has to be considered in Eqn. (2.4).

Now, by substituting Eqs. (2.3)-(2.4) into Eqs. (2.1), and introducing a re-normalized mag-

[‡]Owing to the relation $\nabla \cdot (\nabla \times) = 0$, the two div-equations are trivially fulfilled for frequencies $\omega > 0$.

netic field

$$\tilde{\mathbf{H}}(\mathbf{r}, \omega) = \sqrt{\mu_0/\epsilon_0} \mathbf{H}(\mathbf{r}, \omega) \quad (2.5)$$

we finally end up with ($k = \omega/c$)

$$\begin{aligned} \nabla \times \mathbf{E}(\mathbf{r}, \omega) &= +ik\tilde{\mathbf{H}}(\mathbf{r}, \omega), \\ \nabla \times \tilde{\mathbf{H}}(\mathbf{r}, \omega) &= -ik\epsilon(\mathbf{r}, \omega)\mathbf{E}(\mathbf{r}, \omega). \end{aligned} \quad (2.6)$$

Summing up, these equations will state the basis for all upcoming specifications of this chapter. The tilde placed above the magnetic field will be omitted in the following, henceforth assuming the exclusive usage of the re-normalized magnetic field.

2.1.2 Stack of periodically modulated layers

As already written in the chapter's introduction, in the following considerations the focus will be on periodic, stacked MMs. The fundamental geometrical layout is depicted in Fig. 2.1. In

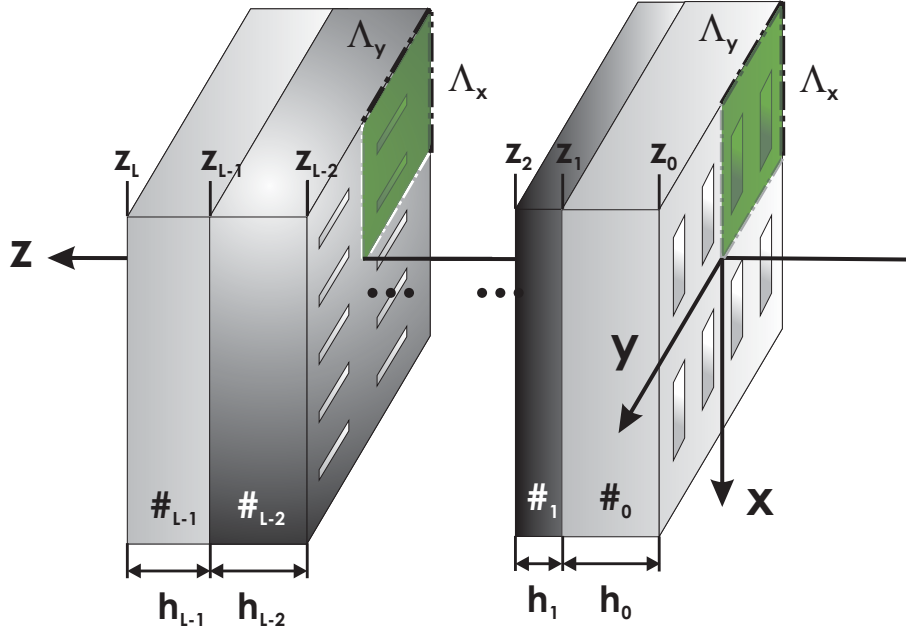


Figure 2.1: Schematic picture of a periodic multi-layer structure. In general, all included layers possess a periodic material distribution in lateral dimension (x - and y -direction). All layers have to share a common periodicity $\Lambda_x \times \Lambda_y$ which defines the unit cell in every layer (see green-shaded area). The permittivity distribution is invariant along the third spatial dimension (z) within a single layer. The height of each layer is arbitrary and denoted by h_l ; l is the layer index running from 0 to $L - 1$.

general, the entire structure is composed of an arbitrary number of layers. The constituent materials are considered to be isotropic such that the permittivity distribution ϵ is periodic

in x - and y -direction and it is assumed to be invariant with respect to the z -direction in each individual layer. The lateral (x - and y -direction) period, which has to be commensurable for all the layers, amounts to $\Lambda_x \times \Lambda_y$. The permittivity distribution is of the form $\epsilon^{(l)}(x, y) = \epsilon^{(l)}(x + \Lambda_x, y + \Lambda_y)$, with l being the layer index. The adjacent regions, formally subscripted by -1 and L , are not specified in detail at the moment. However, it has to be assumed that the field in these regions can be represented by a Fourier series, i.e. can be decomposed into plane waves.

2.2 Fourier modal method

The following section serves to present a brief summary of the Fourier modal method – a numerical technique that was widely used to achieve the results presented in this thesis. Its aim is to solve the electromagnetic boundary value problem for the geometrical layout as described in Sec. 2.1.2 in a rigorous manner.

2.2.1 Bloch theorem and Fourier-Floquet eigenmodes

Since the permittivity distribution is periodic with respect to the lateral dimensions in each layer of the structure, the Bloch theorem [89] can be applied to any electromagnetic field component, i.e.

$$f^{(l)}(x + \Lambda_x, y + \Lambda_y, z) = \exp [i(\alpha_0 \Lambda_x + \beta_0 \Lambda_y)] f^{(l)}(x, y, z). \quad (2.7)$$

Here, the quantity f is a placeholder for any Cartesian component of \mathbf{E} or \mathbf{H} , respectively. According to Eqn. (2.7), the field is called pseudo-periodic since it decomposes into a phase factor and into a purely lattice periodic component. α_0 and β_0 represent the lateral components of the *Bloch wave vector*, or shortly called the *Bloch vector* in the following. It has to be mentioned that α_0 and β_0 are conserved throughout all layers, the substrate and cladding which is a direct implication of the electromagnetic boundary conditions. Hence, the field inside every layer l can be expressed by the pseudo-Fourier series

$$f^{(l)}(x, y, z) \cong \sum_{m=-U_x}^{U_x} \sum_{n=-U_y}^{U_y} f_{mn}^{(l)}(z) \exp [i(\alpha_m x + \beta_n y)]. \quad (2.8)$$

An exact equality is achieved for U_x and U_y approaching infinity, but a numerical solution requires the Fourier series to be truncated. Furthermore,

$$\alpha_m = \alpha_0 + mK_x \quad (2.9)$$

$$\beta_n = \beta_0 + nK_y \quad (2.10)$$

with the reciprocal lattice vector components $K_x = 2\pi/\Lambda_x$ and $K_y = 2\pi/\Lambda_y$. The superscript l denotes the layer index. Inspecting Eqs. (2.8)-(2.10) it becomes clear that it suffices to restrict the lateral Bloch vector components α_0 and β_0 to the so-called *first Brillouin zone*[§] (BZ), i.e. $\alpha_0 \in [-K_x/2, +K_x/2)$ and $\beta_0 \in [-K_y/2, +K_y/2)$. Solutions which possess higher lateral Bloch vector components can always be mapped onto the BZ.

Eigenmodes of a single layer. Now, concentrating on Eqn. (2.8) and remembering that the permittivity distribution is invariant along the z -direction in any layer l , the eigensolutions will be of the following form:

$$f^{(l)}(x, y, z) = \exp(i\gamma^{(l)}z) \sum_{mn} f_{mn}^{(l)} \exp[i(\alpha_m x + \beta_n y)]. \quad (2.11)$$

Inserting Eqn. (2.11) into Maxwell's equations (2.6) and eliminating the z -components of the fields, one obtains an algebraic system of equations for the lateral electromagnetic field components [69, 75], that is

$$\gamma^{(l)} \mathbb{X}^{(l)} = \hat{M}^{(l)} \mathbb{X}^{(l)} = \begin{pmatrix} 0 & \hat{F}^{(l)} \\ \hat{G}^{(l)} & 0 \end{pmatrix} \begin{pmatrix} \mathbb{E}_\perp^{(l)} \\ \mathbb{H}_\perp^{(l)} \end{pmatrix}. \quad (2.12)$$

Here and in the following, quantities like \mathbb{X} denote vectors in Fourier domain. Equation (2.12) can be further simplified to become

$$(\gamma^{(l)})^2 \mathbb{E}_\perp^{(l)} = \hat{F}^{(l)} \hat{G}^{(l)} \mathbb{E}_\perp^{(l)} \quad (2.13)$$

Formally, Eqn. (2.12) is an eigenvalue equation with the eigenvalue $\gamma^{(l)}$ and the eigenvector

$$\mathbb{X}^{(l)} = (\mathbb{E}_\perp^{(l)}, \mathbb{H}_\perp^{(l)})^T = (\mathbb{E}_x^{(l)}, \mathbb{E}_y^{(l)}, \mathbb{H}_x^{(l)}, \mathbb{H}_y^{(l)})^T \quad (2.14)$$

with each of the four entries representing a column vector of the Fourier coefficients of the corresponding field components. Thus, e.g., the x -component of the electrical field $\mathbb{E}_x^{(l)}$ is a

[§]In what follows it is shortly called the *Brillouin zone*.

vector in Fourier domain itself and it reads as

$$(\mathbb{E}_x^{(l)})_{m+(2U_x+1)n} = E_{xmn}^{(l)} \quad (2.15)$$

Similar definitions hold for all other electromagnetic field components, too. The concrete definition of the sub-matrices $\hat{F}^{(l)}$ and $\hat{G}^{(l)}$ turns out to be [69] ($k = \omega/c$)

$$\hat{F}^{(l)} = \frac{1}{k} \begin{pmatrix} \hat{\alpha} \hat{\eta}^{(l)} \hat{\beta} & k^2 \mathbb{1} - \hat{\alpha} \hat{\eta}^{(l)} \hat{\alpha} \\ -k^2 \mathbb{1} + \hat{\beta} \hat{\eta}^{(l)} \hat{\beta} & -\hat{\beta} \hat{\eta}^{(l)} \hat{\alpha} \end{pmatrix} \quad (2.16)$$

$$\hat{G}^{(l)} = \frac{1}{k} \begin{pmatrix} -\hat{\alpha} \hat{\beta} & -k^2 \hat{\epsilon}_{yx}^{(l)} + \hat{\alpha} \hat{\alpha} \\ k^2 \hat{\epsilon}_{xy}^{(l)} - \hat{\beta} \hat{\beta} & \hat{\beta} \hat{\alpha} \end{pmatrix} \quad (2.17)$$

The matrices $\hat{\alpha}$ and $\hat{\beta}$ are diagonal matrices of size $(2U_x+1)(2U_y+1)$ containing the elements of α_m and β_n according to Eqs. (2.9)-(2.10) whereas $\mathbb{1}$ denotes the identity matrix of equal size.

Fourier factorization rules. Special care has to be taken with respect to the Fourier transformation of the permittivity distribution $\epsilon^{(l)}(\mathbf{r}, \omega)$. There exist special rules [74, 76] which drastically improve the convergence properties of the considered method with respect to the number of Fourier harmonics used for the numerical calculation. Without giving any explicit justification here, they affect the definition of the matrices $\hat{\eta}^{(l)}$, $\hat{\epsilon}_{xy}^{(l)}$ and $\hat{\epsilon}_{yx}^{(l)}$. To write down their definitions one furthermore has to define the Toeplitz matrices $\hat{\epsilon}_x^{(l)}(y)$ and $\hat{\epsilon}_y^{(l)}(x)$ which are composed of the following Fourier components

$$\epsilon_x^{(l)}(y)|_m = \frac{1}{\Lambda_x} \int_0^{\Lambda_x} dx \frac{1}{\epsilon^{(l)}(x, y)} \exp(-imK_x x) \quad (2.18)$$

$$\epsilon_y^{(l)}(x)|_n = \frac{1}{\Lambda_y} \int_0^{\Lambda_y} dy \frac{1}{\epsilon^{(l)}(x, y)} \exp(-inK_y y) \quad (2.19)$$

and, finally, one finds the desired quantities to be Toeplitz matrices formed by the following elements

$$(\eta^{(l)})^{-1}|_{mn} = \frac{1}{\Lambda_x \Lambda_y} \iint\limits_{0 \ 0}^{\Lambda_x \Lambda_y} dx dy \epsilon^{(l)}(x, y) \exp[-i(mK_x x + nK_y y)] \quad (2.20)$$

$$\epsilon_{xy}^{(l)}|_{mn} = \frac{1}{\Lambda_y} \int_0^{\Lambda_y} dy (\hat{\epsilon}_x^{(l)}(y))^{-1} \exp(-inK_y y) \quad (2.21)$$

$$\epsilon_{yx}^{(l)}|_{mn} = \frac{1}{\Lambda_x} \int_0^{\Lambda_x} dx (\hat{\epsilon}_y^{(l)}(x))^{-1} \exp(-imK_x x) \quad (2.22)$$

Field decomposition in a single layer. Now that all quantities entering Eqn. (2.13) are defined, the layers' eigensolutions according to Eqn. (2.11) are formally known. Thus, any field distribution within layer l can be written as a superposition of the corresponding eigensolutions (with $j = \{x, y\}$)

$$E_{j,mn}^{(l)} = \sum_{s=1}^S a_s^{(l)} E_{j,mn,s}^{(l)} \exp(i\gamma_s^{(l)} \tilde{z}) + b_s^{(l)} E_{j,mn,s}^{(l)} \exp(-i\gamma_s^{(l)}(\tilde{z} - h_l)) \quad (2.23)$$

$$H_{j,mn}^{(l)} = \sum_{s=1}^S a_s^{(l)} H_{j,mn,s}^{(l)} \exp(i\gamma_s^{(l)} \tilde{z}) - b_s^{(l)} H_{j,mn,s}^{(l)} \exp(-i\gamma_s^{(l)}(\tilde{z} - h_l)) \quad (2.24)$$

with $\tilde{z} = z - z_l$ denoting the relative z -coordinate and h_l the thickness of the respective layer. $S = 2(2U_x + 1)(2U_y + 1)$ represents the finite number of numerically calculated eigensolutions. $E_{j,mn,s}^{(l)}$ are the Fourier components of the eigenvectors according to Eqn. (2.13). Knowing them, the magnetic field components are calculated using Eqs. (2.12)-(2.13), i.e. $\mathbb{H}_{\perp,s}^{(l)} = \hat{G}^{(l)} \mathbb{E}_{\perp,s}^{(l)} / \gamma_s^{(l)}$. At present, $a_s^{(l)}$ and $b_s^{(l)}$ are unknown modal field amplitudes. They are obtained later by imposing the boundary conditions at the layers' interfaces which will be discussed in more detail in the next section.

Finally, it turns out to be advantageous due to later reasons to write down Eqs. (2.23)-(2.24) in a more compact form. By using the notation of Eqn. (2.15) to cast all Fourier components of the electromagnetic field into a single vector, then the above equations can be transformed into a matrix form, that is

$$\mathbb{X}^{(l)}(\tilde{z}) = \begin{pmatrix} \hat{E}_{\perp}^{(l)} & \hat{E}_{\perp}^{(l)} \\ \hat{H}_{\perp}^{(l)} & -\hat{H}_{\perp}^{(l)} \end{pmatrix} \begin{pmatrix} \hat{A}_{+}^{(l)}(\tilde{z}) & 0 \\ 0 & \hat{A}_{-}^{(l)}(\tilde{z}) \end{pmatrix} \begin{pmatrix} \mathbf{a}^{(l)} \\ \mathbf{b}^{(l)} \end{pmatrix} \equiv \hat{W} \hat{\phi}(\tilde{z}) \begin{pmatrix} \mathbf{a}^{(l)} \\ \mathbf{b}^{(l)} \end{pmatrix}. \quad (2.25)$$

$\mathbb{X}^{(l)}(\tilde{z})$ is defined according to Eqn. (2.14) and the component vector $(\mathbf{a}^{(l)}, \mathbf{b}^{(l)})^T$ is com-

posed of the elements of the modal expansion coefficients[¶]. The matrices $\hat{E}_\perp^{(l)}$ and $\hat{H}_\perp^{(l)}$ denote the (numerically) complete set of eigensolutions which are solutions to Eqn. (2.13). $\hat{A}_\pm^{(l)}(\tilde{z})$ denote diagonal matrices according to $\hat{A}_+^{(l)}(\tilde{z}) = \text{diag}\{\exp(i\gamma_s^{(l)}\tilde{z})\}$ and $\hat{A}_-^{(l)}(\tilde{z}) = \text{diag}\{\exp(-i\gamma_s^{(l)}[\tilde{z} - h_l])\}$. Finally, inspecting the right hand side of Eqn. (2.25), the matrix \hat{W} simply defines the eigenvector matrix which is solution to Eqn. (2.12) and the matrix $\hat{\phi}(\tilde{z})$ is the associated propagation kernel, which allows to propagate the field to any position \tilde{z} within the associated layer.

2.2.2 The scattering matrix

As already mentioned before, the modal field amplitudes $a_s^{(l)}$ and $b_s^{(l)}$ of all layers are still unknown, however, they are linked to each other by enforcing the tangential electromagnetic field components to be continuous at the layers' boundaries. A standard scattering matrix (S-matrix) scheme [70] will be used in the following to address this task. Thus, in a first step the self-consistent field evolution inside a specific layer l is considered which is subject to a given field distribution defined at the boundaries \tilde{z}_l and \tilde{z}_{l+1} of that layer. Solving the corresponding equations according to the incoming and outgoing modes one ends up with (x - and y -direction are the tangential ones)

$$\begin{aligned} \begin{pmatrix} \mathbf{a}^{(l+1)} \\ \mathbf{b}^{(l)} \end{pmatrix} &= \hat{\sigma}^{(l)} \begin{pmatrix} \mathbf{a}^{(l)} \\ \mathbf{b}^{(l+1)} \end{pmatrix}, \\ \hat{\sigma}^{(l)} &\equiv \begin{pmatrix} \hat{E}_\perp^{(l+1)} & -\hat{E}_\perp^{(l)} \\ \hat{H}_\perp^{(l+1)} & \hat{H}_\perp^{(l)} \end{pmatrix}^{-1} \begin{pmatrix} \hat{E}_\perp^{(l)} \hat{C}^{(l)} & -\hat{E}_\perp^{(l+1)} \hat{C}^{(l+1)} \\ \hat{H}_\perp^{(l)} \hat{C}^{(l)} & \hat{H}_\perp^{(l+1)} \hat{C}^{(l+1)} \end{pmatrix}. \end{aligned} \quad (2.26)$$

The matrix $\hat{C}^{(l)}$ denotes a diagonal matrix composed of the elements $\exp(i\gamma_s^{(l)}h_l)$, i.e. $\hat{C}^{(l)} = \hat{A}_+^{(l)}(h_l)$ as used in Eqn. (2.25). $\hat{\sigma}^{(l)}$ is the so-called scattering matrix of layer l . The scattering matrices of all individual layers can now be concatenated in a recursive manner. This results in the total scattering matrix of the overall structure. In general, the concatenation between two S-matrices $\hat{\sigma}^1$ and $\hat{\sigma}^2$ will be denoted by $\hat{\sigma}^1 \star \hat{\sigma}^2$ and it evaluates to

$$\begin{aligned} \hat{\sigma}^1 \star \hat{\sigma}^2 &= \begin{pmatrix} \hat{\sigma}_{11}^1 & \hat{\sigma}_{12}^1 \\ \hat{\sigma}_{21}^1 & \hat{\sigma}_{22}^1 \end{pmatrix} \star \begin{pmatrix} \hat{\sigma}_{11}^2 & \hat{\sigma}_{12}^2 \\ \hat{\sigma}_{21}^2 & \hat{\sigma}_{22}^2 \end{pmatrix} \\ &= \begin{pmatrix} \hat{\sigma}_{11}^2 (\mathbb{1} - \hat{\sigma}_{12}^1 \hat{\sigma}_{21}^1)^{-1} \hat{\sigma}_{11}^1 & \hat{\sigma}_{12}^2 + \hat{\sigma}_{11}^2 (\mathbb{1} - \hat{\sigma}_{12}^1 \hat{\sigma}_{21}^1)^{-1} \hat{\sigma}_{12}^1 \hat{\sigma}_{22}^1 \\ \hat{\sigma}_{21}^1 + \hat{\sigma}_{22}^1 (\mathbb{1} - \hat{\sigma}_{21}^2 \hat{\sigma}_{12}^2)^{-1} \hat{\sigma}_{21}^2 \hat{\sigma}_{11}^2 & \hat{\sigma}_{22}^1 (\mathbb{1} - \hat{\sigma}_{21}^2 \hat{\sigma}_{12}^2)^{-1} \hat{\sigma}_{22}^2 \end{pmatrix}. \end{aligned} \quad (2.27)$$

[¶]Actually, the vectors $\mathbf{a}^{(l)}$ and $\mathbf{b}^{(l)}$ are not referring to the Fourier domain, however, the same notation is used for them just for convenience.

Eventually, the outlined concatenation scheme together with the complete set of eigen-solutions according to Eqn. (2.13) allows for the rigorous electromagnetic treatment which arises for any specific excitation impinging from the surrounding onto the structure.

Finally, the strength and usefulness of the presented description with respect to the nature of the adjacent regions (indices -1 and L) defined in context of Fig. 2.1 shall be illustrated. Usually there are two half-spaces – the substrate (index: -1) and cladding (index: L) – assumed to be semi-infinitely extended in the z -direction. As long as the eigenmodes of these regions can be expanded into a pseudo-Fourier series, it is straightforward to incorporate them into the presented S-matrix scheme. In particular, the associated modal amplitudes are usually called reflection and transmission coefficients since they describe the decomposition of the reflected and transmitted fields propagating into the substrate and cladding, respectively. To give some examples, the simplest case is that of substrate and cladding being ordinary homogeneous materials. This is the typical setup of a multi-layer grating. In this case, the modes within substrate and cladding are plane waves. Several examples can be found throughout the literature, e.g. in Refs. [69, 80, 81]. A different scenario may include a semi-infinitely extended bulk periodic structure. In that case the eigenmodes of substrate and/or cladding are Bloch modes. This allows to calculate reflection and transmission coefficients at a boundary between air and a photonic crystal [90–94] or MM [TP01] or even between two distinct photonic crystal [95–97] or MM structures [TP02].

2.2.3 Solving for Bloch eigenmodes

Up to now, the FMM was only discussed to solve Maxwell’s equations for a given, finite (in z -direction) geometry which is excited by a known incident field. However, it can be furthermore exploited to solve for the Bloch eigenmodes of a three-dimensional bulk MM with a unit cell being composed of a stack of modulated layers. According to the considerations of the previous section (see Sec. 2.2.1) the Bloch eigenmodes will obey the Bloch theorem, that is

$$f(x + \Lambda_x, y + \Lambda_y, z + \Lambda_z) = f(x, y, z) \exp [i(\alpha_0 \Lambda_x + \beta_0 \Lambda_y + k_z \Lambda_z)].$$

Again, f represents any electromagnetic field component and it implies that the eigenmodes of a three-dimensional periodic structure decompose into a lattice periodic function which is multiplied by an exponential term. k_z denotes the z -component of the Bloch vector $\mathbf{k}_B = (\alpha_0, \beta_0, k_z)^T$. To calculate the Bloch modes explicitly, it is assumed in the following

that the S-matrix \hat{S} as defined by the relation

$$\begin{pmatrix} \mathbf{a}^{(L)} \\ \mathbf{b}^{(0)} \end{pmatrix} = \hat{S} \begin{pmatrix} \mathbf{a}^{(0)} \\ \mathbf{b}^{(L)} \end{pmatrix} = \begin{pmatrix} \hat{S}_{11} & \hat{S}_{12} \\ \hat{S}_{21} & \hat{S}_{22} \end{pmatrix} \begin{pmatrix} \mathbf{a}^{(0)} \\ \mathbf{b}^{(L)} \end{pmatrix}. \quad (2.28)$$

is known. It describes the overall scattering of a particular stack structure consisting of L layers. This stack is assumed to represent a single unit cell of an associated three-dimensional bulk MM. Thus, applying Bloch periodic boundary conditions to the electromagnetic field also in z -direction, Eqn. (2.28) will transform into [85, 86, 98–100]

$$\begin{pmatrix} \mathbf{a}^{(0)} \exp(ik_z \Lambda_z) \\ \mathbf{b}^{(0)} \end{pmatrix} = \begin{pmatrix} \hat{S}_{11} & \hat{S}_{12} \\ \hat{S}_{21} & \hat{S}_{22} \end{pmatrix} \begin{pmatrix} \mathbf{a}^{(0)} \\ \mathbf{b}^{(0)} \exp(ik_z \Lambda_z) \end{pmatrix} \quad (2.29)$$

After separating all terms, including the Bloch exponential, by bringing them on the right hand side will lead to [98]

$$\begin{pmatrix} \hat{S}_{11} & 0 \\ \hat{S}_{21} & -\mathbb{1} \end{pmatrix} \begin{pmatrix} \mathbf{a}^{(0)} \\ \mathbf{b}^{(0)} \end{pmatrix} = \exp(ik_z \Lambda_z) \begin{pmatrix} \mathbb{1} & -\hat{S}_{12} \\ 0 & -\hat{S}_{22} \end{pmatrix} \begin{pmatrix} \mathbf{a}^{(0)} \\ \mathbf{b}^{(0)} \end{pmatrix} \quad (2.30)$$

which represents a generalized eigenvalue problem with eigenvalues $\exp(ik_z \Lambda_z)$ and eigenvectors $(\mathbf{a}^{(0)}, \mathbf{b}^{(0)})^T$. In particular, the vector $(\mathbf{a}^{(0)}, \mathbf{b}^{(0)})^T$ collects the expansion coefficients of the actual Bloch modes in terms of the Fourier modes of the first layer (index: 0) of the structure. It has to be mentioned, that a successive application of the scattering matrix approach also allows for the calculation of all other expansion coefficients $(\mathbf{a}^{(1)}, \mathbf{b}^{(1)})^T$ to $(\mathbf{a}^{(L-1)}, \mathbf{b}^{(L-1)})^T$ of the remaining layers of the structure. Thus, the complete electromagnetic field distribution of all Bloch modes is determined. Anyway, performing further algebraic manipulations on Eqn. (2.30) it finally transforms into

$$\begin{pmatrix} \mathbb{1} & -\hat{S}_{12} \\ 0 & \hat{S}_{22} \end{pmatrix} \begin{pmatrix} \mathbf{a}^{(0)} \\ \mathbf{b}^{(0)} \end{pmatrix} = \frac{1}{1 + \exp(ik_z \Lambda_z)} \begin{pmatrix} \mathbb{1} + \hat{S}_{11} & -\hat{S}_{12} \\ \hat{S}_{21} & -\mathbb{1} - \hat{S}_{22} \end{pmatrix} \begin{pmatrix} \mathbf{a}^{(0)} \\ \mathbf{b}^{(0)} \end{pmatrix} \quad (2.31)$$

which is a more favorable representation with respect to a numerical solution [100] since the new eigenvalue $1/(1 + \exp(ik_z \Lambda_z))$ does not cause overflow ($\rightarrow \infty$) if the imaginary part of k_z becomes positive and large. However, concentrating on the physical results it is important to note that the solution of Eqn. (2.31) will provide the multi-branch dispersion relation

$$k_{p,z} = k_{p,z}(\alpha_0, \beta_0, \omega) \quad (2.32)$$

of the Bloch modes of the three-dimensional bulk MM. The z -component $k_{p,z}$ of the Bloch vector is complex in general and it will be called *propagation constant* in the following. It continuously depends on the (real) lateral Bloch vector components α_0 , β_0 and the frequency ω in a parametric manner^{||}. Furthermore, there exists an infinite but countable number of solutions, with respect to mode index p , but due to the numerical calculation the number of modes will always stay finite. However, an increasing number of eigenmodes (depending on their propagation constant) will converge against their real counterparts in the infinite set of solutions which can be controlled by the number of Fourier harmonics used for the numerical calculation [86].

2.3 Chapter summary and concluding remarks

This chapter was devoted to the brief presentation and description of the Fourier modal method. It allows to solve Maxwell's equations for stacked, periodic MMs and nano-structures on rigorous grounds. At first, it was discussed how to solve the electromagnetic scattering problem on a finite nano-structure, e.g., to determine the reflection and transmission coefficients under illumination from the surrounding. In a second part and even more important, it was shown how to use the FMM to determine the band structure or dispersion relation $k_{p,z}(\alpha_0, \beta_0, \omega)$ as well as the associated Bloch modes of any periodic nano-structure. In particular, this includes three-dimensional, periodic and absorbing MMs. For that aim one principally is able to scan the entire parameter space defined by $\{(\alpha_0, \beta_0) \in \text{BZ}, \omega \in [0, \infty]\}$ with BZ denoting the Brillouin zone. However, the complete numerical procedure (including eigenvalue solvers and matrix inversions) has to be applied for each set of parameters $(\alpha_0, \beta_0, \omega)$ individually, such that these calculations are not feasible and practically all considerations will be restricted to some reasonable subspaces, e.g. iso-frequency surfaces (keeping the frequency constant) or frequency dispersion relations with respect to a fixed lateral direction (fixing α_0 and β_0).

^{||}Note that this treatment is different from the one that is used for photonic crystals [101] where the frequency obeys a multi-branch dispersion relation according to $\omega = \omega_n(\mathbf{k}_\perp, k_z)$.

3 Bulk metamaterials and Bloch eigenmodes

In the upcoming chapter we want to change the perspective away from the numerics towards a more or less abstract view on the problem of eigenmodes of MMs. The results of this chapter were already partly published in Ref. [TP03] and a more comprehensive survey will be presented here. In the following it is not important which method was used to determine the Bloch modes of a periodic MM. Instead, all consideration will exclusively rely on their pseudo-periodicity and some very fundamental material properties, like reciprocity. In the first part of this chapter it will be shown that the Bloch modes of absorbing MMs are orthogonal to each other and the associated orthogonality relations will be derived. These results are fundamental [TP03] and they represent a modification or extension of what is already known from dielectric periodic media, e.g. photonic crystals [21]. In the second part of the chapter the derived orthogonality relations are then exploited, e.g, to describe propagation within bulk MMs and to describe the scattering (reflection/transmission) of light at the boundary between two MM half-spaces in general.

3.1 Orthogonality relations of Bloch modes

In the following, an arbitrary periodic MM will be considered. Light propagation can be described in terms of its complete set of eigenmodes. Formally using Dirac's notation, any Bloch mode

$$|B_p(\alpha_0, \beta_0, \omega)\rangle \equiv (E_{p,x}, E_{p,y}, H_{p,x}, H_{p,y})^T \exp [i(\alpha_0 x + \beta_0 y + k_{p,z}(\alpha_0, \beta_0, \omega)z)] \quad (3.1)$$

can be characterized by a pseudo-periodic ket-vector being composed of an exponential term and the lattice periodic vector $(E_{p,x}, E_{p,y}, H_{p,x}, H_{p,y})^T$ which contains all lateral electromagnetic field components. In general, the *propagation constant* $k_{p,z}(\alpha_0, \beta_0, \omega)$ is complex and it parametrically depends on the lateral *Bloch vector* components as well as on the frequency. Although not explicitly written down, every field component depends on

$(\alpha_0, \beta_0, \omega)$, too. Finally, the complete spatiotemporal evolution of the p -th mode is given by $|B_p(\alpha_0, \beta_0, \omega)\rangle \exp(-i\omega t)$. Furthermore, all considerations will be restricted to light propagation with respect to the $\pm z$ -direction. Therefore, α_0 and β_0 must be real quantities to keep the modes finite at infinity.

In the following, general orthogonality relations between the Bloch modes of a medium are derived. The starting point is the set of Maxwell's equations according to Eqs. (2.6).

Inner product between Bloch modes. Relying on Dirac's notation, one can define a generalized inner product according to [90]

$$\langle B_q^\dagger | B_p \rangle = \iint_{-\infty}^{\infty} dx dy \Psi \cdot \mathbf{e}_z \exp \{i[(\alpha_0 + \alpha_0^\dagger)x + (\beta_0 + \beta_0^\dagger)y + (k_{q,z}^\dagger + k_{p,z})z]\}, \quad (3.2)$$

$$\Psi(\alpha_0, \beta_0, \alpha_0^\dagger, \beta_0^\dagger; x, y, z) \equiv [\mathbf{E}_p \times \mathbf{H}_q^\dagger - \mathbf{E}_q^\dagger \times \mathbf{H}_p].$$

between two Bloch modes $|B_p\rangle \equiv |B_p(\alpha_0, \beta_0, \omega)\rangle$ and $|B_q^\dagger\rangle \equiv |B_q(\alpha_0^\dagger, \beta_0^\dagger, \omega)\rangle$ obeying Maxwell's equations at the same frequency ω . For the sake of brevity, the frequency argument will be omitted in the following. \mathbf{e}_z denotes the Cartesian unit vector in z -direction. The introduced inner product may depend on the precise z -position of the plane where the integral is evaluated. However, $\langle B_q^\dagger | B_p \rangle$ turns out to be invariant with respect to the z -coordinate as will be shown later. Since only the z -component Ψ_z enters Eqn. (3.2), the remaining components will be omitted in the following. To derive the orthogonality relations one has to remember that Ψ_z is by definition a lattice periodic function that can be expanded into a Fourier series with respect to the x - and y -direction, namely $\Psi_z = \sum_{m,n=-\infty}^{\infty} \Psi_{mn}(\alpha_0, \beta_0, \alpha_0^\dagger, \beta_0^\dagger; z) \exp[i(K_x m + K_y n)]$. The expansion coefficients are denoted by Ψ_{mn} . They explicitly depend on the z -coordinate and, thus, Eqn. (3.2) transforms into

$$\langle B_q^\dagger | B_p \rangle = (2\pi)^2 \sum_{m,n=-\infty}^{\infty} \left\{ \Psi_{mn}(\alpha_0, \beta_0, \alpha_0^\dagger, \beta_0^\dagger; z) \delta(K_x m + \Delta\alpha_0) \delta(K_y n + \Delta\beta_0) \exp[i(k_{q,z}^\dagger + k_{p,z})z] \right\} \quad (3.3)$$

with $\Delta\alpha_0 = \alpha_0 + \alpha_0^\dagger$ and $\Delta\beta_0 = \beta_0 + \beta_0^\dagger$. The sum in Eqn. (3.3) seems to be rather involved, but only one element turns out to be non-zero.

Reduced inner product. To see this, one has to remember that $(\alpha_0, \beta_0)^T$ and $(\alpha_0^\dagger, \beta_0^\dagger)^T$ are elements of the BZ. Excluding the case that both modes are directly located at the edge of the BZ it can be concluded that $|\Delta\alpha_0| < K_x$ and $|\Delta\beta_0| < K_y$. Therefore, only the central

element $(m, n = 0)$ of Eqn. (3.3) is non-zero which leads to

$$\begin{aligned} \langle B_q(\alpha_0^\dagger, \beta_0^\dagger) | B_p(\alpha_0, \beta_0) \rangle &= (2\pi)^2 \Psi_{00} \delta(\Delta\alpha_0) \delta(\Delta\beta_0) \exp[i(k_{q,z}^\dagger + k_{p,z})z] \\ &\equiv \{B_q(\alpha_0^\dagger, \beta_0^\dagger) | B_p(\alpha_0, \beta_0)\} \delta(\Delta\alpha_0) \delta(\Delta\beta_0) \end{aligned} \quad (3.4)$$

where the reduced inner product $\{B_q^\dagger | B_p\}$ was introduced according to

$$\{B_q^\dagger | B_p\} = \frac{(2\pi)^2}{\Lambda_x \Lambda_y} \iint_{\text{unit cell}} dx dy \Psi \cdot \mathbf{e}_z \exp[i(k_{q,z}^\dagger + k_{p,z})z]. \quad (3.5)$$

The pre-factor is chosen for convenience to avoid additional constants in Eqn. (3.4). The reduced inner product is very similar to the original one according to Eqn. (3.2), but it is only evaluated over the cross section of a single unit cell. Thus, the integral will remain finite in general. From a numerical point of view these facts are very essential since they allow to work on finite intervals.

Orthogonality with respect to \mathbf{k}_\perp . *En passant*, Eqn. (3.4) is already half of the story with respect to the orthogonality of modes. It indicates that two Bloch modes $|B_p(\alpha_0, \beta_0)\rangle$ and $|B_q(\alpha_0^\dagger, \beta_0^\dagger)\rangle$ are orthogonal to each other whenever $(\alpha_0, \beta_0)^T \neq -(\alpha_0^\dagger, \beta_0^\dagger)^T$, or in other words, if they do not share a lateral Bloch vector component which is opposite in sign. Moreover, the orthogonality relations according to Eqn. (3.4) will also hold between modes of different media as long as their periods in lateral direction, i.e. $\Lambda_x \times \Lambda_y$, are equal. This is caused by the fact that the permittivity distribution does not explicitly enter the derivation of Eqn. (3.4) and, instead, only the pseudo-periodicity of the eigenmodes was exploited.

Law of conservation. Now, after having evaluated the generalized inner product $\langle B_q^\dagger | B_p \rangle$ with respect to its dependency on the lateral Bloch vector components α_0 and β_0 , the influence of the discrete mode indices, namely q and p is still unidentified. Relying on the Lorentz reciprocity theorem [102] one can derive the following expression [90]

$$\begin{aligned} \iint_{\partial V} (\tilde{\mathbf{E}}_2 \times \tilde{\mathbf{H}}_1 - \tilde{\mathbf{E}}_1 \times \tilde{\mathbf{H}}_2) \cdot d\mathbf{S} = \\ \frac{i}{c} (\omega_1 - \omega_2) \iiint_V (\epsilon \tilde{\mathbf{E}}_1^T \tilde{\mathbf{E}}_2 - \tilde{\mathbf{H}}_1^T \tilde{\mathbf{H}}_2) dV. \end{aligned} \quad (3.6)$$

It is fulfilled for $\tilde{\mathbf{E}}_1$ and $\tilde{\mathbf{H}}_1$ ($\tilde{\mathbf{E}}_2$ and $\tilde{\mathbf{H}}_2$), representing the electric and magnetic field vectors of any monochromatic field distribution obeying Maxwell's equations (2.6) within the same

medium $\epsilon(\mathbf{r}, \omega)$ at frequency ω_1 (ω_2). For isotropic constituents, i.e. $\epsilon(\mathbf{r}, \omega)$ is a scalar function, no further assumption is necessary* to derive Eqn. (3.6).

In what follows, Eqn. (3.6) is applied to the eigenmodes $|B_q^\dagger\rangle = |B_q(-\alpha_0, -\beta_0, \omega)\rangle$ and $|B_p\rangle = |B_p(\alpha_0, \beta_0, \omega)\rangle$. Of course, the parameters are chosen such that $|B_q^\dagger\rangle$ and $|B_p\rangle$ are non-orthogonal in the sense of Eqn. (3.4). Now, the special case of a cuboidal volume V with lower and upper limits z and $z+z_0 > z$ is considered. In lateral direction V is extended over a single unit cell and, hence, the integration kernel is periodic in x and y . Due to this fact, the surface integral in Eqn. (3.6) collapses and there are only two surfaces at z and $z+z_0$ with a non-vanishing contribution. Furthermore, the right hand side of Eqn. (3.6) is zero, because both modes have the same frequency. Then, using the reduced inner product according to Eqn. (3.5), Eqn. (3.6) transforms into

$$\{B_q^\dagger|B_p\}_{z+z_0} - \{B_q^\dagger|B_p\}_z = 0. \quad (3.7)$$

It is immediately clear that $\{B_q^\dagger|B_p\}$, and consequently also $\langle B_q^\dagger|B_p\rangle$, do not depend on z explicitly. Hence, $\langle B_q^\dagger|B_p\rangle$ is a conserved quantity, although the Bloch modes entering this equation generally do experience an attenuation during propagation along z . Moreover, due to the fact that the concept of a group velocity is questionable in lossy media the authors of Ref. [103] use the cited quantity, namely $\{B_q^\dagger|B_p\}$, to define a so-called adjoint field velocity for modes in lossy periodic structures. This modal field velocity then turns out to reproduce the energy velocity in case of a lossless dielectric.

Orthogonality with respect to \mathbf{k}_z . By explicitly evaluating Eqn. (3.7) for $z_0 = \Lambda_z$ and exploiting the quasi-periodicity of the Bloch modes along the z -direction it follows that

$$\{B_q^\dagger|B_p\} \{1 - \exp [i(k_{p,z} + k_{q,z}^\dagger)\Lambda_z]\} = 0. \quad (3.8)$$

This equation is obviously fulfilled whenever at least one of these two terms equals zero. The latter one only vanishes whenever $k_{p,z} + k_{q,z}^\dagger = 0$. To identify these cases, the general relation between the propagation constants of modes $|B_q^\dagger\rangle$ and $|B_p\rangle$ provides the answer. The propagation constants are related by $k_{q,z}^\dagger = -k_{q,z}$ as deduced from the most general property

$$\mathbf{k}_{B,p}^\dagger = -\mathbf{k}_{B,p} \quad (3.9)$$

which is essential and only applies in reciprocal media [103, 104]. Using Eqn. (3.9) and assuming that there are only non-degenerated modes, i.e. $k_{p,z} \neq k_{q,z}$ for $p \neq q$, Eqn. (3.8)

*A very similar relation is valid for any anisotropic medium as long as it is reciprocal, i.e. $\epsilon(\mathbf{r}, \omega) = \epsilon^T(\mathbf{r}, \omega)$. The Bloch mode orthogonality relations will even hold in this more general case.

directly implies that

$$\{B_q(-\alpha_0, -\beta_0)|B_p(\alpha_0, \beta_0)\} \propto \delta_{pq} \quad (3.10)$$

with δ_{pq} being the Kronecker symbol. This relation together with Eqn. (3.4) gives the final result

$$\langle B_q(\alpha_0^\dagger, \beta_0^\dagger)|B_p(\alpha_0, \beta_0)\rangle = C_p(\alpha_0, \beta_0)\delta_{pq}\delta(\alpha_0 + \alpha_0^\dagger)\delta(\beta_0 + \beta_0^\dagger) \quad (3.11)$$

being the orthogonality relations of Bloch modes in an arbitrary and, in particular, absorbing MM. The set of functions

$$C_p(\alpha_0, \beta_0) = \{B_p(-\alpha_0, -\beta_0)|B_p(\alpha_0, \beta_0)\}$$

allows for an arbitrary normalization. Finally, having a closer look at the definition of the bilinear form $\{B_q(\alpha_0^\dagger, \beta_0^\dagger)|B_p(\alpha_0, \beta_0)\}$ according to Eqn. (3.5), it gets obvious that it is antisymmetric with respect to its elements, i.e. $\{B_q(\alpha_0^\dagger, \beta_0^\dagger)|B_p(\alpha_0, \beta_0)\} = -\{B_p(\alpha_0, \beta_0)|B_q(\alpha_0^\dagger, \beta_0^\dagger)\}$. Consequently, the scaling function will reflect this symmetry such that $C_p(\alpha_0, \beta_0) = -C_p(-\alpha_0, -\beta_0)$.

3.1.1 Decomposition of beams

After having derived the orthogonality relations obeyed by the Bloch modes of a particular MM, it is straightforward to decompose any field distribution $|F\rangle(x, y)$ into a superposition of Bloch modes. Therefore, one has to assume that the Bloch modes are complete such that any field $|F\rangle(x, y)$, measured at a certain z -position, may be written as[†]

$$|F\rangle(x, y) = \sum_p \iint_{\text{BZ}} d\alpha_0 d\beta_0 A_p(\alpha_0, \beta_0) |B_p(\alpha_0, \beta_0)\rangle(x, y, z), \quad (3.12)$$

with $A_p(\alpha_0, \beta_0)$ denoting the expansion coefficients, i.e. the Bloch spectrum. Projecting Eqn. (3.12) onto $\langle B_q(\alpha_0^\dagger, \beta_0^\dagger)|$ and using Eqn. (3.11) it immediately follows that

$$A_p(\alpha_0, \beta_0) = \frac{\langle B_p(-\alpha_0, -\beta_0)|F\rangle}{C_p(\alpha_0, \beta_0)}. \quad (3.13)$$

At first glance, it appears to be quite surprising that the spectral amplitude for a certain set of parameters (α_0, β_0) is determined by the Bloch mode associated with those parameters

[†]Note that a notation like $|B(\alpha_0, \beta_0)\rangle$ (with parenthesis *inside*) refers to a parametrical dependence of the ket-vector on the considered parameter. On the contrary, if the parenthesis are placed *outside*, e.g. $|F\rangle(x, y)$ or $|F\rangle(k_x, k_y)$, then this notation refers to the domain in which the considered quantity is evaluated.

that are opposite in sign. However, Eqs. (3.12)-(3.13) are quite similar to the expansion of any field distribution into plane waves propagating in a homogeneous medium. There, the expansion coefficient to a specific plane wave, say $\exp[i(\mathbf{k}_\perp \mathbf{r} + k_z z)]$, with lateral wave-vector component \mathbf{k}_\perp is given by a Fourier integral [105]. However, this is nothing else than the projection of the field onto that eigenmode which has a lateral wave-vector in opposite direction, namely $\exp(-i\mathbf{k}_\perp \mathbf{r})$.

3.2 The single interface between bulk metamaterials

Detrimental for a description of finite MMs, e.g. a MM slab structure, is the possible excitation of a larger number of Bloch modes at its interfaces. Then, the coupling of light into the MM is a complicated issue and requires a devoted rigorous treatment on its own [100, 106]. In the current section we will rely on the data presented in Sec. 3.1 and we will outline a description based on the Bloch modes of both MMs which helps to calculate the mutual scattering coefficients, i.e. the reflection and transmission coefficients, at a planar interface. Furthermore, it will turn out to be highly desirable to simplify this treatment and, preferably, to extract the coupling properties at a MM interface only from a single Bloch mode – particularly the one that also dominates the light propagation in the bulk. Along these lines we have shown in two recent publications that coupling between two media is governed by a single mode in both media, as long as the involved eigenmodes are only slightly perturbed with respect to each other [TP02, TP03].

3.2.1 General description

The very general problem of coupling light at the interface between two MMs \mathcal{L} (left) and \mathcal{R} (right) under oblique incidence is depicted in Fig. 3.1. For the sake of convenience, we will consider two MMs of equal periodicity with respect to the interface. This ensures, that a mutual cross coupling between both media only occurs for those Bloch modes which possess the same lateral (tangential) Bloch vector component. A generalization to the case of two different periods is straightforward in general, but turns out to be quite cumbersome. Then, the lateral Bloch vector component is conserved except for a multiple of the reciprocal interface lattice vector of the common period as it is known, e.g., for photonic crystals [106–110]. In the current configuration the eigenmodes on both sides of the interface are Bloch modes with a temporal dependency according to $\exp(-i\omega t)$ with a real frequency ω . Due to the orientation of the interface as depicted in Fig. 3.1 the lateral Bloch vector components $\mathbf{k}_\perp = (\alpha_0, \beta_0)^T$ must be chosen to be equally real to maintain the fields finite

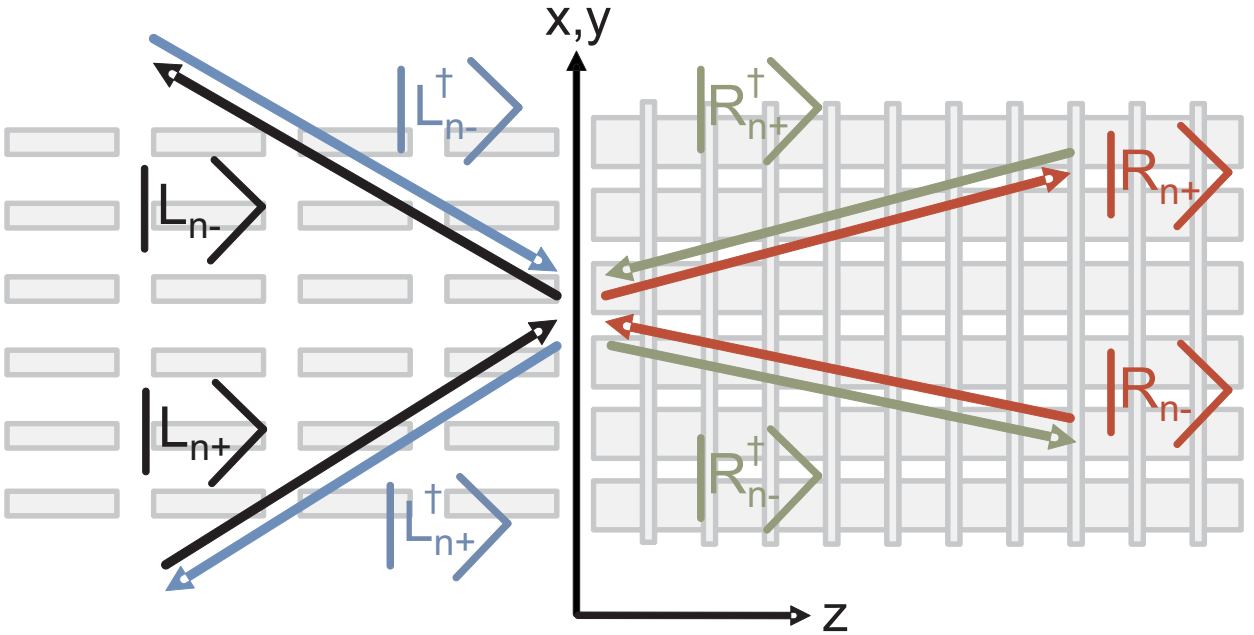


Figure 3.1: Schematic picture of an interface between two periodic media. The Bloch vector components tangential to the interface that are preserved are $(\alpha_0, \beta_0)^\top$ and $(-\alpha_0, -\beta_0)^\top$ for the adjoint (\dagger) fields, respectively.

at infinity. Hence, the propagation constant $k_{n,z} = k_{n,z}(\alpha_0, \beta_0, \omega)$ will be complex in general and it is determined by the particular dispersion relation of the respective medium. In what follows, Dirac's notation is used again. Thus, any Bloch mode is represented by its propagation constant $k_{n,z}$ and the associated ket-vector

$$|B_n\rangle = (E_{n,x}, E_{n,y}, H_{n,x}, H_{n,y})^T \exp[i(\alpha_0 x + \beta_0 y + k_{n,z} z)].$$

On either side of the interface (medium \mathcal{L} is discussed in the following) Fig. 3.1 shows four discrete set of modes. Two of them, i.e. $|L_{n+}\rangle$ and $|L_{n-}\rangle$, are solutions to a certain set of parameters, say $(\mathbf{k}_\perp, \omega)$. Furthermore, $|L_{n+}\rangle$ represents the modes with an energy flow in positive z -direction (in passive, absorbing materials they fulfill $\Im(k_{n,z}) > 0$) and $|L_{n-}\rangle$ are those with an energy flow in negative z -direction ($\Im(k_{n,z}) < 0$). On the other hand, the adjoint fields $|L_{n+}^\dagger\rangle$ and $|L_{n-}^\dagger\rangle$ are solutions to a different lateral Bloch vector $(-\mathbf{k}_\perp^\dagger, \omega)$. Please note, in contrast to the previous case, that forward and backward modes are now indicated by "–" and "+", respectively. After finishing the classification of all relevant modes the orthogonality relations according to Eqn. (3.11) can be used to write down the

following expressions [TP03], i.e.

$$\langle L_{m+}^\dagger | L_{n+} \rangle = L_m^+(\mathbf{k}_\perp) \delta_{mn} \delta(\mathbf{k}_\perp - \mathbf{k}_\perp^\dagger), \quad (3.14)$$

$$\langle L_{m-}^\dagger | L_{n-} \rangle = -L_m^-(\mathbf{k}_\perp) \delta_{mn} \delta(\mathbf{k}_\perp - \mathbf{k}_\perp^\dagger), \quad (3.15)$$

$$\langle L_{m+}^\dagger | L_{n-} \rangle = 0, \quad (3.16)$$

$$\langle L_{m-}^\dagger | L_{n+} \rangle = 0. \quad (3.17)$$

$L_m^\pm = \pm \{L_{m\pm}^\dagger | L_{m\pm}\}$ are normalization functions (please, refer to Eqn. (3.5) for the definition of the reduced inner product $\{L_{m\pm}^\dagger | L_{m\pm}\}$) and the minus sign in Eqn. (3.15) is just chosen for convenience. Similar results are valid for the mutual dependency of modes from medium \mathcal{R} using different normalization constants R_m^\pm in general. Furthermore, considering the mutual cross-dependency between the modes of media \mathcal{L} and \mathcal{R} and following the discussion in Sec. 3.1 one can directly conclude that

$$\langle R_{m+}^\dagger | L_{n+} \rangle = \{R_{m+}^\dagger | L_{n+}\} \delta(\mathbf{k}_\perp - \mathbf{k}_\perp^\dagger), \quad (3.18)$$

$$\langle R_{m-}^\dagger | L_{n-} \rangle = \{R_{m-}^\dagger | L_{n-}\} \delta(\mathbf{k}_\perp - \mathbf{k}_\perp^\dagger), \quad (3.19)$$

$$\langle R_{m+}^\dagger | L_{n-} \rangle = 0, \quad (3.20)$$

$$\langle R_{m-}^\dagger | L_{n+} \rangle = 0 \quad (3.21)$$

must be fulfilled as long as the two MMs possess the same cross section period at the common interface. In the more general case multiple δ -functions appear, which would potentially lead to a coupling between modes of different lateral Bloch vector components (as already mentioned above).

Without loss of generality it is assumed in the following that the incident light is impinging from the left hand side onto the interface. Furthermore, the incident field is assumed to be represented by any superposition of modes $|L_{n+}(\mathbf{k}_\perp)\rangle$. Due to the boundary, there are modes $|L_{n-}(\mathbf{k}_\perp)\rangle$ and $|R_{n+}(\mathbf{k}_\perp)\rangle$ excited in reflection as well as in transmission. Then, the continuity of the tangential electromagnetic field components at the interface implies that

$$\sum_n \int_{\text{BZ}} d\mathbf{k}_\perp i_n(\mathbf{k}_\perp) |L_{n+}(\mathbf{k}_\perp)\rangle + \sum_n \int_{\text{BZ}} d\mathbf{k}_\perp r_n(\mathbf{k}_\perp) |L_{n-}(\mathbf{k}_\perp)\rangle = \sum_n \int_{\text{BZ}} d\mathbf{k}_\perp t_n(\mathbf{k}_\perp) |R_{n+}(\mathbf{k}_\perp)\rangle, \quad (3.22)$$

with $r_n(\mathbf{k}_\perp)$ and $t_n(\mathbf{k}_\perp)$ being the reflection and transmission coefficients. $i_n(\mathbf{k}_\perp)$ describes the modal decomposition of the impinging field. The rigorous solutions for $r_n(\mathbf{k}_\perp)$ and $t_n(\mathbf{k}_\perp)$ can be derived by projecting Eqn. (3.22) once on $\langle R_{k-}^\dagger |$ and once on $\langle L_{k+}^\dagger |$ and by

exploiting the orthogonality relations according to Eqs. (3.14)-(3.21). In matrix notation this results in

$$\mathbf{r}(\mathbf{k}_\perp) = -\hat{a}^{-1}\hat{c} \mathbf{i}(\mathbf{k}_\perp), \quad (3.23)$$

$$\mathbf{t}(\mathbf{k}_\perp) = \hat{d}^{-1}\hat{f} \mathbf{i}(\mathbf{k}_\perp), \quad (3.24)$$

where the matrix elements are determined by

$$a_{kn} = \{R_{k-}(-\mathbf{k}_\perp)|L_{n-}(\mathbf{k}_\perp)\}, \quad (3.25)$$

$$c_{kn} = \{R_{k-}(-\mathbf{k}_\perp)|L_{n+}(\mathbf{k}_\perp)\}, \quad (3.26)$$

$$d_{kn} = \{L_{k+}(-\mathbf{k}_\perp)|R_{n+}(\mathbf{k}_\perp)\}, \quad (3.27)$$

$$f_{kn} = \{L_{k+}(-\mathbf{k}_\perp)|L_{n+}(\mathbf{k}_\perp)\} = L_k^+(\mathbf{k}_\perp)\delta_{kn}. \quad (3.28)$$

Remarkably, the reflection and transmission coefficients for the particular lateral Bloch vector component \mathbf{k}_\perp are exclusively determined by the incident field components i_n which possess the same lateral Bloch vector component. At first, this result reflects the mutual orthogonality relations fulfilled by the Bloch modes of both media according to Eqs. (3.18)-(3.21) and, secondly, it is a manifestation of the boundary conditions which enforce the continuity of the lateral Bloch vector component in the considered configuration. Henceforth, knowing the Bloch modes of both media \mathcal{L} and \mathcal{R} one can construct the matrices \hat{a} , \hat{c} , \hat{d} and \hat{f} according to Eqs. (3.25)-(3.28) and apply them to rigorously solve for the reflection and transmission coefficients of all Bloch modes excited at the interface. For the sake of completeness, the elements of the coefficient vector \mathbf{i} are calculated by projecting any incident field distribution, say $|I\rangle$, onto the modes $|L_{n+}^\dagger\rangle$. Using Eqn. (3.13) yields $i_n(\mathbf{k}_\perp) = \langle L_{n+}^\dagger(-\mathbf{k}_\perp)|I\rangle/L_n^+(\mathbf{k}_\perp)$.

3.2.2 Fundamental mode approximation

The following considerations are restricted to the important case that only the *fundamental mode*[‡] $|L_{0+}\rangle$ is impinging on the interface, i.e. $i_0(\mathbf{k}_\perp) = 1, i_{n \geq 1}(\mathbf{k}_\perp) = 0$. For scenarios where the eigenmodes of media \mathcal{L} and \mathcal{R} largely match each other, the matrices \hat{a} , \hat{c} , \hat{d} are expected to become sparse. Hence, approximate solutions can be found by contracting the description to small sub-matrices which only take into account a small number of entries around the fundamental mode. Doing that, the size of the sub-matrices dictates the accuracy of the

[‡]The fundamental mode is characterized by the lowest imaginary part of the propagation constant k_z . Thus, it prevails against all other Bloch modes in terms of attenuation during bulk propagation. For a detailed discussion see also Sec. 3.3.

approximation[§]. This procedure is quite similar to the usage of impedance matrices when dealing with dielectric systems [97]. However, applying the crudest approximation, that is to take into account only the first element of all matrices defined by Eqs. (3.25)-(3.27), one obtains

$$r_0(\mathbf{k}_\perp) = -\frac{\langle R_{0-}(-\mathbf{k}_\perp)|L_{0+}(\mathbf{k}_\perp)\rangle}{\langle R_{0-}(-\mathbf{k}_\perp)|L_{0-}(\mathbf{k}_\perp)\rangle}, \quad (3.29)$$

$$t_0(\mathbf{k}_\perp) = \frac{\langle L_{0+}(-\mathbf{k}_\perp)|L_{0+}(\mathbf{k}_\perp)\rangle}{\langle L_{0+}(-\mathbf{k}_\perp)|R_{0+}(\mathbf{k}_\perp)\rangle} \quad (3.30)$$

for the reflection and transmission coefficients into the fundamental modes. As part of this assumption, the resulting reflection and transmission coefficients $r_{n \geq 1}$ and $t_{n \geq 1}$ into all higher modes are zero. If this approximation is justified, the situation resembles that of an interface between two genuine homogeneous media where the scattering properties are exclusively determined by the two fundamental eigenmodes. Hence, in what follows this approximation is called the *fundamental mode approximation*.

3.3 Beam propagation in metamaterials

In this section the focus will be on the properties and characteristics of light beams which propagate in bulk MMs over macroscopic distances. The description will turn out to be in full analogy to the description of diffraction of beams in homogeneous media. In that case, any electromagnetic field distribution can be expanded into plane waves and the entire problem of light propagation is then based on the propagation of a bunch of these eigenmodes [105]. Henceforth, it is assumed that any electromagnetic field distribution $|F\rangle(x, y)$ within a MM is known in a plane $z = 0$. In general, the expansion into Bloch modes at $z = 0$ is governed by Eqn. (3.12). For the sake of simplicity, the discussion will be limited to beams which are confined only in one lateral dimension, say x , such that the beam is exclusively composed of Bloch modes of type $|B_p(\alpha_0, \beta_0 = 0)\rangle$. Assuming that there are no sources located within the volume $z > 0$, the field propagating into the positive half-space will be given by

$$|F\rangle(x, y, z) = \sum_p \int_{-K_x/2}^{+K_x/2} d\alpha_0 A_{p+}(\alpha_0) |B_{p+}(\alpha_0)\rangle(x, y, z). \quad (3.31)$$

[§]Assuming \hat{a} , \hat{c} , \hat{d} and \hat{f} to be matrices of size $S \times S$ with a typical value of S in the order of $\mathcal{O}(10^3)$ for three-dimensional bulk structures. Then, the outlined approximation means, to truncate all matrices to a smaller size $\tilde{S} \ll S$ [in the order $\mathcal{O}(10^1) \dots \mathcal{O}(10^2)$]. The new quantities are defined according to, e.g., $\hat{a} \rightarrow (a_{kn})$ with $k, n = 1, \dots, \tilde{S}$. The crudest approximation is to truncate all matrices to a size of 1×1 , i.e. scalars, such that only the first entry of all matrices, e.g. a_{11} , is taken into account.

The Bloch spectrum $A_{p+}(\alpha_0)$ can be determined by applying Eqn. (3.13) to $|F\rangle(x, y)$ at $z = 0$.

In the following it turns out to be more convenient to split off the exponential component from the Bloch mode such that

$$|B_{p+}(\alpha_0)\rangle(x, y, z) \rightarrow |B_{p+}(\alpha_0)\rangle(x, y, z) \exp[i(\alpha_0 x + k_{p+,z} z)].$$

Consequently, the ket-vector $|B_{p+}(\alpha_0)\rangle(x, y, z)$ will only contain the actual Bloch mode's lattice periodic contributions in the remaining section. However, Eqn. (3.31) contains a continuous as well as a discrete superposition of modes and the question arises if this most general description is really required. Having in mind light propagation over sufficiently large distances, it is clear that only the Bloch mode with the lowest attenuation is transmitted. For that purpose, it is henceforth assumed that the set of Bloch modes $|B_{p+}(\alpha_0)\rangle$ is arranged according to the magnitude of the imaginary part of their propagation constants, i.e. $\Im[k_{0+,z}(\alpha_0)] < \Im[k_{1+,z}(\alpha_0)] < \Im[k_{2+,z}(\alpha_0)] < \dots$, where the arrangement is individually applied for every angular component. Then, the smallest mode index p_{\min} is selected which fulfills $|A_{p+}(\alpha_0)| > 0$ and all higher terms $p > p_{\min}$ of the sum appearing in Eqn. (3.31) are neglected[¶]. Consequently, this equation simplifies to

$$|F\rangle(x, y, z) = \int_{-K_x/2}^{+K_x/2} d\alpha_0 A(\alpha_0) |B(\alpha_0)\rangle(x, y, z) \exp[i\alpha_0 x] \exp[ik_z(\alpha_0) z] \quad (3.32)$$

with the mode index p_{\min} being omitted in the following. Henceforth, $|B(\alpha_0)\rangle$ denotes the so-called *fundamental mode* and $A(\alpha_0)$ is the respective angular distribution.

The paraxial limit. The expression defined by Eqn. (3.32) is rather involved since the considered Bloch modes (ket-vectors) explicitly depend on the spatial coordinates. Due to the fact that beams are usually extended over multiple unit cells in the lateral direction, the expansion function $A(\alpha_0)$ is assumed to be limited to the BZ. Furthermore, $A(\alpha_0)$ is assumed to be centered around a central lateral Bloch vector component $(\tilde{\alpha}_0, 0)$. Hence, a Taylor expansion of the propagation constant $k_z(\alpha_0)$ can be performed which leads to

$$k_z \approx \xi_0 + \xi_1(\alpha_0 - \tilde{\alpha}_0) + \frac{\xi_2}{2}(\alpha_0 - \tilde{\alpha}_0)^2 \quad (3.33)$$

[¶]The outlined choice of p_{\min} takes into account additional selection rules for all Bloch modes, e.g. their symmetry. $|A_{p+}(\alpha_0)| = 0$ means that the associated mode is not excited.

where the expansion coefficients are defined according to

$$\xi_0 = \xi'_0 + i\xi''_0 = k_z(\tilde{\alpha}_0) \quad (3.34)$$

$$\xi_1 = \xi'_1 + i\xi''_1 = \left. \frac{\partial k_z}{\partial \alpha_0} \right|_{\tilde{\alpha}_0} \quad (3.35)$$

$$\xi_2 = \xi'_2 + i\xi''_2 = \left. \frac{\partial^2 k_z}{\partial \alpha_0^2} \right|_{\tilde{\alpha}_0} \quad (3.36)$$

Now, Eqs. (3.33)-(3.36) are inserted into Eqn. (3.32) and the resulting expression is only evaluated at discrete points $x = u\Lambda_x$, $y = v\Lambda_y$ and $z = w\Lambda_z$ with u , v and w being integers. Due to the fact that $A(\alpha_0)$ is non-zero only in the BZ, one can extend the integration limits to infinity and the resulting integral will transform into a Fourier integral which gives

$$\begin{aligned} |F\rangle(u\Lambda_x, w\Lambda_z) &= \int_{-\infty}^{+\infty} d\alpha_0 A(\alpha_0) |B(\alpha_0)\rangle(x=0, y=0, z=0) \\ &\times \exp[ik_z(\alpha_0)z] \exp[i\alpha_0 u\Lambda_x] \end{aligned} \quad (3.37)$$

since $|B(\alpha_0)\rangle$ does not depend on $(x = u\Lambda_x, y = v\Lambda_y, z = w\Lambda_z)$ explicitly. Transforming this expression into the spatial domain, light propagation is formally described by a partial differential equation, i.e.

$$\left[i\frac{\partial}{\partial w} + \xi_0 - i\xi_1 \frac{\partial}{\partial u} - \frac{\xi_2}{2} \frac{\partial^2}{\partial u^2} \right] |V\rangle(u, w) = 0, \quad (3.38)$$

with $|V\rangle(u, w) = |F\rangle(u\Lambda_x, w\Lambda_z) \exp(-i\tilde{\alpha}_0 \Lambda_x u)$ being the electromagnetic field distribution in the quasi-continuous limit. Now, u and w are continuous variables and, henceforth, Eqn. (3.38) will describe light propagation effects on length scales which typically extend over multiple unit cells [111, 112]. The rather subtle field distributions appearing within a single unit cell (or around a meta-atom) can not be predicted by that. Let us have a look at a short example to get a better feeling for this description. For that purpose the evolution of a super-Gaussian beam profile within a 2D photonic crystal is presented in Fig. 3.2. As it is expected, the quasi-continuous model well reproduces the *ordinary* diffraction effects, like beam spreading, whose typical length scale extends over several wavelengths. On the contrary, the rather sharp field gradients occurring within the unit cell of the considered structure are completely annihilated as compared to the rigorous field propagation model according to Eqn. (3.32). However, if one is only interested in the *large-scale* features occurring during the evolution of the beam and not in the *near-field* features which dominate on length scales smaller than one unit cell, then the usage of Eqn. (3.38)

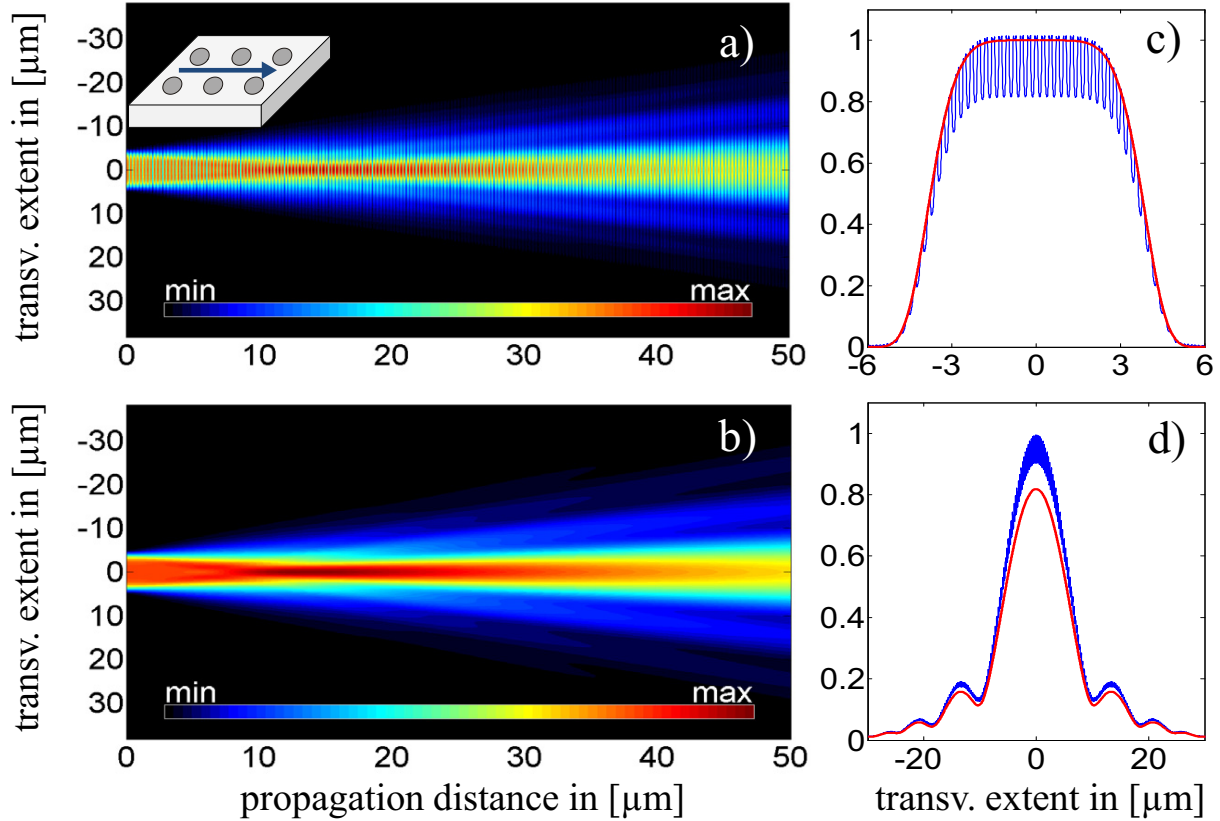


Figure 3.2: Amplitude evolution of a super-Gaussian beam $[\exp\{(x/4\mu\text{m})^6\}]$ at $z = 0$ inside a 2D photonic crystal at wavelength $\lambda = 1500$ nm. The photonic crystal (see inset) consists of air holes (diameter: 200 nm) in a silicon matrix ($n = 3.5$). The period is 255 nm and the polarization is TM (\mathbf{H} in out-of-plane direction). The arrow indicates the direction of propagation. The figures on the left display the modulus of the magnetic field $|\mathbf{H}|$ as calculated by the rigorous propagation model (a) according to Eqn. (3.32) and the quasi-continuous propagation model (b) according to Eqn. (3.38). For a better visibility, the magnetic field distribution is plotted over the lateral coordinate at propagation distances $z = 0$ (c) and $z = 50 \mu\text{m}$ (d). The blue (red) lines correspond to the rigorous (quasi-continuous) propagation model.

greatly simplifies the entire description.

3.3.1 Inclination and diffraction coefficients

Equation (3.38) is very similar to the well-known paraxial wave equation which governs the evolution of light in a homogeneous medium [112, 113]. For the sake of simplicity, it is convenient to assume for a moment that $\xi_1'' \ll \xi_1'$. Then, inspecting Eqn. (3.38), the first derivative will mainly cause the beam to continuously shift in lateral direction. More precisely, its center of gravity will move on a straight line determined by $u = \xi_1' w$. Thus, ξ_1' is called the *inclination coefficient* since it defines the beam's main angle of propagation

relative to the z -axis, i.e. $\tan(\theta) = \xi'_1$. Moreover, when thinking about refraction of light at the single interface between two MMs, then the sign of the product $R = \xi'_{1,\text{MM1}}(\tilde{\alpha}_0) \cdot \xi'_{1,\text{MM2}}(\tilde{\alpha}_0)$ between the inclination coefficients of the two MMs decides whether positive ($R > 0$) or negative ($R < 0$) refraction appears. Now, concentrating on the imaginary part ξ''_1 , it can be concluded that it causes an asymmetric damping of the beam. It will lead to beam distortions during propagation, but more importantly, it can bend the beam's major propagation direction since the angular center of gravity can be modified.

Now, the focus is shifted to the second derivative appearing in Eqn. (3.38). Its real part ξ'_2 is responsible for diffraction, and its imaginary part ξ''_2 results in angular filtering of the beam. Once again, it is more convenient to discuss propagation effects attributed to ξ'_2 and ξ''_2 independently from each other. Starting with the imaginary part, it is more convenient to discuss its influence in Fourier domain using Eqn. (3.37). Clearly, the existence of a term $\propto \exp(-\xi''_2(\alpha_0 - \tilde{\alpha}_0)^2 z)$ will modify the modulus of the angular spectrum $A(\alpha_0)$ in a non-trivial fashion. However, it can be concluded that the sign of ξ''_2 determines whether the initial distribution $A(\alpha_0)$ is affected by a low pass ($\xi''_2 > 0$) or a high pass Fourier filter ($\xi''_2 < 0$). Accordingly, one will observe a spreading or a contraction of the beam in spatial domain. This must look very similar to ordinary diffraction. Now, concentrating on the real part of ξ'_2 , and assuming that $\xi''_2 \ll \xi'_2$ for convenience, we end up with the typical discussion that is routinely facilitated for dielectric structures, e.g. photonic crystals. There, effects caused by ordinary diffraction are usually discussed along the beam's main direction of propagation which is determined by ξ'_1 as discussed above. Then, the second derivative which defines ξ'_2 will turn into the local curvature of the dispersion relation's real part $\Re(k_z)$ evaluated at $\tilde{\alpha}_0$. Thus, ξ'_2 will transform into the following expression

$$\xi'_2(\mathbf{k}^{(0)}) = \left. \frac{d^2 \Re(\mathbf{k})}{ds^2} \right|_{\mathbf{k}^{(0)}}, \quad (3.39)$$

with $ds = |d\mathbf{k}|$, $\mathbf{k} = [\alpha_0, \Re(k_z(\alpha_0))]^T$ and $\mathbf{k}^{(0)} = [\tilde{\alpha}_0, \Re(k_z(\tilde{\alpha}_0))]^T$. This rather general definition translates into the more convenient form

$$\xi'_2(\tilde{\alpha}_0) = \frac{\frac{\partial^2 \Re(k_z)}{\partial \tilde{\alpha}_0^2}}{\left[1 + \left(\frac{\partial \Re(k_z)}{\partial \tilde{\alpha}_0} \right)^2 \right]^{\frac{3}{2}}}. \quad (3.40)$$

for an iso-frequency contour of the functional type $k_z(\alpha_0)$. For propagation along the z -direction, i.e. $\xi'_1(\tilde{\alpha}_0) = \partial \Re(k_z) / \partial \tilde{\alpha}_0 = 0$, Eqn. (3.40) coincides with the former definition according to Eqn. (3.36).

In contrast to ordinary, dielectric homogeneous media where the *diffraction coefficient* ξ'_2

is constant (it is $-1/k$), here it is determined by the particular dispersion relation of the underlying MM. For that reason, the diffraction coefficient may take arbitrary values such that it can be negative, positive or it even may become zero. Then, one typically speaks about *normal diffraction* ($\xi'_2 < 0$), *anomalous diffraction* ($\xi'_2 > 0$) and *diffractionless propagation* ($\xi'_2 = 0$). The description of light propagation in terms of its diffraction coefficient is rather established for photonic crystals and photonic lattices [21, 112] and not for MMs. One reason is certainly the difficulty to observe light propagation over several unit cells in highly absorbing metallic nano-structures. However, the assumption to have bulk MMs at hand is not necessary and already thin MM slabs are conveniently described with the parameters presented above, since they do not rely on any effective medium assumptions. Instead, light propagation is exclusively described by relying on the true eigenmodes of the underlying structure. Just to give one example, the authors of Ref. [114] report about rigorous numerical simulations of a fishnet MM where positive refraction was obtained from a negative-index MM and vice versa. These findings cannot be explained on grounds of effective media theories, but they are easy to explain with the model presented above. In that sense, the next chapter will present a thorough analysis of a fishnet MM where, amongst others, these effects are studied and consequences are drawn.

3.4 Chapter summary and concluding remarks

This chapter has started with the introduction of Bloch modes in absorbing, periodic nano-structures, i.e. MMs. The defined Bloch modes $|B_p(\mathbf{k}_\perp, \omega)\rangle$ parametrically depend on the lateral Bloch vector component $\mathbf{k}_\perp \in \text{BZ}$ and the frequency $\omega \in [0, \infty)$. The last Bloch vector component $k_z = k_{p,z}(\mathbf{k}_\perp, \omega)$ is determined by the multi-branch dispersion relation and it has an infinite but countable number of solutions. Important to note, this representation must not be confused with the one that is commonly used for photonic crystals made from non-absorbing materials [101]. For photonic crystals the modes $|M_n(\mathbf{k}_\perp, k_z)\rangle$ depend on all three Bloch vector components in a parametric manner, and the frequency is determined by the dispersion relation $\omega = \omega_n(\mathbf{k}_\perp, k_z)$. Then, modes are non-orthogonal to each other whenever they have the same Bloch vector and frequency (mode index n). However, orthogonality relations between Bloch modes were shown in this work to exist also in the absorbing case, namely for MMs. They were derived in the first part of this chapter and they represent fundamental and self-contained results. The second part of this chapter was on the correct treatment of reflection and transmission of light at the boundary between two dissimilar MM half-spaces. Here, the orthogonality relations were successfully applied to derive closed-form expressions for the reflection and transmission coefficients in terms of the

Bloch modes of both media. In general, a mutual cross coupling between all Bloch modes appears. Only in case that the eigenmodes of both MMs largely match each other, this cross-coupling can be neglected. This allows to find simplified expressions for the reflection and transmission coefficients that are solely based on the fundamental modes of both media. This is what is henceforth called the fundamental mode approximation. It has to be stressed that this approximation is not just a technical detail but essential to discuss the physics of MMs. Such detailed discussion will be provided in the next chapter. In this context it will be shown that the validity of the fundamental mode approximation is intimately connected with the homogeneity of MMs. Last but not least, the current chapter has closed with a discussion about the propagation of beams in bulk MMs. Concepts already known from photonic crystals and photonic lattices were modified and adapted to the inevitable situation that attenuation (damping) has to be taken into account. Thus, parameters such as the diffraction and inclination coefficients were introduced. They are solely derived from the Bloch mode's dispersion relation with the aim to describe refraction and diffraction in MMs without relying on any assumption or effective medium model for the underlying nano-structure.

4 Investigation of bulky fishnet-like metamaterials

In view of macroscopic optical devices which may comprise MMs or MM components, there is a strong need for three-dimensional bulk MMs. For that purpose, unit cells of various shape were suggested to be arranged in a deterministic three-dimensional manner. Several promising examples were published that report on the fabrication of bulky samples using either direct laser writing or electron beam lithography to built up multi-layer fishnet or split-ring structures [28, 115–118].

To understand this urgent need, one has to look back at the beginnings of MM's research which started with Pendry's work about the perfect lens [3] – a simple slab of a homogeneous material having a permittivity and permeability of -1 . Unfortunately, there is no natural material available in the optical domain which offers a serious magnetic polarizability [119] and, henceforth, a large campaign started to find and build man-made structures mimicking magnetically and electrically polarizable entities. Finally, the development of transformation optics with its proposals for novel and incredible devices [5, 8] additionally provoked the need for homogeneous bulk media with engineered electric and magnetic properties.

Most suggestions for contemporary MM structures exploit the excitation of localized plasmon polariton resonances as provided by metallic nano-structures. These structures promise a large interaction between light and matter while simultaneously exhibiting small feature sizes. Though, the creation of homogeneous MMs, especially working in the optical domain, has turned out to be a delicate issue [TP04, 120, 121]. The assignment of local, effective material parameters follows the paradigm that light only weakly resolves the spatial details of the unit cells which stays in full analogy to the classical transition from microscopic to macroscopic electrodynamics*. In consequence, the actually structured material is conceptually substituted by an effective continuous distribution (with its eigenmodes being plane waves)

*The term *weakly* refers to so-called *weak spatial dispersion*. In classical electrodynamics the material response is solely attributed to the effect of the electrical field on the current density, i.e. $\mathbf{j}(\omega, \mathbf{k}) = \hat{R}(\omega, \mathbf{k})\mathbf{E}(\omega, \mathbf{k})$. Expanding the response tensor \hat{R} into a power series with respect to the wavevector \mathbf{k} , then one speaks about *weak spatial dispersion* if this expansion is limited by the second order term. Only in that case local material parameters, namely $\epsilon(\omega, \mathbf{k})$ and $\mu(\omega, \mathbf{k})$ can be assigned.

that must provide identical optical properties. A wide variety of publications is dedicated to this intent and one can refer to three major strategies to assign effective parameters – the parameter retrieval techniques [TP05,122–124], the wave propagation retrieval [125] and methods based on field averaging [126–128]. However, clear indications that the retrieved quantities cannot be considered as local, effective material parameters are their thickness and angular dependence [TP04,TP06,129,130]. In fact, investigating the angular dispersion characteristics $\mathbf{k}_B(\omega = \text{const.})$, i.e. the iso-frequency surfaces, of most MMs it is obvious that they cannot simply be mapped to any known behavior of local homogeneous materials as there are, e.g., isotropic or anisotropic ones [TP04,120,131–133]. Consequentially, there is a strong need for a more fundamental description.

In what follows the focus will be on the description of periodically arranged, stacked MMs with lateral periods that are only slightly smaller than the wavelength. This situation is typical for MMs operated in the optical domain. It is the declared aim of this chapter to explain the characteristics of light propagation through bulk MMs only by the Bloch modes as introduced in Chap. 3. However, this description does not prevent the introduction of effective parameters which help to simplify the description of light propagation in MMs. In fact, the inclination and diffraction coefficients as introduced in the previous chapter may be regarded as effective parameters which help to describe refraction as well as diffraction of beams in periodic media in a very compact way. However, to bridge the gap between the Bloch modal description and various homogenization efforts it appears best to start with a clear specification of the term *homogeneous* as we want to understand in the following. In due consideration of different concepts discussed in the scientific literature, it might be best understood and described in terms of a hierarchical scheme, where subsequent statements require the previous to be fulfilled.

- ▶ The entities of a medium have to be sub-wavelength. Then, by illuminating a slab sample with a plane wave the transmitted as well as the reflected far field is still a plane wave, i.e. higher diffraction orders are evanescent.
- ▶ Light propagation inside the medium is determined by a single Bloch mode – the so-called fundamental mode (FM).
- ▶ Additionally, also the coupling of light (reflection/transmission) from or to an external medium is determined by the same fundamental Bloch mode. When these conditions are fulfilled, we say that the *fundamental mode approximation* (FMA) is valid. The medium might then be characterized by the propagation constant of the FM and its impedance. These two parameters, describing the properties of the FM, are called *effective wave parameters*.

- If the dispersion relation of the FM can be mapped onto that of a true homogeneous medium obeying a certain constitutive relation, the effective *wave parameters* might be reduced to local, effective *material parameters*. These are necessarily independent of the shape and the illumination scheme of a specimen and are solely related to the material itself.

Since most interesting dispersive features of MMs (especially the magnetic ones) fade away the smaller the unit cells are [TP04, 134–136], one has to get used to the idea that the mesoscopic size domain is rather essential rendering the assignment of local, effective material parameters as unfeasible. Thus, the ultimate (fourth) criterium of the aforementioned hierarchy can be hardly met and one has to return to the third and second item. Therefore, in the following considerations, the term *homogeneous medium* is used in its more general form, i.e. considering the properties of the FM or, equivalently, its effective parameters.

Despite the variety of available MM structures, the following considerations will focus on bulky fishnet MMs which became famous due to their left-handed behavior[†] and simultaneously exhibiting comparatively low losses [137, 138]. Moreover, this class of MMs is widely investigated, both experimentally and theoretically, such that it represents a sound source for further investigations. However, it has to be mentioned that the concept of Bloch modes was already successfully applied to various MM structures and turned out to be in full consistency with rigorous results [TP00, TP07, TP08, 139, 140].

The current chapter is structured as follows. In Sec. 4.1 the fishnet MM structure will be briefly reviewed and its fundamental mechanism of operation as a left-handed material is explained. In Secs. 4.2 and 4.3.1 the Bloch modes of a bulky fishnet MM are determined and their dispersion relation is presented. In this context it will be shown, that the potential left-handed behavior of the fishnet structure is linked to a fundamental Bloch mode which exhibits a Bloch vector which points against the direction of propagation, i.e. the Poynting vector. Then, the dispersive characteristics of the fundamental Bloch mode are extensively used to analyze diffraction within a bulky fishnet MM and also refraction into the same one. It will be demonstrated that the operation in the left-handed regime is not sufficient nor necessary to observe effects like negative refraction or anomalous diffraction. As an example, the thorough analysis of a fishnet structure reveals that it even supports ordinary, positive refraction in the left-handed domain. Based on these results and findings, a super-cell MM approach is then outlined in Sec. 4.4 which allows to mould the angular dispersion relation of the fundamental Bloch mode by desire. By that, a super-cell fishnet

[†]Sometimes this is also referred to a *negative phase velocity* or even a *negative effective refractive index*.

structure is presented which shows either a nearly circular angular dispersion relation (as isotropic materials would do) or even a very flat one which gives rise to the observation of diffractionless propagation. Finally, the chapter will close with Sec. 4.5 where the attention is drawn to the scattering of light at the interface of a MM. In particular, the focus will be on the reflection and transmission of plane waves at the interface between air and a MM and the coupling properties are then exploited as a measure to evaluate the homogeneity of MMs in general. Some of the results that will be presented in the following were published in several regular articles [TP09, TP10, TP03].

Eventually, there is a final note to draw in advance with respect to the applicability of the parameter retrieval procedure. When it is applied to a finite MM slab it will provide an effective propagation constant $k_{z,\text{eff}}$ and an effective impedance Z_{eff} as the fundamental output. Assuming that the FMA is fulfilled, they constitute the effective wave parameters of the fundamental Bloch mode (for a detailed discussion see Sec. 4.5.1). In the opposite case, i.e. the FMA is not justified, then $k_{z,\text{eff}}$ and Z_{eff} will lose their physical meaning in general and they cannot be linked to a modal property anymore. However, when the parameter retrieval is applied to periodic but absorbing MMs it turns out that at least $k_{z,\text{eff}}$ will still converge against k_z of the fundamental Bloch mode of the considered medium as long as the thickness of the MM layer is chosen to be large enough [TP06, TP07, 141]. Keeping this in mind will facilitate the considerations of the following sections.

4.1 The fishnet structure

The fishnet structure was first introduced by Zhang *et al.* in 2006 [142, 143]. According to Ref. [142], the structure's properties were characterized by calculations of a single fishnet slab which showed a negative phase evolution in transmission. Using an S-parameter retrieval method [124] the authors had concluded that the fishnet exhibits a negative effective permittivity and permeability. Within the framework of isotropic, homogeneous materials the negativity of both parameters is a prerequisite to obtain a negative refractive index expressing the left-handedness of the underlying material [3].

A layout of the fishnet structure is depicted in Fig. 4.1a. The fishnet, as it was originally introduced, is composed of two nano-structured metallic films (yellow layers) which are separated by a thin dielectric layer (gray layers). Furthermore, the perforated metallic film combines a thick metallic double wire structure (in y -direction) crossed by comparatively thin wires under an angle of 90° . The fundamental mechanism of operation of the fishnet structure is as follows. The thin wires effectively work as a diluted electron gas and they only

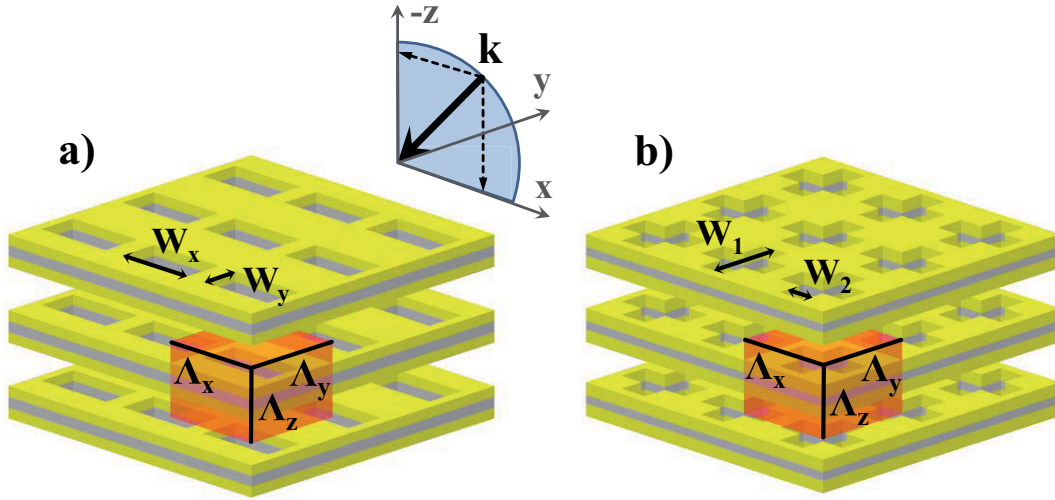


Figure 4.1: Schematic of a multi-layer fishnet (a) and Swiss cross MM (b). The structure is assumed to be infinitely extended in all spatial dimensions and the red box indicates the respective unit cells.

influence the electric field. On the other hand, the thick double-wire structure will affect the electric as well as the magnetic field. This fact is reflected, e.g., in an electric quadrupolar and magnetic dipolar character of the near field at a single double-wire or even only a single double cut-wire structure [144–147]. Within the framework of an effective medium theory the influence on the magnetic field is rather essential since it allows to modify the dispersion of the effective permeability which eventually may lead to a left-handed behavior of the composite structure. However, to avoid any difficulties which may arise from the description of MMs, and in particular fishnet MMs, by effective parameters we will instead rely on the dispersion relation of Bloch modes as already stated above. Consequently, we will consider the fishnet to be a periodic structure in all three spatial dimensions. The final layout is already displayed in Fig. 4.1a with a single unit cell indicated by the red box.

Finally and for the sake of completeness, it has to be mentioned that the original fishnet structure as introduced by Zhang *et al.* can be further optimized to exhibit a response which is independent from the polarization for propagation purely along the z -direction [148, 149]. In that sense, Fig. 4.1b shows one successor of the original fishnet structure, namely a Swiss cross MM [149]. It will be subject to research in Sec. 4.5. Despite the rearrangement of the unit cell's shape, the fundamental mechanism of operation still follows the principles as explained above and, consequently, it may be considered as a fishnet-like MM.

4.2 Frequency dispersion of a fishnet

Bloch modes and their polarization. The geometrical parameters of the fishnet MM to be investigated in the following are motivated by a fabricated (single layer) sample as reported in Ref. [150]. The sample consists of a pair of 45 nm silver layers [M.1] (see chapter *Material parameters* in the appendix for detailed information) separated by a thin dielectric MgF₂ layer ($\epsilon = 1.90$) of 30 nm thickness. The hole sizes are $W_x = 500$ nm and $W_y = 284$ nm. Without loss of generality, it is assumed that adjacent functional fishnet layers are embedded in air ($\Lambda_z = 200$ nm) to end up with a bulk MM. From a technical point of view this choice seems to be rather puzzling, but it helps to keep the achieved resonance position in the vicinity of that reported in Ref. [150]. Choosing any other dielectric to be the host material will mainly shift the resonance position but it does not alter the physical conclusions.

Numerically calculating the dispersion relation $k_{p,z}(k_x = k_y = 0, \omega)$ of the considered structure, the result is a finite and discrete spectrum of modes with mode index p . However, displaying the dispersion relation of all calculated modes is quite confusing. Therefore, it is sufficient to provide here a small selection of modes and to describe their basic properties that are representative for the complete modal spectrum. Doing that, it can be first recognized that the entire dispersion relation $k_{p,z}(k_x = 0, k_y = 0, \omega)$ can be divided into two subsets of modes, i.e. Σ^+ (forward propagating) and Σ^- (backward propagating). Assuming all constituent materials to be reciprocal, these two subsets are simply related by $\Sigma^+ = -\Sigma^-$, meaning that the achieved solution will always be composed of pairs of modes which have a propagation constant which is opposite in sign as it was already explained in Sec. 3.1. The following discussion will be, without loss of generality, restricted to modes propagating in positive z -direction. Figure 4.2 shows the relevant data for the real and imaginary part of the propagation constant $k_{p,z}$. There are four modes displayed in Figs. 4.2a and 4.2b which can be divided into three different classes of polarization states as indicated by the choice of colors. The net polarization is determined by averaging the electrical field distribution over the x - y -cross section of a unit cell. As it is indicated by Figs. 4.2c - 4.2f, the red solid and dashed modes show a net polarization in y -direction, the blue mode exhibits a net polarization in x -direction, and the green mode has a zero net polarization meaning that the cross section average of the complete electrical field distribution vanishes. This categorization is quite helpful when considering a finitely extended MM to which light couples from the outside at a planar interface. Then, it helps to decide which class of modes is capable to couple to an impinging plane wave of a certain polarization. By that it becomes immediately clear, that Bloch modes with a zero net polarization (the green one) cannot be excited by a plane wave under normal incidence and, consequently, their properties are practically not

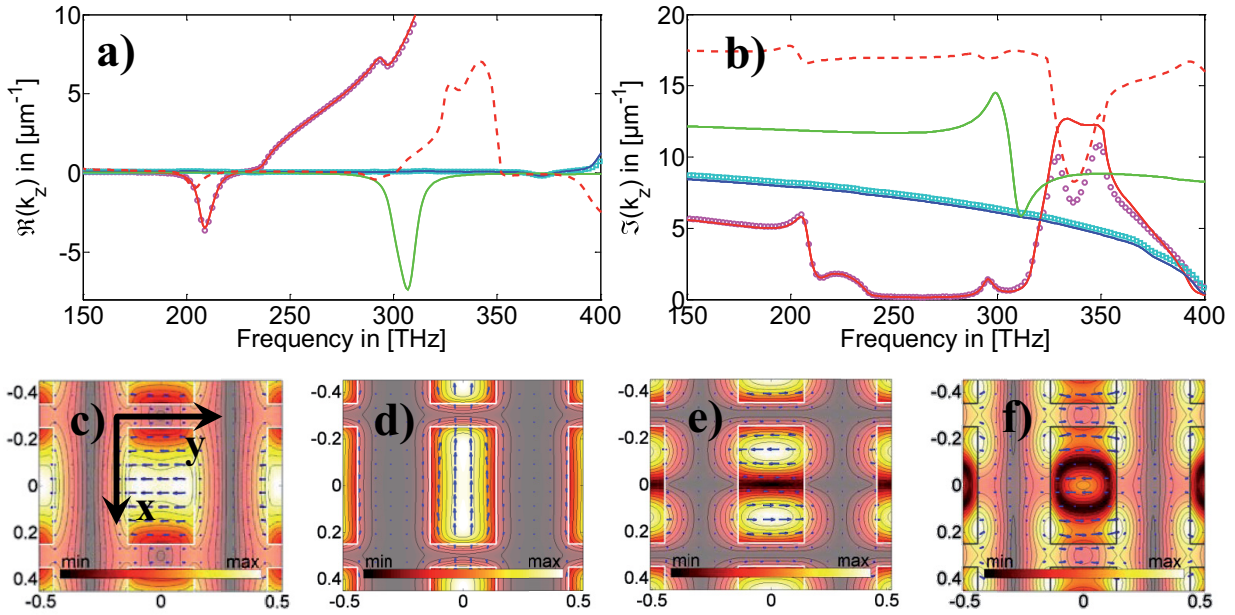


Figure 4.2: Real (a) and imaginary part (b) of the dispersion relation $k_z(\omega)$ of the bulk fishnet MM under consideration for the lowest-order Bloch modes. Propagation is assumed to be along the z -direction, i.e. $(k_x, k_y) = (0, 0)$. The solid curves represent the Bloch modes with the lowest imaginary parts of k_z at 150 THz, that is the lowest frequency of the calculated spectrum. The green (red, blue) curves correspond to modes with zero (y -, x -) net polarization determined by averaging the electrical field distribution across the lateral directions, i.e. x and y . The red dashed line is the second-order Bloch mode possessing a net polarization in y -direction. The magenta (blue) symbols display the effective propagation constant k_{eff} as determined by a parameter retrieval procedure for plane wave illumination polarized in y - (x -) direction. In that case, a finite fishnet structure was assumed extending over 10 functional layers in propagation direction. The remaining figures show the corresponding electrical field distribution ($|\mathbf{E}|$) of all four modes shown above [red solid (c), blue solid (d), green solid (e), red dashed (f)] at 208.8 THz in a plane centered between two adjacent functional fishnet layers. i.e. $z = 0$ (as introduced in Fig. 4.1). The shaded area indicates the location of the actual fishnet layers and the arrows represent the magnitude and direction of the lateral electrical field components $(E_x \mathbf{e}_x + E_y \mathbf{e}_y)$.

accessible.

A fundamental mode with negative phase velocity. Concentrating on the particular results displayed in Figs. 4.2a and 4.2b, it can be seen that the red solid mode exhibits a frequency region from 195 THz to 222 THz in which the real part $\Re(k_z)$, which is a measure for the phase velocity, becomes reasonably negative while the energy flow concurrently maintains its direction along $+z$. This is exactly the realm where this specific mode shows a left-handed behavior. Remembering its polarization state, it becomes obvious that this mode can only be excited by a y -polarized plane wave impinging on a finite fishnet structure. At the same time, this mode represents the FM (as introduced in Sec. 3.3) in y -polarization

because it clearly shows the lowest imaginary part of the propagation constant as compared to the next higher-order mode (red dashed line). Thus, it will dominate the light propagation over sufficiently large distances because finally its attenuation prevails against all other modes. However, in the higher frequency region right above 320 THz, there is a crossing of the red modes observable. Consequentially, also the identity of the FM will migrate. This peculiarity can also be observed when a parameter retrieval procedure is applied to an appropriate finite fishnet slab structure. In the considered case, the parameter retrieval method is applied to the reflection and transmission spectra of a slab that consists of 10 fishnet layers in height and that is illuminated by a y -polarized plane wave. The associated results achieved for the effective propagation constant k_{eff} are shown in Figs. 4.2a and 4.2b by the magenta symbols. As expected, the imaginary part of k_{eff} clearly follows the values of that Bloch mode which exhibits the lowest imaginary part of $k_{p,z}$, i.e. the FM [TP06]. Hence, the migration of the FM's identity is clearly reflected by the presented data. However, the situation is more involved for the real part of the retrieved effective propagation constant. Although it is not shown explicitly in Fig. 4.2a, the retrieved values start to fail the Bloch modal data for frequencies larger than about 320 THz which corresponds to the aforementioned first crossing point of the two red Bloch modes (see Fig. 4.2b). Without going too much into the details of the parameter retrieval procedure, but the reason for this erroneous behavior lies in the fact, that the retrieved effective propagation constant k_{eff} is determined except for a factor of $2\pi m/L$, with L being the slab thickness and m being an integer number. As soon as the FM's identity migrates between two Bloch modes, then an unambiguous determination of the integer multiple m is no longer possible in general. Finally and to complete the story, the cyan symbols in Figs. 4.2a and 4.2b represent the retrieved effective propagation constant $k_{z,\text{eff}}$ when the incident polarization is switched to the x -direction. Then, the achieved results clearly coincide with the blue mode because it exhibits a compatible net polarization while simultaneously having the lowest attenuation.

4.3 Beam propagation in a fishnet

It was shown in the previous section, that the dispersion relation of the FM of a bulk MM may indeed be determined by a conventional parameter retrieval method. Despite the fact that it will not be shown explicitly here, this property also holds when the lateral Bloch vector components do not vanish, i.e. $k_x \neq 0$ and/or $k_y \neq 0$. One can take advantage of this fact by applying a parameter retrieval method for oblique incident waves [TP05, TP07]. However, this strategy shall not mislead from the fact that an assignment of local, effective material parameters (which are free of spatial dispersion) is still impossible since

the dispersion relation of the FM generally does not match that of a local homogeneous medium, e.g. isotropic or anisotropic ones. Consequentially, a given MM can only be conceptually replaced (in the sense of a black box) by an effective homogeneous medium in an exceptional case. This case is, of course, the determination of reflection and transmission coefficients of plane waves (for a fixed frequency and direction of propagation) scattered at a particular finite MM slab. However, this situation is of minor practical relevance, since this corresponds to the re-inversion of the parameter retrieval procedure itself. Especially, if one is interested in the propagation of beams which can be understood as a superposition of different plane waves (or better eigenmodes), the situation becomes more complex. Then, the properties of beams, i.e. refraction and diffraction, interacting with artificial bulk materials are better described in terms of the dispersion relation of their eigenmodes. This strategy is a standard technique, e.g., for photonic crystals and waveguide arrays and interesting effects such as zero and anomalous diffraction [151–153] as well as negative refraction [154, 155] can be clearly identified. Here we aim at proceeding along this path by analyzing the dispersion relation for arbitrary lateral Bloch vector components and studying the consequences for refraction and diffraction in imaging MMs where the fishnet structure serves as an example.

4.3.1 Iso-frequency contours of a fishnet

In the following section, a choice of different points of operation of the fishnet MM will be presented and discussed. These data will later serve to elaborate the fishnet with respect to its potential operation as a (perfect) lens device and as a medium exhibiting negative refraction. By that, it will be shown, that a negative phase velocity (or a negative effective index) is by no means a sufficient nor a necessary condition to observe any of these effects. For the sake of brevity, it is assumed in the following that the lateral Bloch vector component has only one non-vanishing component k_x ($k_y \equiv 0$). Furthermore, the following considerations will be restricted to beams which have a net polarization of the electrical field in y -direction. For this polarization, the FM exhibits a plasmonic resonance which exhibits a left-handed behavior around 208.8 THz as already discussed in Sec. 4.2. Resonances associated with a net polarization in x -direction occur at higher frequencies and are not discussed here.

Three different frequencies were selected in the following and a detailed investigation has been performed with respect to the spatial dispersion relation (iso-frequency curves) of the FM. The choice of these frequencies was motivated by the spectral behavior of the propagation constant as shown in Fig. 4.2a by the red line. The first value of $\nu_1 = 208.8$ THz ($\lambda_1 = 1.44 \mu\text{m}$) corresponds to the plasmonic resonance position for propagation along

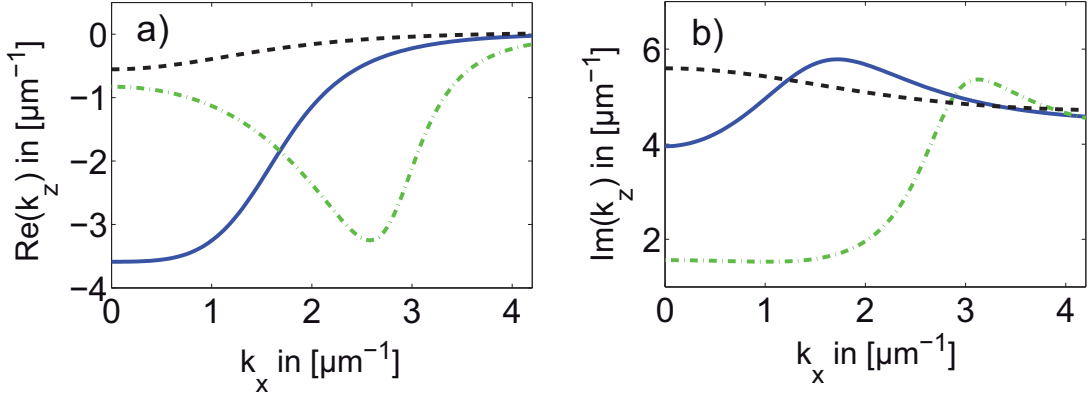


Figure 4.3: Real (a) and imaginary part (b) of the FM's angular dispersion relation (iso-frequency curve) $k_z(k_x)$ evaluated at three different wavelengths. Blue, solid: $\lambda_1 = 1.44 \mu\text{m}$; green, dashed-dotted: $\lambda_2 = 1.39 \mu\text{m}$; black, dashed: $\lambda_3 = 1.49 \mu\text{m}$.

the z -direction, i.e. the minimum of $\Re(k_z)$. The two other frequencies are slightly positively/negatively detuned from this spectral position, i.e., $\nu_2 = 216 \text{ THz} > \nu_1$ ($\lambda_2 = 1.39 \mu\text{m}$) and $\nu_3 = 201.9 \text{ THz} < \nu_1$ ($\lambda_3 = 1.49 \mu\text{m}$). The size of detuning will permit a meaningful qualitative distinction in the angular behavior, but its concrete size affects only quantitatively the observations. The corresponding dispersion relations (iso-frequency curves) $k_z(k_x)$ are shown in Fig. 4.3. These curves are symmetric with respect to k_x , i.e., $k_z(k_x) = k_z(-k_x)$. The k_x component of the Bloch vector is varied between zero and $4.2 \mu\text{m}^{-1}$ which is close to the vacuum wavenumber for the three wavelengths of interest. From Fig. 4.2 it can be seen that $\Re(k_z)$ approaches zero for $k_x \rightarrow 4.2 \mu\text{m}^{-1}$ in all three cases. In this limit the fishnet MM is driven out of resonance and it just mimics a diluted metal.

However, concentrating on the differences between the three iso-frequency contours shown in Fig. 4.3, it is evident that a shift from λ_1 to larger wavelengths, i.e. λ_3 , leads to an attenuation of the response of the fishnet MM since the resonance is no longer fully excitable. This becomes obvious because the two considered curves behave similar differing only by a scaling factor. In particular, both curves exhibit their minimum at normal incidence ($k_x = 0$) and vary monotonically with k_x . In strong contrast, a detuning of the wavelength from λ_1 to smaller values, i.e. λ_2 , causes the plasmonic resonance to be strongest excitable for an oblique direction. The iso-frequency curve $k_z(k_x)$ for λ_2 exhibits its minimum at $k_x \simeq 2.60 \mu\text{m}^{-1}$ and the curve shows a non-monotonic dependence on k_x . This has dramatic consequences for the imaging properties as it will be shown later. However, all presented results, in particular for λ_1 and λ_2 , do exhibit negative values for k_z in the entire angular domain just emphasizing the left-handed behavior of the FM.

Inclination and diffraction coefficients. In the following, we concentrate on two distinct frequencies where the choice was motivated by the preliminary results as discussed above. First, we choose $\lambda_1 = 1.44 \mu\text{m}$ and second $\lambda_2 = 1.39 \mu\text{m}$ because these two cases turned out to exhibit a quite remarkably different angular behavior (see Fig. 4.3). Results for λ_3 would have been similar to λ_1 , hence this wavelength is omitted. To proceed the analysis of the fishnet MM in terms of its properties concerning the propagation of beams, it is now natural to derive the inclination and diffraction coefficients. They were formally introduced in Sec. 3.3. Concentrating on the real part of the propagation constant k_z , Fig. 4.4 shows the relevant data. There, $\Re[k_z(k_x)]$ and the inclination coefficient $\xi'_1(k_x)$ as well as the diffraction coefficient $\xi'_2(k_x)$ are shown for the two wavelengths of interest. It is evident

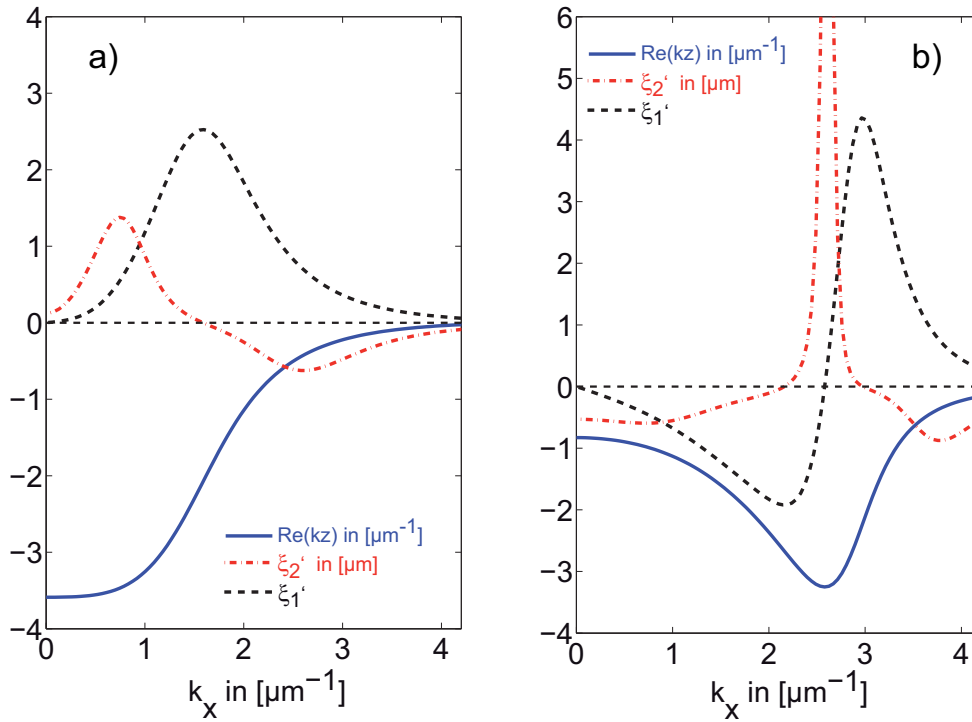


Figure 4.4: Iso-frequency curves (real part of k_z), the inclination parameter ξ'_1 and the diffraction coefficient ξ'_2 vs. the lateral Bloch vector component k_x for λ_1 (a) and λ_2 (b).

that the diffraction coefficient experiences rapid variations and even changes sign for both wavelengths. It can be further seen, that in the vicinity of normal propagation ($k_x = 0$) anomalous diffraction ($\xi'_2 > 0$) occurs only for λ_1 , whereas it is normal ($\xi'_2 < 0$) for λ_2 . There is only a small angular region around $k_x = 2.60 \mu\text{m}^{-1}$ where the fishnet exhibits anomalous diffraction also for this wavelength. On the other hand, the inclination coefficient ξ'_1 does not exhibit a simple monotonic behavior in neither case and it even changes its sign for λ_2 at $k_x = 2.60 \mu\text{m}^{-1}$. This will lead to large differences with respect to the imaging and

refractive properties of a fishnet slab as it will be discussed in the upcoming sections in detail. In particular, the fact that ξ'_1 may change its sign will lead to a transition from positive to negative refraction although the fishnet exhibits a left-handed behavior throughout the entire presented angular domain. This will be subject to deeper investigations in Sec. 4.3.3.

4.3.2 The fishnet slab and imaging of beams

A very promising and frequently invoked application of MMs is the perfect lens. This requires a MM slab with a unitary impedance, vanishing losses and an isotropic refractive index of $n = -1$, in particular for all lateral wave-vector components k_x . It allows the formation of a perfect image of a monochromatic source located in the front focus of a MM slab [3]. Let us briefly remind the basic properties of a perfect lens from a wave optical point of view.

On one hand, the exploited MM has to exhibit a spherical iso-frequency surface (at least at the operational wavelength) which provides a constant but anomalous diffraction in the propagating wave regime. By that, the phase curvature that a beam accumulates in free space (in front and behind the lens) will be compensated within the MM. Choosing the correct focal distance of the well-known perfect lens configuration (half of the slab thickness) the total diffractive spreading between the two focal points disappears. This working mechanism is illustrated in Fig. 4.5a. It can be well compared to the compensation of temporal dispersion of pulses as applied in optical telecommunication systems [156]. These considerations will facilitate the understanding of image formation and they will be the key in explaining the realistic imaging properties of the current fishnet structure.

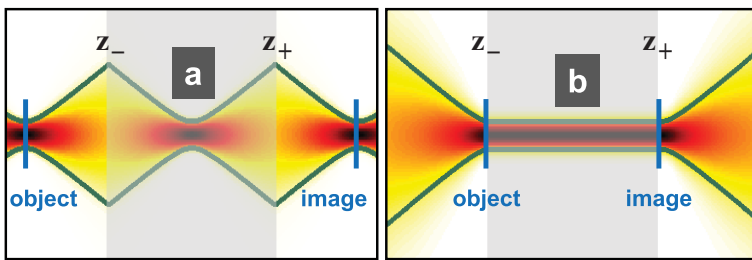


Figure 4.5: Schematic sketch of the image formation process by means of a MM with an isotropic refractive index (a) or which suppresses the diffractive spread of light (b).

On the other hand, the enhancement of evanescent waves – actually the more remarkable property of a perfect lens – is a pure surface related effect which takes advantage of surface states resulting in an effective and proper increase of all incident evanescent waves. These evanescent waves are crucial for obtaining sub-wavelength resolution. However, in the following discussion they are completely disregarded and the focus will be exclusively on the propagating wave regime. This is justified, as will be seen, since the performance of the fishnet MM as a lens is already limited by its impact on the propagating waves. Hence-

forth, it is of primary interest to analyze the consequences of the peculiar shape of the iso-frequency surfaces, as exemplarily displayed in Fig. 4.3, on the re-focusing capabilities of a finite fishnet slab deployed as a *conventional* lens. For that purpose, a suitable set of non-paraxial and diverging beams is chosen in the following. They will be impinging on a finite fishnet slab and the transmitted field will be analyzed in the half-space right after the slab device. However, the decision to apply a fishnet slab as a potential lens device is not just playing to the gallery. On the contrary, it is perhaps the only chance to access the associated dispersion properties also experimentally. The high attenuation which is expected for a beam propagating through the fishnet slab requires to use highly non-paraxial beams. The characteristic length, i.e. the Rayleigh length, after which a paraxial beam experiences considerable diffraction, will largely exceed the characteristic damping length $1/\Im(k_z)$ of the bulk fishnet material. Thus, there is a strong need to decrease the Rayleigh length, such that diffractive effects appear at the same length scale as the attenuation is doing.

Eventually and for the sake of completeness, it has to be mentioned that a perfect imaging may also be achieved with a MM slab exhibiting a completely flat angular dispersion $k_z(k_x)$. In that case, light propagates diffractionless at a constant attenuation, rendering the material amenable to a light tunneling scheme [152, 153]. This mode of operation is illustrated in Fig. 4.5b and it is later referenced in Sec. 4.4. However, also in that case the fishnet slab will likely be illuminated by non-paraxial beams due to the same reasons as explained above.

Angular transmission function. To investigate its pertinent imaging properties, the field originating from a finite object at $z = 0$ (the source position in front of the device) has to be propagated through a finite fishnet slab and the adjacent domains. In what follows the fishnet slab consists of 12 functional layers with an overall thickness of $d = 2.4 \mu\text{m}$. Moreover, the incident field distribution is assumed to be one-dimensional (line source), and linearly polarized in y -direction, i.e. $\mathbf{E} = E\mathbf{e}_y$ with $E(x, z = 0) \equiv E_0(x)$. By using the angular decomposition of this field, i.e. $E_0(k_x) = \frac{1}{2\pi} \int_{-\infty}^{+\infty} dx E_0(x) \exp(-ik_x x)$, its propagation to any position z behind the device can be represented by its angular spectrum as

$$\begin{aligned} E(x, z) &= \int_{-\infty}^{+\infty} dk_x E_0(k_x) \exp\{ik_z^{\text{FS}}(k_x z_-)\} T(k_x) \exp\{ik_z^{\text{FS}}(k_x)(z - z_+)\} \exp(ik_x x) \\ &\equiv \int_{-\infty}^{+\infty} dk_x E(k_x, z) \exp(ik_x x) \end{aligned} \quad (4.1)$$

with $k_z^{\text{FS}}(k_x) = \sqrt{(\omega/c)^2 - k_x^2}$ being the propagation constant in free space. Furthermore, z_- and z_+ denote the coordinates of the front and rear facet of the MM slab as depicted in

Fig. 4.5. $T(k_x)$ represents the angular transmission function of the MM slab relating the input and output plane wave components by $E(k_x, z_+) = T(k_x)E(k_x, z_-)$. Numerically, $T(k_x)$ is rigorously calculated by applying the FMM for the entire fishnet slab under consideration and by scanning the angular domain of interest. In particular, $T(k_x)$ corresponds to the transmission function of the zeroth diffraction order. Due to the sub-wavelength nature of the structure, this information suffices to determine the far field response of the structure. However, there is an alternative way to determine the slab's transmission function, at least approximately. Remembering the quite large damping of the overall slab structure, then the transmission function $T(k_x)$ can be calculated according to

$$T(k_x) = t_0(k_x)t'_0(k_x) \exp[ik_z(k_x)d]$$

in a very good approximation. Here, $t_0(k_x)$ denotes the transmission coefficient of a plane wave into the FM determined at a single interface. The primed quantity t'_0 represents the opposite scenario. Formally, these coefficients can be calculated by applying Eqn. (3.24) as described in Sec. 3.2. However, neglecting the influence of the single interface transmission coefficients t_0 and t'_0 for a moment, then the overall transmission function $T(k_x)$ is simply determined by

$$T(k_x) \approx T_{\text{DR}}(k_x) = \exp\{ik_z(k_x)d\}. \quad (4.2)$$

Equation (4.2) provides a simple yet approximate interrelation between the transmission coefficient of the finite structure $T(k_x)$ and the dispersion relation $k_z(k_x)$ of the bulk MM. Accordingly, the transmission of every angular component through the finite slab structure is approximated by the propagation of the connected FM over equal distance d within the bulk MM. To evaluate the validity of Eqn. (4.2), Fig. 4.6 shows a comparison between $T(k_x)$ and $T_{\text{DR}}(k_x)$ for both wavelengths of interest ($\lambda_1 = 1.44 \mu\text{m}$ and $\lambda_2 = 1.39 \mu\text{m}$). In general,

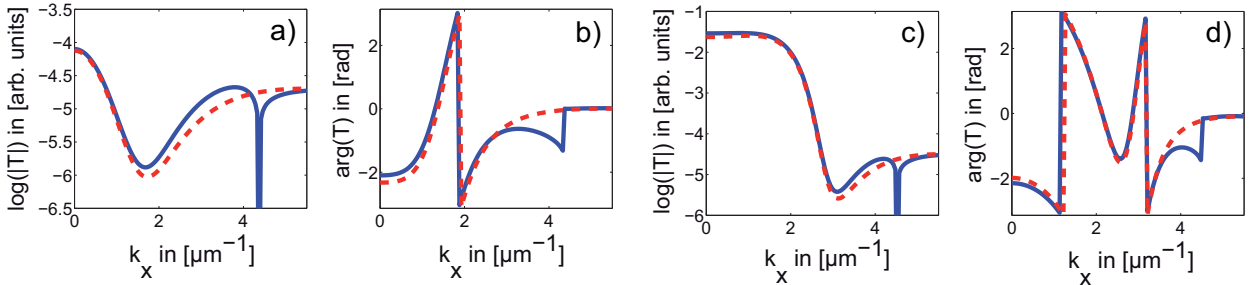


Figure 4.6: Logarithmic modulus and the phase of the transmission coefficient vs. the lateral Bloch vector component k_x for λ_1 in a) and b) and for λ_2 in c) and d). The blue, solid line corresponds to $T(k_x)$, whereas the red, dotted curve shows $T_{\text{DR}}(k_x)$.

both models coincide very well for both wavelengths. Only near grazing incidence where

$|T(k_x)|$ tends to zero ($\log |T| \rightarrow -\infty$) also qualitative differences can be observed for the two approaches. These deviations are attributed to the negligence of t_0 and t'_0 when calculating $T_{\text{DR}}(k_x)$. Thus, all succeeding numerical studies concerning the MM imaging properties will be performed using the rigorously computed transmission coefficient $T(k_x)$. The dispersion relation, and thus $T_{\text{DR}}(k_x)$, will only be used to back the numerical results by physical arguments. However, it will turn out that conclusions of both approaches agree perfectly.

Propagation schemes. In order to clearly distinguish the impact of different physical effects (damping, diffraction) it appears to be convenient to consider/define three different *abstract* calculation scenarios in the following. They are characterized by three different transmission functions – which correspond to three different levels of approximations – of one and the same structure.

- ▶ **Real scheme.** The so-called *real scheme* employs the complete complex transmission coefficient $T_{\text{R}}(k_x) = T(k_x)$. Thus, it accounts for all properties of the actual fishnet slab such as damping and diffraction effects.
- ▶ **Semi-real scheme.** The second scheme is the *semi-real scheme*. Attenuation is neglected so that effectively only the real part of the propagation constant, i.e. $\Re(k_z)$, is taken into account. Consequently, the associated transmission function will be calculated according to $T_{\text{SR}}(k_x) = \exp \{i \arg [T(k_x)] d\}$.
- ▶ **Semi-ideal scheme.** The third scheme serves as a benchmark by assuming the transmission function of an effectively homogeneous and isotropic material having $n = -1$ (circular iso-frequency curve). However, the complex transmission coefficient is approximated by $T_{\text{SI}}(k_x) = \exp \{-i \sqrt{\omega^2/c^2 - k_x^2} d\}$ for $k_x^2 \leq \omega^2/c^2$, and $T_{\text{SI}}(k_x) = 1$ otherwise, essentially representing the perfect lens except its effect on evanescent waves.

Gaussian beams. In what follows, the z -axis is assumed to be the principal direction of propagation. Without loss of generality, the source field is further assumed to be Gaussian, i.e.

$$E_0(x) = A_0 \exp \left(-\frac{x^2}{\sigma_x^2} \right), \quad \rightsquigarrow \quad E_0(k_x) \propto \exp \left(-k_x^2 / \sigma_k^2 \right), \quad (4.3)$$

where $\sigma_k = 2/\sigma_x$ denotes the angular spectral width. To characterize the pertinent imaging properties of a fishnet slab, a series of calculations with a varying spectral width σ_k were performed for normally and obliquely incident beams. In all situations, the waist of the incident beam was located $1.2 \mu\text{m}$ in front of the MM slab.

4.3.2.1 Anomalous diffraction regime – operating @ λ_1

Considering the propagation of paraxial beams, then the fishnet structure, operated at a wavelength of $1.44 \mu\text{m}$, exhibits anomalous diffraction for $k_x < 1.6 \mu\text{m}^{-1}$, diffraction-free propagation at $k_x = 1.6 \mu\text{m}^{-1}$ and normal diffraction beyond this point as depicted in Fig. 4.4a. However, in the following discussion we focus on normal incident, non-paraxial beams with a broad angular spectrum between $\pm 4.2 \mu\text{m}^{-1}$ and even broader. Thus, we want to evaluate the consequences of the non-ideal dispersion characteristics of the bulk fishnet on its imaging properties, where the term *imaging* refers to the re-focusing capabilities of incident and diverging Gaussian beams. As it was already mentioned, the decision to test the diffraction properties of the MM under consideration by means of highly non-paraxial beams instead of paraxial ones, is mainly motivated by the high attenuation which is expected for a beam propagating through the fishnet slab. Thus, it is highly desirable to balance the length scales on which diffraction and attenuation are characteristically appearing.

In the paraxial limit it is expected that the fishnet slab will indeed re-focus a normally incident beam due to the negative curvature of the iso-frequency contour (anomalous diffraction) around $k_x = 0$. But how does the structure perform for decreasing waist diameters σ_x going along with an increasing spectral width σ_k of the beam? Saying it in advance: re-focusing can be achieved in nearly all cases. However, a detailed investigation of this issue will give an important insight into the significance and the impact of the various dispersive properties of the fishnet structure. Hence, Tab. 4.1 provides an overview of a systematic parameter variation. The widths (FWHM) of the re-focused Gaussian beam at the rear focal position is shown there as a function of the spatial width of the incident beam. The focal position is not assumed to be predefined. Instead, it is identified as the point where the amplitude reaches its well-defined maximum at the optical axis measured in the half-space behind the fishnet slab.

In the *semi-ideal* calculation scheme, differences between input and output quantities can be clearly attributed to the missing evanescent waves which were neglected when calculating T_{SI} . Hence, T_{SI} will serve as a benchmark in the following since the discussion neglects the special impact on evanescent waves as already stated previously. In the *semi-real* scheme the achieved width of the re-focused beam becomes larger than in the semi-ideal one. Due to the fact that $|T_{\text{SR}}| = |T_{\text{SI}}|$, these differences can be attributed to the non-circular shape of $\Re(k_z)$, i.e. $\xi'_2 \neq \text{const}$. Obviously, these aberrations tend to increase the width of the image. Now, in order to close the gap between idealized and real MMs, losses have to be fully taken into account. Thus, the last column of Tab. 4.1 shows the relevant data. The smallest achievable focal width amounts to about $3.74 \lambda_1$ which is roughly three times larger than in the semi-real scheme. The large deviation may be explained by the strong

variations of the imaginary part of k_z , causing an inhomogeneous attenuation of all angular components. Then, the fishnet slab essentially acts as a low-pass filter, which becomes evident when inspecting $\Im(k_z)$ provided by Fig. 4.4a or equivalently using Fig. 4.6a for the modulus of the associated transmission function. The FWHM of the central transmission window is about $1.05 \mu\text{m}^{-1}$ corresponding to a FWHM of $3.46 \lambda_1$ in the spatial domain (Gaussian shape assumed). This value fits perfectly to the data presented in Tab. 4.1 and is close to the aforementioned limit of about $3.74 \lambda_1$. Consequently, the fishnet slab under consideration is mainly limited by the particular shape of the imaginary part of its iso-frequency contour and not by the dispersive properties of its real part. In retrospect, this justifies our initial assumption to neglect the influence of the evanescent waves and to concentrate on the propagating wave spectrum of the incident beam.

σ_k in $2\pi/\lambda_1$	FWHM in units of λ_1			
	input	semi-ideal	semi-real	real
1/10	5.33	5.33	5.33	6.47
1/6	3.21	3.21	3.27	4.86
1/3	1.59	1.59	1.70	3.97
2/3	0.79	0.85	1.32	3.74
1	0.53	0.71	1.21	–

Table 4.1: Calculated beam width (FWHM) in the focal plane of the fishnet slab for the different scenarios as described in the main body of the text for different incident beam widths. Additionally the spectral width σ_k of the input beam is given. No clear focus position could be identified for the *real scenario* at $\sigma_k = 2\pi/\lambda_1$.

of incident beams. The upper row belongs to a beam with a FWHM of $1.59 \lambda_1$ and the lower one is associated to a value of only $0.53 \lambda_1$.

In principle, the chosen examples exactly reflect the special characteristics as already discussed above. In particular, the crucial low-pass filtering effect as it appears for the real slab structure becomes clearly visible. However, when reaching the limit of very small waist diameters of the incident beam (third row of Fig. 4.7) this low pass filtering may also lead to some kind of stabilization of the field distribution as it can be seen when comparing the semi-real and the real calculations scenarios. Beam distortions become very strong when the losses are neglected. This indicates the crucial effect of the non-spherical shape of the

To better understand the influence of different parameters, Fig. 4.7 shows some selected amplitude distributions calculated behind the considered fishnet slab. In all cases, the beam propagates in z -direction and the position $z = 0$ coincides with the MM's rear interface. The three different columns correspond to the three different propagation schemes. From left to right these are: T_{SI} , T_{SR} and T_{R} . Now, concentrating on the particular meaning of the rows, the central row shows the associated transmission function for better understanding. The rows on top (bottom) correspond to two different choices

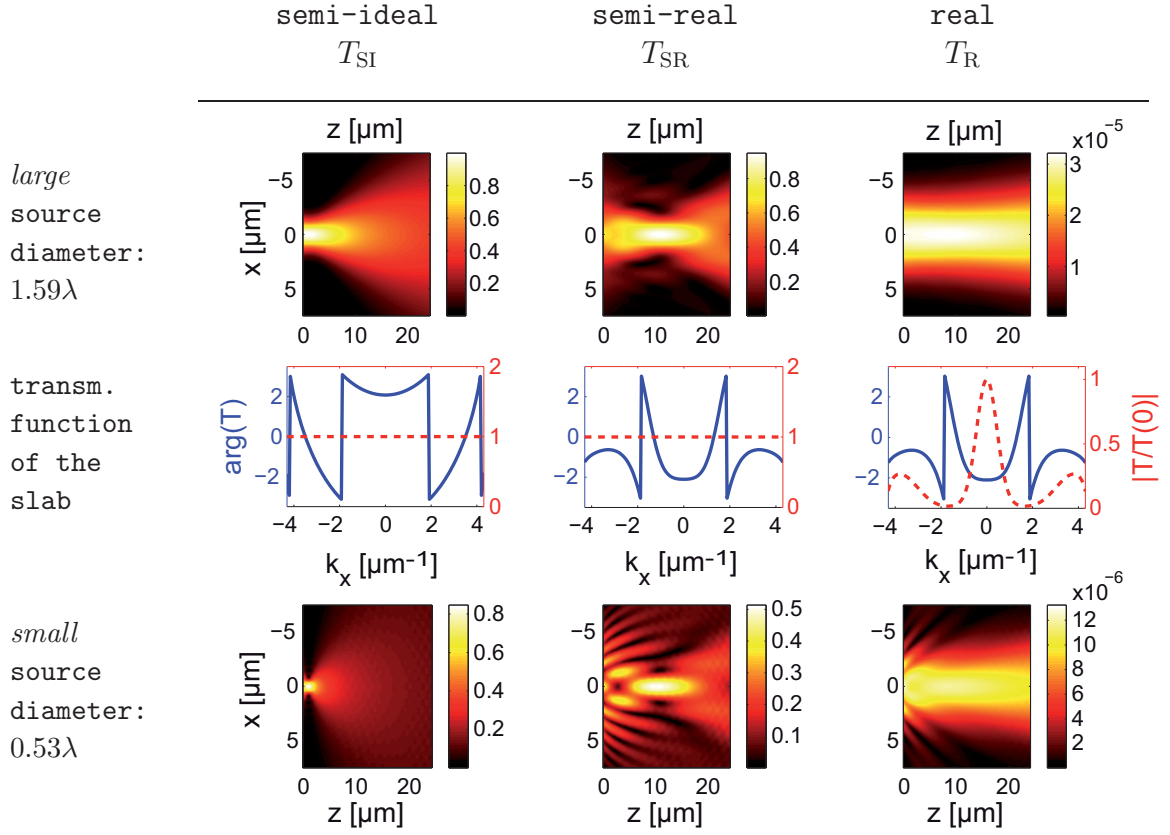


Figure 4.7: Amplitude distributions of the field transmitted through the MM slab at normal incidence for $\lambda_1 = 1.44 \mu\text{m}$. top row: source's FWHM is $1.59 \lambda_1$ ($\sigma_k = 1/3 \times 2\pi/\lambda_1$); bottom row: source's FWHM is $0.53 \lambda_1$ ($\sigma_k = 2\pi/\lambda_1$). middle row: phase (blue, solid) as well as the normalized modulus (red, dashed) of the respective MM slab transmission function. The different columns reflect the three different transmission functions used to calculate the field distributions. First column: T_{SI} , second column: T_{SR} , third column: T_R .

iso-frequency curve and especially that ξ_2' changes sign for large incident angles.

4.3.2.2 Normal diffraction regime – operating @ λ_2

Now, let us slightly decrease the operating wavelength to $\lambda_2 = 1.39 \mu\text{m}$. Despite the fact that the fishnet MM still exhibits a left-handed behavior, diffraction is now normal around $k_x = 0$ as already discussed in context of Fig. 4.4b. Hence, normally incident beams cannot be focused by a MM slab at this frequency. Although not explicitly shown, this behavior was indeed proven by numerical simulations similar to the one shown before. In neither case a re-focusing of the incident beam could be achieved behind the fishnet slab. Instead, the

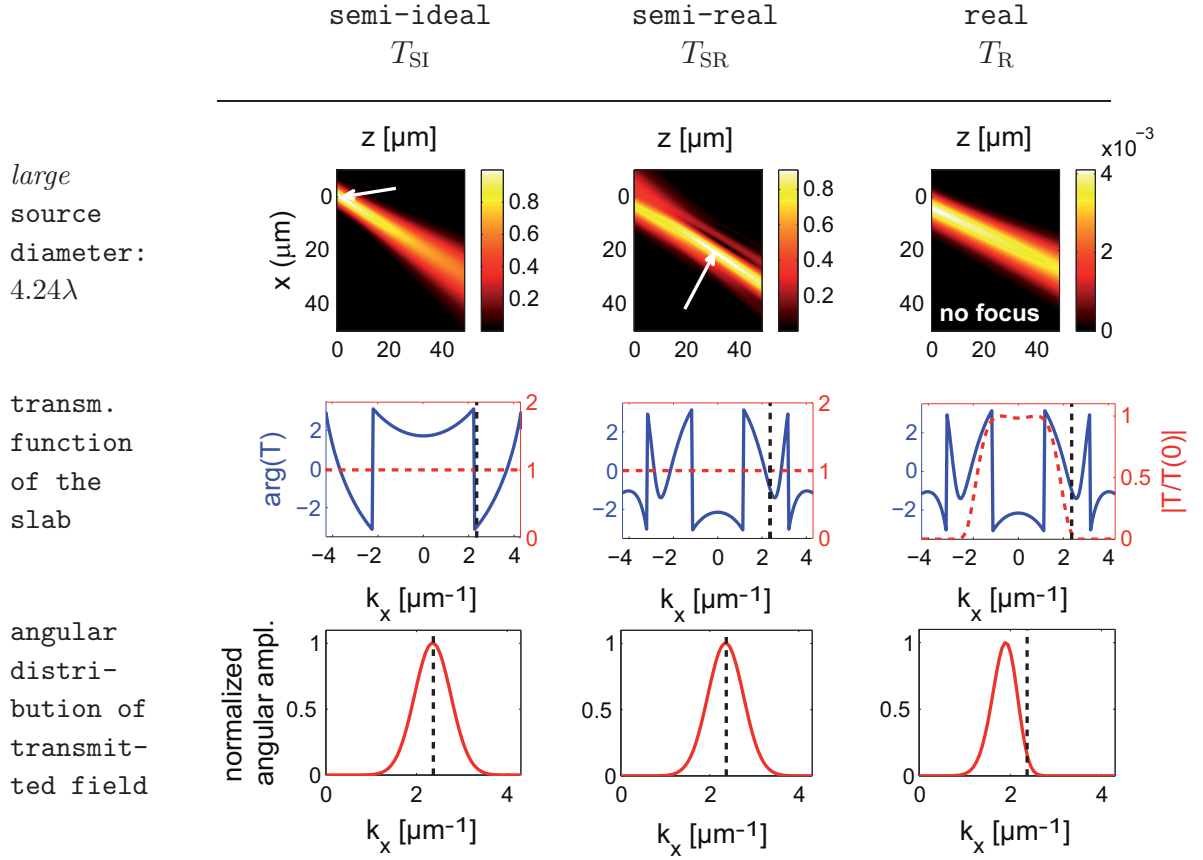


Figure 4.8: Top row: Amplitude distributions of the field transmitted through the MM slab at oblique incidence $k_x^0 = 2.4 \mu\text{m}^{-1}$ for $\lambda_2 = 1.39 \mu\text{m}$. The source's spectral width is $\sigma_k = 1/8 \times 2\pi/\lambda_2$ corresponding to a FWHM of $4.24 \lambda_2$; middle row: phase (blue, solid) as well as the normalized modulus (red, dashed) of the respective MM slab transmission function; bottom row: normalized angular spectrum of the transmitted field directly at the back facet ($z = 0$) of the MM slab. The black, dashed line indicates the mean lateral wave-vector component k_x^0 of the incident beam. The different columns reflect the three different transmission functions used to calculate the field distributions. first column: T_{SI} , second column: T_{SR} , third column: T_R

smallest measurable waist was always located directly at the exit facet of the device. This investigation clearly demonstrates that a negative phase velocity or a left-handed behavior of the medium must not be associated with negative refraction and anomalous diffraction. This conclusion goes along with the mesoscopic size of the applied fishnet MM which is far away from being a local, effective homogeneous material. However, inspecting the diffraction coefficient in more detail, there exists a narrow region, i.e. $2.15 \mu\text{m}^{-1} < k_x < 3.0 \mu\text{m}^{-1}$, where anomalous diffraction occurs (see Fig. 4.4). Thus, focusing may be achieved for obliquely incident beams, but due to the strong changes of the diffraction coefficient the

imaging quality is expected to be poor.

This has been numerically verified and the results are shown in Fig. 4.7. The incident beam has a mean lateral wave-vector of $k_x^0 = 2.4 \mu\text{m}^{-1}$ for the illuminating Gaussian beam. The comparison between the semi-ideal and the semi-real calculations shows strong deviations of the beam's propagation characteristics. The white arrow marks the corresponding focal positions. Especially, the large difference in the focal distances may be attributed to the huge variation of the diffraction coefficient used for the semi-real calculation scheme. However, the validity of our basic assumption is once again confirmed, that is that anomalous diffraction leads to a re-focusing of an incident diverging beam.

But, as a drop of bitterness one has to recognize, that there is apparently no focal point which can be identified in case of the real calculation scheme which means that losses are now fully taken into account. Consequently, this behavior must be attributed to the effect of the imaginary part $\Im(k_z)$ of the propagation constant. When carefully looking at Fig. 4.3, it can be seen that $\Im(k_z)$ has a strong gradient exactly in the considered anomalous diffraction regime around $k_x = 2.4 \mu\text{m}^{-1}$. Hence, the linear Taylor expansion coefficient ξ_1'' (see Sec. 3.3) cannot be neglected anymore. Effectively, the first momentum of the spectrum and so the principal propagation direction is significantly shifted towards lower angles. This is illustrated in the third row of Fig. 4.8. The dashed vertical line indicates the mean lateral component of the wave-vector of the incident field, i.e. $k_x = 2.4 \mu\text{m}^{-1}$. The red curves in all three pictures show the normalized angular spectrum of the transmitted field calculated at the exit facet of the slab. In contrast to the semi-ideal and the semi-real calculation scheme, the angular center is shifted to lower values. Thus, the principal spectral component is now located outside the anomalous diffraction regime (ξ_2' becomes negative) preventing the re-focusing of the input field. Hence, the peculiar interplay between the effects caused either by the real and the imaginary part of the propagation constant hinders the image formation in this particular situation.

4.3.3 Refraction of paraxial beams

A beam propagating through any medium experiences diffraction. On the contrary, beam refraction appears only at the interface between two media. In this section it is likewise shown how to exploit the dispersion relation to explain refraction at MM surfaces. Thus, a paraxial beam[‡] is considered which is obliquely incident onto a MM slab. In a geometrical picture, the beam experiences a displacement Δ while propagating through the MM slab. A schematic is provided in Fig. 4.9a. The displacement Δ is directly related to the beam's

[‡]An angular width of $\sigma_k = 1/25 \times 2\pi/\lambda$ for the incident beam was used in the following numerical calculations. It shows negligible diffraction over the considered propagation length.

angular direction θ_2 inside the slab, i.e. $\Delta = \tan(\theta_2)d$, with d being the thickness of the slab. In this simple yet intuitive picture, multiple reflections inside the slab structure are neglected. In case of a slab medium with a sufficiently large absorption, which holds for the considered fishnet structure, this assumption appears to be realistic. Thus, by assuming the incident angle θ_1 to be positive, negative refraction occurring at the front facet of the slab translates into a negative beam displacement Δ and vice versa.

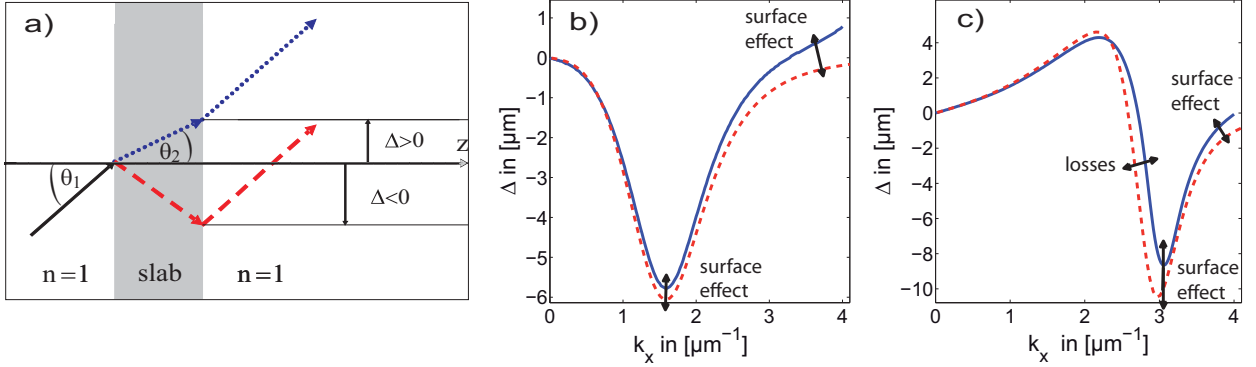


Figure 4.9: Schematic (a) of a paraxial beam propagating through a thin MM slab. Refraction at the first interface leads to a beam displacement Δ at the second interface. In particular, negative or positive refraction can be identified by a positive or negative beam displacement assuming that $\theta_1 > 0$. Calculated displacements Δ of the transmitted field at the rear interface of the MM slab as a function of the incident beam's mean wave-vector component k_x calculated for λ_1 (b) and λ_2 (c), respectively. The blue, solid lines represent the results of rigorous calculations performed on the finite slab structure, whereas the red, dashed curves rely on the inclination coefficient ξ'_1 of the bulk fishnet MM.

By considering a slab consisting of a homogeneous and isotropic material, then the sign of the observed beam displacement Δ would be strictly related to the sign of the slab's refractive index n , i.e. its phase velocity. In the more general case, which is the refraction between two arbitrary but periodic media, the angle of refraction is no longer governed by the phase velocity specific to the associated media. Instead, the refractive behavior must be solely described in terms of the angular dispersion relation. The basic mechanisms were discussed in Sec. 3.3. Thus, the sign of the inclination coefficient $\xi'_{1,MM}$ of the slab's material dictates the sign of the expected beam displacement. However, if strong losses are involved, as in the present fishnet MM, similar angular filtering effects as already discussed in the previous section may interfere with this model. This can be circumvented, by considering paraxial beams with sufficiently large waist diameters. Then, the whole beam approximately experiences a constant damping during propagation with negligible impact on the beam's profile. Nevertheless, in the following calculations the influence of damping will be fully taken into account and its consequences are pointed out.

After this brief introduction, the formerly introduced fishnet slab will now be likewise analyzed for the two known wavelengths $\lambda_1 = 1.44 \mu\text{m}$ and $\lambda_2 = 1.39 \mu\text{m}$. The associated inclination coefficients ξ'_1 are already displayed in Fig. 4.4. For both wavelengths the phase velocity is negative in the entire angular domain. In contrast, the inclination coefficient ξ'_1 reasonably differs between the two considered cases. It is entirely positive for λ_1 indicating the fishnet slab to show negative refraction (or likewise a negative beam displacement Δ) for beams incident between $\pm 90^\circ$. On the other hand, ξ'_1 is negative for λ_2 starting from normal incidence, has a zero at $k_x = 2.60 \mu\text{m}^{-1}$ and then it becomes positive for larger lateral Bloch vector components k_x . This leads to the conclusion that negative refraction appears only for large incident angles where ordinary refraction occurs, in particular, for small angles around normal incidence.

To verify this statement, rigorous numerical calculations were performed for a paraxial Gaussian beam possessing an angular width of $\sigma_k = 1/25 \times 2\pi/\lambda$ and a mean wave-vector k_x which varies between normal and grazing incidence. The surrounding medium is assumed to be air such that the angle of incidence θ_1 is determined by $k_x = 2\pi \sin(\theta_1)/\lambda$. Once again, the FMM was used to perform the calculations for the finite structure. The beam displacement is measured as the difference of the beam's center of gravity at the front and the rear interface of the MM slab, respectively. The corresponding results are presented in Fig. 4.9 by the blue solid curves. For comparison, Fig. 4.9 also displays the approximated results $\Delta = -\xi'_1 d$ by relying only on the inclination coefficient ξ'_1 of the bulk fishnet MM (see the red graphs). First concentrating on Fig. 4.9b, both curves agree very well except for large angles approaching grazing incidence ($k_x > 3.5 \mu\text{m}^{-1}$) and around the local minimum position. There are two potential reasons for these deviations. First, they may be attributed to the effect of losses ($\xi''_1 \neq 0$) and, second, they may be attributed to additional beam displacements originating from the front and rear surface of the slab. To be more precise, these surface related beam displacements are commonly known as Goos-Hänchen and Imbert-Fedorov shifts. Historically, they are introduced when considering the interface between two homogeneous dielectrics, and there they only occur under total internal reflection [157–159]. In the more general case, they are not restricted to appear only under this condition which is the case in the current example. However, due to a thorough analysis of the considered example[§], it can be concluded that losses affect the overall transmittance,

[§]To explain the differences between the results of the rigorous calculations and those predicted by exclusively relying on the inclination coefficient ξ'_1 , one carefully has to distinguish between the effect of losses introduced by the bulk MM and the referenced surface effects. Mathematically, the beam displacements occurring strictly at the surface can be uniquely attributed to the peculiar shape of the single interface transmission coefficients t_0 and t'_0 . Hence, the magnitude of the surface induced beam displacements can be uniquely determined by the comparison of the rigorous results (achieved by using T_R as introduced in Sec. 4.3.2) and the approximated transmission function T_{DR} according to Eqn. (4.2). T_{DR} neglects

but they do only slightly influence the refraction. On the contrary, as indicated by the labels in Fig. 4.9b, the occurring deviations originate from the effect of the rear and/or the front interface of the MM.

Now, turning over to the results for the second wavelength λ_2 . At first, the geometrical model well coincides with the rigorous calculations, too. In particular, the beam displacement is positive for small incident angles and it then becomes negative for $k_x \approx 2.6 \mu\text{m}^{-1}$. The small deviations in this region can be attributed to the strong gradient of the propagation constant's imaginary part ($\xi_1'' \gtrless 0$), whereas around grazing incidence surface effects are once again responsible as it also indicated by the labeled arrows within the corresponding figure.

Conclusions. Summarizing this section, it must be concluded that refraction appearing at the considered fishnet structure, is perfectly consistent with predictions relying on the dispersion relation of the FM of the associated bulk MM. The presented description perfectly fits to the mesoscopic nature of contemporary optical MMs, in particular the fishnet structure, and it provides reliable results. Most notably, there appears a strong modification in the characteristic refraction at the fishnet's interface when the operating wavelength is only marginally modified. More precisely, a variation of only 50 nm in the operating wavelength turns the refraction characteristics from initially being negative to become positive over a large angular region although the phase velocity remains negative.

4.4 Advanced metamaterials – the super-cell approach

As it was elaborated in great detail within the last section, the peculiar characteristics of the considered fishnet structure significantly prevent this MM from being "perfect". In particular, the distinct shape of the propagation constant's real and imaginary part had limited a slab device in its performance with respect to its potential application as a (perfect) lens. Thus, a reasonable design approach to improve this particular MM structure, but also all MMs in general, should rely on the desired optical response. It appears to be desirable to mould the dispersion relation of the underlying bulk MM such that it better fits to the requirements of the particular field of application/operation. A solution to this problem is not straightforwardly at hand. However, the results to be presented in this section try to lift these limitations in a twofold way. Conceptually, a procedure is suggested to design MMs with a predefined characteristic of light propagation, characterized by their dispersion

the single interface transmission coefficients t_0 and t'_0 but takes into account the losses for the propagation through the bulk MM. To sum up, in doing this analysis very carefully, the final results can be interpreted as it is shortly summarized in the main body of the text.

relation. Optically, it will be shown that the former fishnet MM can be optimized such that it finally exhibits either an isotropic response or that it even permits diffractionless propagation.

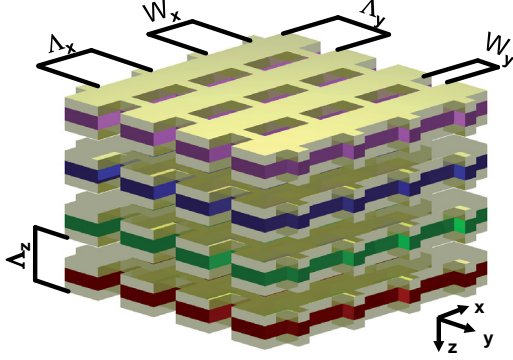


Figure 4.10: Schematic of the super-cell fishnet MM. The geometrical parameters explicitly highlighted in the figure were kept constant within each optimization. In case of the MM providing an isotropic optical response (circular iso-frequency curve) they are $\Lambda_x = \Lambda_y = 600$ nm, $\Lambda_z = 200$ nm, $W_x = 500$ nm, and $W_y = 284$ nm. In the second case (diffractionless optical MM) the parameters are $\Lambda_x = \Lambda_y = 300$ nm, $\Lambda_z = 200$ nm, $W_x = 250$ nm, and $W_y = 140$ nm.

parameters, such that the optical response of the MM matches with sufficient precision the desired one.

In the present contribution these additional degrees of freedom are exemplarily introduced by considering MMs composed of super-cells. The relevant geometry, with a fishnet structure being the basic pattern, is shown in Fig. 4.10. A super-cell is formed by stacking four functional fishnet *sub-layers* in z -direction. These functional sub-layers slightly differ in their metallic as well as dielectric spacer thicknesses which represents the additional degrees of freedom. In lateral direction the structure's extension is maintained such that the overall volume of the unit cell of the super-cell fishnet structure is given by $\Lambda_x \times \Lambda_y \times 4\Lambda_z$. In what follows, the goal is to optimize the additional free parameters, i.e. metallic and spacer layer thicknesses, of all sub-layers individually such that the MM exhibits the predefined optical properties. Two relevant examples will be outlined. The first one concerns the design of a MM exhibiting a dispersion relation with a circular iso-frequency curve being equivalent

According to the previous treatments of this thesis, again, the dispersion relation $k_z(k_x, k_y, \omega)$ of the FM of a bulk MM is investigated. Departing from that, one can impose desired constraints such as an isotropic optical response (a spherical shape with constant curvature) or even a real and imaginary part of the propagation constant k_z , which does not depend on the lateral one. The former feature will allow, e.g., for the improvement of the imaging properties of a MM slab (as already discussed in Sec. 4.3 in detail), whereas the latter one causes light to propagate diffractionless at a constant attenuation, rendering the material amenable to a light tunneling scheme for the purpose of imaging. To achieve these goals the degrees of freedom defining a MM have to be increased. Numerical optimization techniques may be subsequently applied to find an optimum set of

to an effective medium with $n_{\text{eff}}(k_x) = -1$. The second one will be a MM where light propagates diffractionless.

4.4.1 A fishnet exhibiting a circular angular dispersion

For referential purpose, Figs. 4.11a and 4.11b shows the real and imaginary part of the propagation constant $k_z(k_x, 0, \omega = \text{const.})$ at a fixed wavelength for the original fishnet structure (black dashed line) as it was already introduced and discussed in Sec. 4.3. All

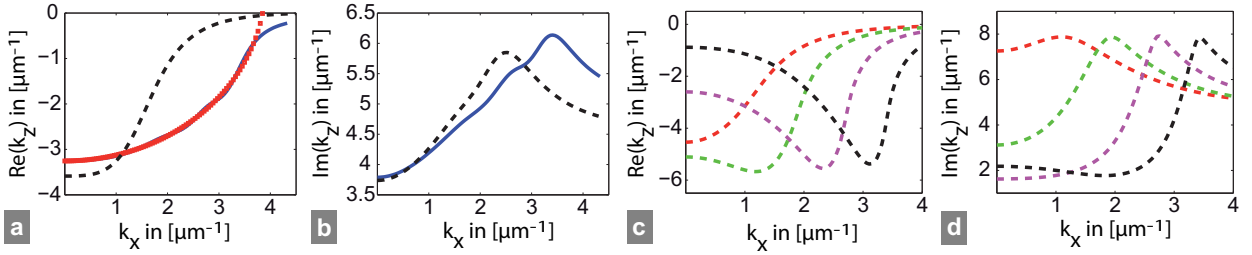


Figure 4.11: Real (a) and imaginary (b) part of the propagation constant k_z as a function of the lateral Bloch vector component k_x (iso-frequency contour) for the original fishnet (black dashed line) and the optimized super-cell structure (blue solid line). The best circular fit is superimposed (red dotted line). For referential purposes, the real (c) and imaginary (d) part of the propagation constant $k_z(k_x)$ associated with four individual bulk media (indicated by different colors) is shown. In each case, these media are defined by one of the single functional sub-layers of the optimized structure.

functional sub-layers are identical. The metal is silver and its material properties were calculated according to a Drude dispersion formula (see Sec. 4.2). At the chosen wavelength of $1.44 \mu\text{m}$ the real part of k_z assumes its largest negative value at normal incidence. All simulations are again performed by relying on the FMM. The polarization is again assumed to be along the y -direction being the proper polarization for the fishnet to show the desired left-handed behavior.

The performance of an ordinary fishnet slab being exploited as a *conventional* lens was already discussed in Sec. 4.3.2. However, Fig. 4.12a shows the contrast function which is expected for the imaging of two spatially separated, one-dimensional Gaussian beams. The overall fishnet slab is extended over 12 functional sub-layers (3 super-layers). The waist of the incident field is assumed to be located $1.2 \mu\text{m}$ in front of the device with a field distribution according to $[\mathbf{E} = E(x, z)\mathbf{e}_x$ with $E_0(x) \equiv E(x, z = 0)]$

$$E_0(x) = \exp\left[-\frac{(x - S_x)^2}{\sigma_x^2}\right] + \exp\left[-\frac{(x + S_x)^2}{\sigma_x^2}\right].$$

The quantity $2S_x$ denotes the beam separation. The field is assumed to be a line source emitting linearly polarized light in y -direction (for detailed explanation see also the dis-

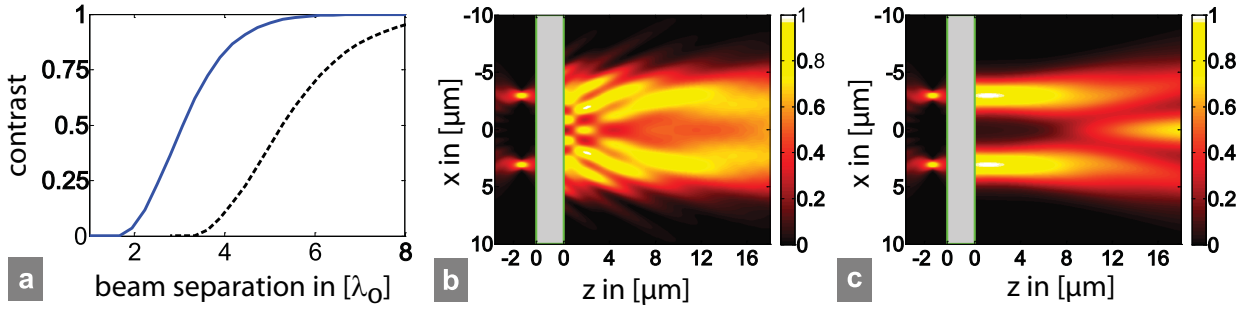


Figure 4.12: a) The emerging contrast in the object plane upon imaging of two Gaussian beams as function of their initial separation (original fishnet: dashed line; super-cell: solid line). Image formation of two closely spaced (separation of 6 μm) sub-wavelength Gaussian beams ($\sigma_x = 2\lambda/(2\pi) = 0.46 \mu\text{m}$) by a 2.4 μm -thick ordinary (b) and optimized (c) fishnet MM slab. The intensity scale on the left and on the right of the structure is independently normalized to unity for better visibility. For the purpose of the contrast function measurements, the waist width of a single Gaussian beam was chosen to be $\sigma_x = 2\lambda/(2\pi) = 0.46 \mu\text{m}$ or $\sigma_x = 6\lambda/(2\pi) = 1.37 \mu\text{m}$ in case of the optimized or ordinary structure, respectively.

cussion around Eqn. (4.3) in Sec. 4.3.2). The waist width σ_x of a single beam was set to $6\lambda/(2\pi) = 1.37 \mu\text{m}$. For smaller values the introduced beam distortions in the transmitted field become too large and a clear determination of the backside foci becomes impossible. Furthermore, the contrast function C was calculated according to

$$C = \frac{|E(x_f; z_f)|^2 - |E(0; z_f)|^2}{|E(x_f; z_f)|^2 + |E(0; z_f)|^2}$$

with (x_f, z_f) denoting the position of the focus being detected in the half-space behind the structure[¶]. As can be seen from Fig. 4.12a, the image contrast quickly deteriorates with smaller beam separation. As it was discussed in Sec. 4.3.2, the peculiar shape of the angular dispersion characteristics limits the resolution of the ordinary fishnet slab. In the considered example it only amounts to about 4λ .

Now, by relying on the super-cell approach and by applying a numerical optimization routine, the thicknesses of the metal and the dielectric layers of each fishnet sub-layer were optimized individually while the remaining parameters were kept constant. The target function was a circular iso-frequency contour for the real part of the Bloch vector, comparable to that of an isotropic medium with $n = -1$. It suggests that optimization is only performed for the propagating part of the Bloch vector spectrum^{||}. All geometrical param-

[¶]Of course, in general there exist two foci with coordinates (x_f, z_f) and $(-x_f, z_f)$ above and below the optical axis. However, due to the symmetry of the illuminating field it does not matter which of them is used for the calculation of the contrast function.

^{||}The optimization process was done in two steps. At first, an initial set of data was manually suggested on qualitative grounds. This was done by systematically analyzing the angular dispersion relation of an

eters of the optimized structure are documented in Tab. 4.2. The resulting iso-frequency curve along with a best circular fit is shown in Fig. 4.11. The effective index of the medium corresponding to the radius of the best fit amounts to $n_{\text{eff}} = -0.92$. In passing, we note that although the medium acts optically nearly isotropic within the particular angular region ($k_x = \pm 3.5 \mu\text{m}^{-1}, 0$), the geometry of the unit cell is not. The isotropic response is achieved by globally balancing the dispersive characteristics between all functional sub-layer. To verify that the final dispersion relation is really a genuine property of the super-cell structure, Figs. 4.11c and 4.11d also provide dispersion relations of four different ordinary (no super-cell) bulky fishnet MMs. In each case, the geometrical layout is just chosen to be identical to one of the four functional sub-layer of the optimized super-cell structure. As it can be clearly seen, the resonance positions of the individual fishnet structures** are nicely distributed throughout the angular domain. Hence, it must be concluded, that the peculiar interaction between the sub-layers leads to the resulting dispersive properties of the super-cell structure, since non of the individuals shows the desired broad circular shape.

a				b			
#l	d_m in [nm]	d_{ds} in [nm]	ϵ_{ds}	#l	d_m in [nm]	d_{ds} in [nm]	ϵ_{ds}
1	75.0	29.7	1.90	1	49.8	40.0	9.21
2	72.4	27.9	1.90	2	52.1	40.0	9.70
3	74.1	26.0	1.90	3	33.4	40.0	11.05
4	76.9	24.2	1.90	4	34.3	40.0	11.06

Table 4.2: Detailed overview of the structural parameters for the optimized fishnet MMs which exhibit either a nearly circular iso-frequency contour (a) or diffractionless propagation (b). l denotes the sub-layer index. d_m and d_{ds} denote the thicknesses of the metallic and dielectric spacer layers. ϵ_{ds} is the permittivity of the dielectric spacer.

In the following the optimized super-cell fishnet structure will be likewise applied as a finite

ordinary fishnet structure depending on all relevant geometrical parameters, as there are the thicknesses of the dielectric and metallic layers. From these solutions a first educated guess for the arrangement of the functional sub-layers in the super-cell was derived. This was done by assuming that the mean value of the individual sub-layers' dispersion relations matches the predefined criteria. However, this rather simplistic approach did not provide satisfying results and it was subsequently used as the starting point for a numerical optimization routine. For this purpose a pre-defined nonlinear least-squares optimization method was used (subspace trust-region algorithm based on the interior-reflective Newton method [160]) which is part of the MATLAB[®] software environment [161]. By that procedure, about 15 iterations (which correspond to 135 evaluations of the structures response) were usually required to approach the optimized solutions.

**The resonance positions are understood to be defined by the positions of the local minima of the real part of the propagation constant, namely $\Re(k_z)$.

slab device to test its performance for the purpose of imaging. The entire structure consists of 3 super-layers with an overall thickness of $2.4 \mu\text{m}$. The contrast function achievable for two Gaussian beams imaged by this optimized MM slab is shown in Fig. 4.12a. It can be seen that the resolution is almost doubled, although it has not yet reached the sub-wavelength regime. The major reason for this is the yet remaining angular-dependent absorption, rendering the structure to maintain its low-pass filtering characteristics. However, this restriction can be further lifted by imposing additional constraints on the imaginary part of the propagation constant k_z . To get a better impression of the superiority of the super-cell fishnet over the conventional structure, Figs. 4.12b and 4.12c additionally shows the calculated field distributions in front of and behind the MM slab device. The waist width of a single beam was in the sub-wavelength region ($\sigma_x = 2\lambda/(2\pi) = 0.46 \mu\text{m}$ each) and their separation amounted to $6 \mu\text{m}$. As it can be seen, for the ordinary fishnet the spots are not resolved, whereas the super-cell fishnet allows for their clear, but not perfect imaging.

4.4.2 A fishnet exhibiting a flat angular dispersion

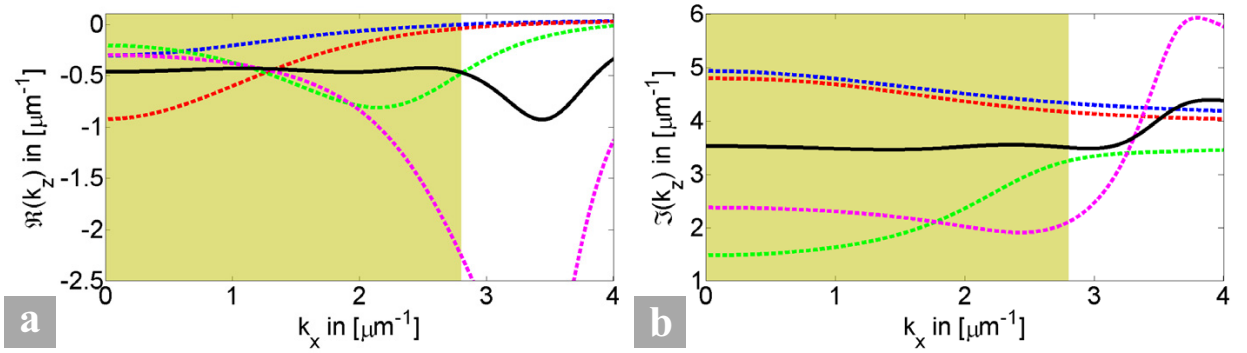


Figure 4.13: Real (a) and imaginary (b) part of k_z as function of the lateral Bloch vector component, k_x , (iso-frequency contour). The black, solid line displays the optimized super-cell structure. Target function of the optimization was a constant propagation constant k_z . The optimization criteria were enforced in a k_x -interval corresponding to the shaded area. The colored, dashed curves show the dispersion relations $k_z(k_x)$ of four individual bulk media (indicated by different colors) for referential purposes. In each case, these media are defined by one of the single functional sub-layers of the optimized structure.

To demonstrate that the constraints imposed on the desired optical performance of the super-cell MM can be rather freely chosen we are now aiming at achieving diffractionless propagation or self-collimation, respectively. In the following example, it will turn out that the light tunneling scheme will be even superior to the previously considered lens concept for the purpose of imaging.

The same ordinary fishnet structure used in the previous section serves again as the starting

point for the optimization procedure. The operating wavelength is $1.44 \mu\text{m}$. However, to achieve a MM that supports diffractionless propagation, the target function is now a propagation constant (real and imaginary part of k_z) that is independent of the lateral component k_x . The optimized iso-frequency curves are shown in Fig. 4.13 and the geometrical parameters are documented in Tab. 4.2 in detail. The optimization was enforced in an interval between zero and $k_x = 2.8 \mu\text{m}^{-1}$ (indicated by the shaded region). The optimization results in an imaginary as well as real part of the propagation constant which become approximately constant within the target region. The deviations from the mean value only amount to a maximum value of $0.025 \mu\text{m}^{-1}$ and $0.05 \mu\text{m}^{-1}$ for the real part and the imaginary part, respectively. If both quantities would be perfectly constant, each component of the plane wave spectrum of a finite object would exhibit the same phase advance and dissipation upon traversing the MM slab. Hence, the field distribution at the front and rear interface of a slab device consisting of that MM would be identical. They would only be scaled by an overall amplitude and phase factor. A verification of almost diffractionless propagation through the optimized MM is documented in Fig. 4.14. There, two closely spaced sub-wavelength Gaussian beams ($\sigma_x = 0.46 \mu\text{m}$) were placed at the front interface of the slab device. The field distribution at the exit facet for a MM slab thickness of $2.4 \mu\text{m}$ (three super-cells) and of $4.8 \mu\text{m}$ (six super-cells) reveals that diffraction inside the slab device is indeed negligible. This becomes even more obvious, when the field distribution is compared to those which will be achieved upon free space propagation over the same distance.

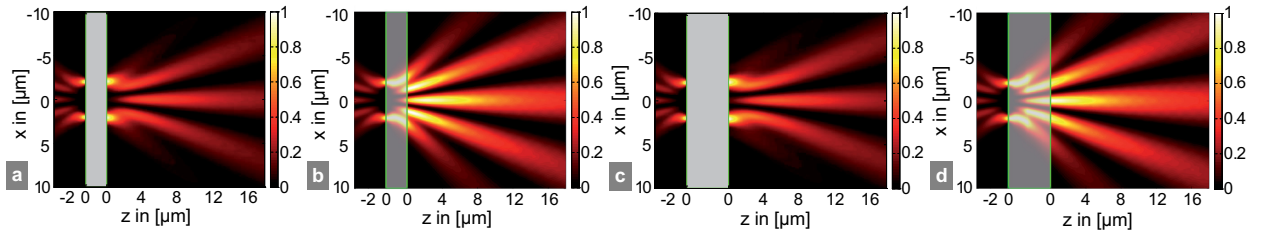


Figure 4.14: The electrical amplitude distribution around an optimized fishnet slab consisting of three (a) or six (c) super-cells. The illuminating field is a double Gaussian beam ($\sigma_x = 0.46 \mu\text{m}$, $\lambda = 1.44 \mu\text{m}$). The grey boxes indicate the MM slab structure. For better visibility the fields on the left and on the right of the structure are normalized individually. The beam separation is $4 \mu\text{m}$. The waist position of the incident field is located at $z = 0$ (front interface). For comparison, two field distributions are additionally shown which correspond to the scenario that the MM slab is removed and the field propagates over equal distances of $2.4 \mu\text{m}$ (b) and $4.8 \mu\text{m}$ (d) in free space, respectively. The substitution of the original MM slab is indicated by the transparent boxes. For the sake of better visibility the field on the left and on the right of the "virtual structure" is again normalized. The field within the box is normalized for every z -position individually to ensure a smooth transition of the coloring.

Conclusions. In conclusion, it was shown that MMs can be tailored to a large extent to exhibit certain optical functionalities inaccessible with natural occurring materials. The dispersion relation of Bloch modes constitutes the quantity on which constraints are imposed. Here, an optimization procedure was applied to achieve either an almost perfect (but to date no sub-wavelength) imaging or diffractionless propagation of sub-wavelength structures through a MM. Independent from the chosen examples, also different target functions might be easily chosen. Technologically, the demonstrated design approach of super-cell stacked MMs appears to be straightforwardly realizable with standard planar technologies (e.g. e-beam lithography) already at hand. Allowing the variation of film thicknesses is a minor technological challenge. Since the approach intrinsically relies on an optimization, a larger number of free parameters in the design (degrees of freedom) would increase the quality of the achieved MM's characteristics as compared to the desired ones. The fact that constraints were only imposed on the two-dimensional iso-frequency curve in the current work are mainly caused by the large demand on computational resources; but in principle they can be even imposed on the full spatio-temporal dispersion relation $k_z(k_x, k_y, \omega)$ which is relevant for pulsed beam propagation.

4.5 Reflection and transmission at a planar interface

In the two previous sections the focus was on light propagation within bulk MMs. The dispersion relation of the FM was shown to correctly predict physical observations, i.e. the refraction and diffraction characteristics of beams. However, only little attention was paid to the precise treatment of MM boundaries. But, if one aims at describing light propagation at finite samples more correctly, then it is additionally important to consider the scattering (reflection and transmission) properties of MMs, too. In contrast to light propagation through the bulk, where the FM will always become dominant after a reasonably long distance, the treatment of light coupling at the MMs' boundaries appears to be more involved. Thus, detrimental for a description of finite structures, e.g. a slab or stratified MMs, is the possible excitation of a larger number of Bloch modes at the interfaces in general. Then, the coupling of light into the MM is a complicated issue and requires a rigorous treatment. However, remembering the classification of a homogeneous medium as it was outlined in the beginning of this chapter, then it would be highly desirable to likewise have a similar situation, namely to extract the coupling properties at the MM interfaces from that Bloch mode that dominates the light propagation in the bulk, i.e. the FM. The theoretical principles for both treatments, i.e. a fully rigorous as well as an approximative solution (fundamental mode approximation), were already given in Sec. 3.2.

They are applied now to specific examples and the physical implications will be discussed.

4.5.1 Interface between a homogeneous dielectric and a metamaterial

In the following we will specify this model, at first, to the rather special, but highly relevant, case of the single interface between vacuum and a MM. In this context it will be shown that the FMA is completely equivalent to the introduction of an effective impedance, namely the Bloch impedance Z_B which is the second effective wave parameter in addition to the propagation constant k_z . Exemplarily, a Swiss cross MM is analyzed subsequently. The limits of the FMA are explored and implications are discussed. Finally, we will go beyond this scenario in discussing an example which requires the most general case, i.e. when reflection and transmission are governed by multiple modes.

4.5.1.1 The Bloch impedance

Let us first start with a description of the fundamental quantities of the system under consideration, i.e. a planar interface between a homogeneous dielectric and a MM. To this end, Fig. 3.1 shows a schematic of the situation. In the present case, the eigenmodes of medium \mathcal{L} become just plane waves $|P_n\rangle$. To keep the description as simple as possible, but without loss of generality, we will restrict the following discussion to y -polarized incident plane waves impinging from air in the x - z -plane and having a lateral wave-vector $\mathbf{k}_\perp = (k_x, 0)^T$. Thus,

$$|P_{n+}\rangle = |P_{n-}^\dagger\rangle = (0, E_n^P, H_n^P, 0)^T \quad (4.4)$$

$$|P_{n-}\rangle = |P_{n+}^\dagger\rangle = (0, E_n^P, -H_n^P, 0)^T \quad (4.5)$$

with $H_n^P = E_n^P/Z_{P,n}$ and

$$Z_{P,n} = \frac{\sqrt{\mu_0/\epsilon_0}}{\sqrt{1 - k_x^2/k_0^2 + \frac{\lambda}{\Lambda_x}n}} \quad (4.6)$$

being the *lateral impedance* of plane wave mode n . Λ_x denotes the period in x -direction and $k_0 = \omega/c$ is the vacuum wavenumber. Furthermore, assuming that the MM is mirror-symmetric with respect to both x - and y -direction and that it is terminated such that the unit cell is mirror-symmetric with respect to the z -direction, similar relations [162] hold for the eigenmodes of the periodic MM (medium \mathcal{R}), i.e.

$$|R_{n+}\rangle = |R_{n-}^\dagger\rangle = (E_{n,x}^B, E_{n,y}^B, H_{n,x}^B, H_{n,y}^B)^T \quad (4.7)$$

$$|R_{n-}\rangle = |R_{n+}^\dagger\rangle = (E_{n,x}^B, E_{n,y}^B, -H_{n,x}^B, -H_{n,y}^B)^T. \quad (4.8)$$

Now, Eqs. (4.4)-(4.8) with $n = 0$ are plugged into Eqn. (3.29) which determines the approximate solution for the reflection coefficient r_0 into the fundamental plane wave. In the following, the subscript "n = 0" will be omitted from all field components, i.e. $E_0^P \rightarrow E^P$ and $E_{0,x}^B \rightarrow E_x^B$ and $Z_{P,0} \rightarrow Z_P$, keeping in mind that everything is mapped onto the forward propagating FMs of both media $|P_{0+}\rangle$ and $|R_{0+}\rangle$, respectively. Now, explicitly evaluating the numerator of r_0 according to Eqn. (3.29), we get without any further approximation ($\|\cdot\| = C^{-1} \iint dx dy$ denotes the cross section average with C being the cross section area)

$$\begin{aligned} \langle R_{0-}^\dagger | L_{0+} \rangle &= \iint dx dy [\mathbf{E}^P \times \mathbf{H}^B - \mathbf{E}^B \times \mathbf{H}^P]_z \\ &= \iint dx dy [E_y^B H^P - E^P H_x^B] \\ &= C(H^P \|E_y^B\| - E^P \|H_x^B\|) \\ &\equiv C(Z_P^{-1} - Z_B^{-1})E^P \|E_y^B\|, \end{aligned}$$

where we have introduced the *tangential Bloch impedance* [163, 164] of the MM

$$Z_B = \frac{\|E_y^B\|}{\|H_x^B\|} \quad (4.9)$$

as the ratio between the averaged lateral (tangential) electric and magnetic field components. Applying the analogue procedure also to the denominator of Eqn. (3.29) we get

$$\langle R_{0-}^\dagger | L_{0-} \rangle = -C (Z_P^{-1} + Z_B^{-1}) E^P \|E_y^B\|.$$

A very similar analysis can be performed for the transmission coefficient t_0 into the FM of the MM, too. Finally this leads to the following expressions for the reflection and transmission coefficients:

$$r_0 = \frac{Z_B - Z_P}{Z_B + Z_P}, \quad (4.10)$$

$$t_0 = \frac{2Z_B}{(Z_B + Z_P)} \frac{E^P}{\|E_y^B\|}. \quad (4.11)$$

Most strikingly, Eqs. (4.10)-(4.11) are formally identical to the reflection/transmission coefficients at an interface between two genuine homogeneous media unless one uses the Bloch impedance as defined above to characterize the medium \mathcal{R} on the right.

Let us briefly summarize the recent findings. It turned out that the calculation of the FMs transmission and reflection coefficients t_0 and r_0 according to Eqs. (4.10)-(4.11) is fully equivalent to the usage of Eqs. (3.29)-(3.30) which is nothing else than the FMA in

context of a Bloch modal description. It has to be mentioned that the derived coincidence between these two descriptions is not self-evident^{††}. On the one hand it is methodologically interesting, since it brings together two different perspectives to look at MMs – a periodic medium perspective (generally dealing with multiple Bloch modes) and a homogeneous medium perspective (dealing with effective properties, in particular impedances). On the other hand, and this is even more important, it opens up the opportunity to evaluate the condition which is a prerequisite for homogenization. In other words, the validity of the FMA in comparison with the rigorous solution according to Eqs. (3.23)-(3.24) can be used to either justify or reject the assignment of effective wave parameters and, in particular, an impedance. This problem is subject of the following paragraph and it will be dealt with by means of a specific example.

Finally, a subtle fact has to be discussed. In the current discussion we have assumed the referential medium \mathcal{L} to be a homogenous isotropic dielectric and, without having examined it in more detail, the introduction of a Bloch impedance (and hence the consistency between Eqs. (3.29)-(3.30) and Eqs. (4.10)-(4.11)) is specific to this situation. Assuming, in contrast to that, the referential medium to be rather another nano-structured medium with an eigenmode spectrum which is similar to the considered MM, then the FMA may be applicable as well (for an example see [TP02]). However, this does not imply to treat the materials as homogenous in a standard sense, although the FMA is valid. It simply renders Eqs. (3.29)-(3.30) to be more general expressions that are detached from the question of homogenization.

4.5.1.2 Case study: The Swiss cross metamaterial

In the following, a particular example will be considered. A Swiss cross MM is analyzed in detail. Especially, it will be shown how the FMA (being prerequisite for homogenization) can be met while simultaneously maintaining the dispersive features of interest, i.e. a left-handed behavior. To this end, we will consider the interface between air and a Swiss cross MM in a frequency domain where the propagation constant is negative (left-handed behavior). The layout of the structure was already depicted in Fig. 4.1. The current Swiss cross MM consists of a MgO layer ($n = 1.73$, thickness: 54 nm) sandwiched between two layers of

^{††}Indeed, the rigorous solution of the boundary-value problem according to Eqn. (3.22) can be written in several equivalent forms. When truncated to the contribution of the FM, however, these equivalent formulas give rise to different approximate expressions for r_0 and t_0 . One alternative formula for these coefficients was derived in Ref. [TP02]. Hence, the usage of the Bloch impedance according to Eqs. (4.10)-(4.11) is only one particular choice to integrate the properties of the FM into the calculation of the reflection and transmission coefficients.

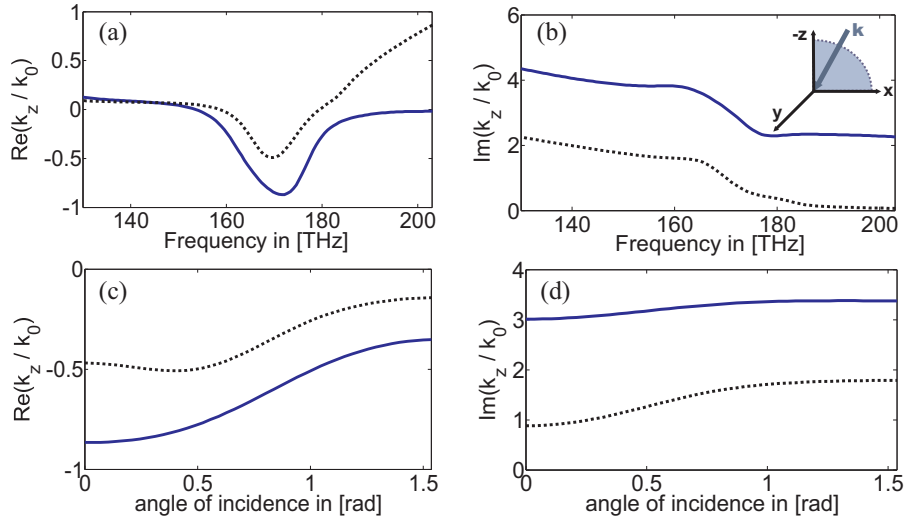


Figure 4.15: Real (a) and imaginary (b) part of the propagation constant $k_z(\omega)$ of the FM with $\mathbf{k}_\perp = (0, 0)^T$ propagating in positive z -direction. Real (c) and imaginary (d) part of $k_z(k_x)$ of the FM for a fixed frequency of 170 THz. The blue solid and black dotted curves correspond to a period in z -direction of $\Lambda_z = 230$ nm and $\Lambda_z = 600$ nm, respectively. For the sake of clarity, the inset shows the orientation of the incident field.

gold (thickness: 44 nm, permittivity according to [M.2]). The remaining parameters are: $W_1 = 310$ nm, $W_2 = 90$ nm and the lateral period is 600×600 nm². The entire nanostructure is embedded in a host material with refractive index of $n = 1.4$. The structure is periodic in all spatial dimensions and the period in z -direction, i.e. Λ_z , will be subject to variations. It will be chosen sufficiently large such that pronounced nearest-neighbor interactions are suppressed. Variation of Λ_z only changes the thickness of the host material layer. The thickness of the Au – MgO – Au stack is fixed. Hence, the filling fraction of the Swiss cross element with respect to the z -direction can be controlled. In the following we assume the Swiss cross to be terminated symmetrically right in the middle of the host material layer. Before going into the detailed analysis of the coupling problem, we first examine the dispersion relation of the FM of the Swiss cross structure. Figs. 4.15a - 4.15b shows the real and imaginary part of $k_z(\omega)$ for propagation along z , i.e. $\mathbf{k}_\perp = 0$. The period Λ_z will be either 230 nm (blue solid lines) or 600 nm (black dotted lines) in the following discussion; corresponding to a high or low filling fraction. Any period in-between could have been equally chosen. The corresponding dispersion relations continuously settle in-between the two representatively chosen periods. In both cases there is a narrow frequency region (around the resonance position of 170 THz) where the real part of the propagation constant k_z becomes negative. As expected, the resonance strength becomes weaker for $\Lambda_z = 600$ nm, but also the attenuation [$\propto \Im(k_z)$] is decreased. For the sake of completeness, Figs. 4.15c - 4.15d also provide the angular dispersion for a fixed frequency of 170 THz. The

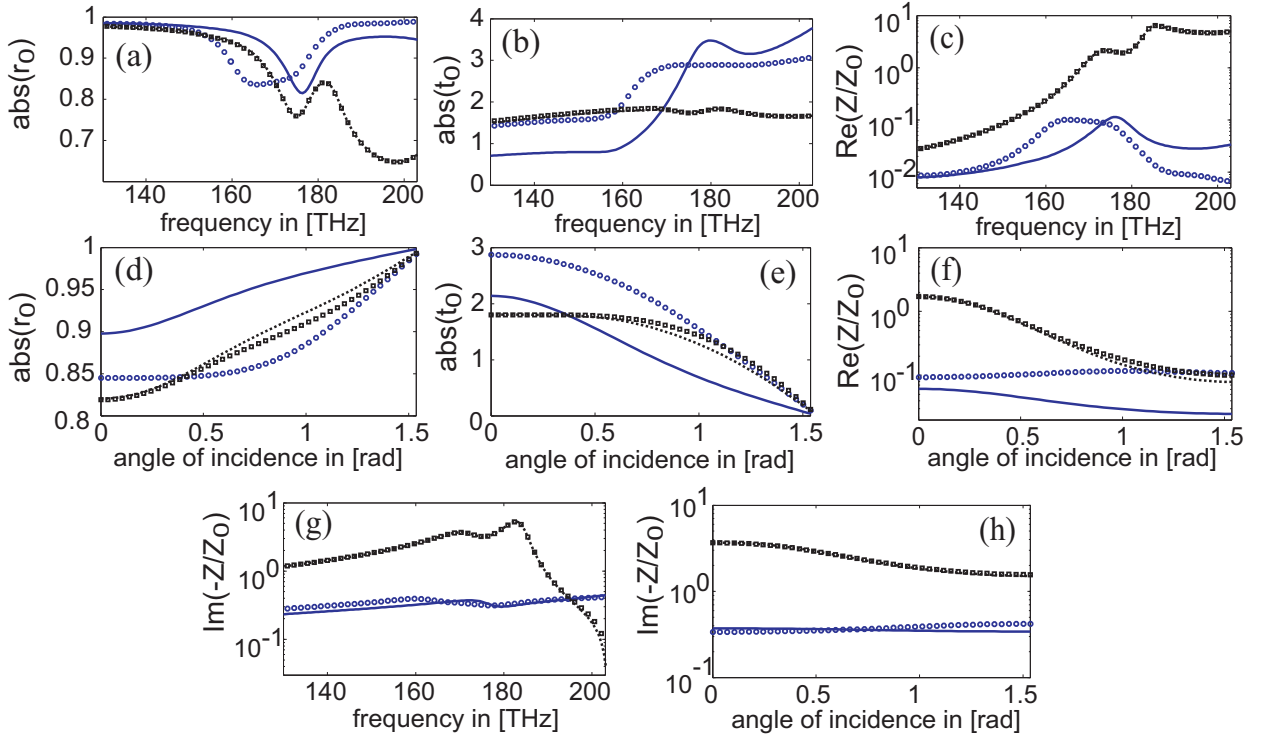


Figure 4.16: Modulus of the reflection (a) and transmission coefficient (b) into the FMs $|L_{0-}\rangle$ and $|R_{0+}\rangle$ as well as real (c) and imaginary part (g) of the tangential Bloch impedance associated with $|R_{0+}\rangle$ for normal incidence as a function of frequency. Modulus of the reflection (d) and transmission coefficient (e) into the FMs $|L_{0-}\rangle$ and $|R_{0+}\rangle$ as well as real (f) and imaginary part (h) of the tangential Bloch impedance associated with $|R_{0+}\rangle$ as a function of the angle of incidence at a fixed frequency of 170 THz. The results have been obtained by using the approximate formulae according to Eqs. (3.29)-(3.30). The longitudinal period of the Swiss cross unit cell amounts to $\Lambda_{z,1} = 230$ nm (blue circles) and $\Lambda_{z,2} = 600$ nm (black squares). For comparison the results of rigorous calculations are shown by blue solid ($\Lambda_{z,1}$) and black dotted lines ($\Lambda_{z,2}$).

maximum angle of $\alpha = \pi/2$ corresponds to grazing incidence of the illuminating plane wave and hence this value corresponds to $k_x = 3.56 \mu\text{m}^{-1}$ for the lateral Bloch vector component. Obviously, $\Re(k_z)$ remains negative throughout the whole angular range.

Now, we proceed with the coupling problem, where Fig. 4.16 provides the necessary information. First we concentrate on r_0 and t_0 . The blue circles (black squares) show $|r_0|$ and $|t_0|$ according to Eqs. (3.29)-(3.30) for periods Λ_z equal to 230 nm (600 nm). Moreover, Fig. 4.16 also displays results of rigorous calculations for r_0 and t_0 for comparison (blue solid and black dotted lines). For both, normal and oblique incidence, the consistence between the rigorous and approximative solutions is clearly better for $\Lambda_z = 600$ nm. Although not shown explicitly, the same observations hold for the phases of r_0 and t_0 . The strongest deviations appear for $\arg(t_0)$ around 170 THz and $\Lambda_z = 230$ nm amounting to about 0.6 rad. For the sake of completeness, we also provide the normalized tangential Bloch impedances Z_B/Z_0

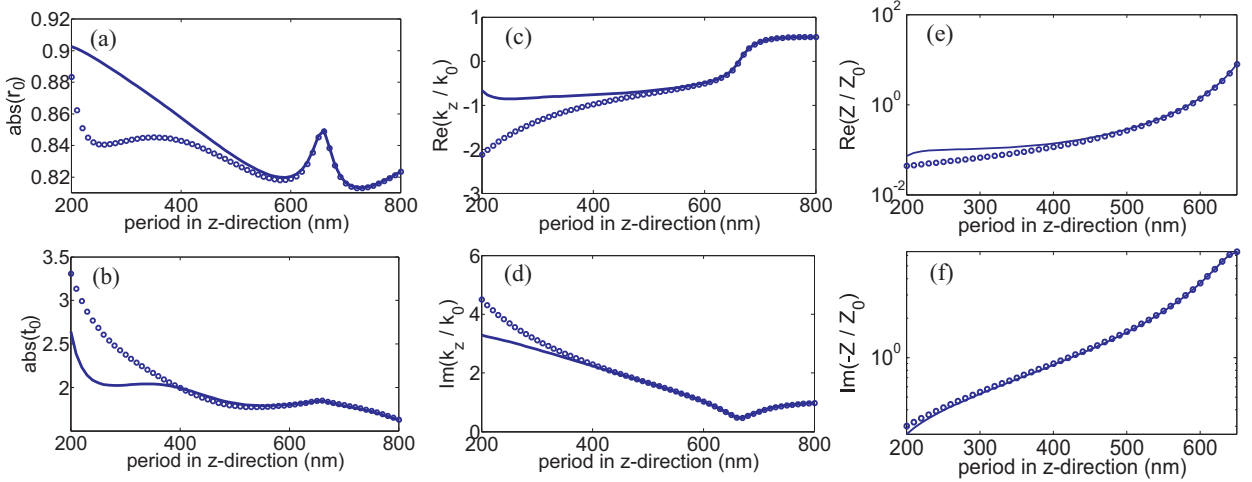


Figure 4.17: Modulus of the reflection (a) and transmission coefficient (b) into the FMs $|L_{0-}\rangle$ and $|R_{0+}\rangle$ for normal incidence at 170 THz as a function of the longitudinal period. The circles represent the approximate solutions according to Eqs. (3.29)-(3.30) and the solid lines are rigorous results. k_z (c,d) and impedance (e,f) as a function of the longitudinal period. The solid lines are the propagation constants and the Bloch impedance of the FM and the circles are the outcome of a parameter retrieval procedure applied to the single layer Swiss cross structure.

(with $Z_0 = \sqrt{\mu_0/\epsilon_0}$) for all considered scenarios. Here, the impedance of the Swiss cross half-space $Z/Z_0 = (1 + r_0)/(1 - r_0)$ as it is retrieved from rigorous reflection data [TP01] is also shown for comparison (solid lines). The logarithmic scale improves the visibility. As before it can be clearly recognized that a smaller filling fraction (longitudinal period of 600 nm) leads to a reasonable agreement.

Systematic investigation of the Λ_z -dependence. To further verify this statement, we have additionally calculated r_0 and t_0 for normal incidence at 170 THz as a function of the longitudinal period Λ_z . Figs. 4.17a - 4.17b clearly evidence the suggested tendency that the accuracy of Eqs. (3.29)-(3.30) increases the smaller the filling fraction is. The dependence of the scattering data on the longitudinal period Λ_z suggests that for small periods, i.e. $\Lambda_z \lesssim 500$ nm, higher-order Bloch modes are considerably excited. For small distances between the interface and the Swiss cross nano-structure, the optical near field becomes more complicated where also the lateral field distribution of the FM is affected [165]. Hence, the mode mismatch between the exciting plane wave and the FM increases (see Fig. 4.18a for the field distribution) such that higher-order modes in both media get noticeably excited. On the contrary, if the filling fraction is sufficiently small such that the interface is beyond the near-field range of the sub-wavelength nano-structure, the lateral field distribution of the FM converges towards a plane wave (see Fig. 4.18b).

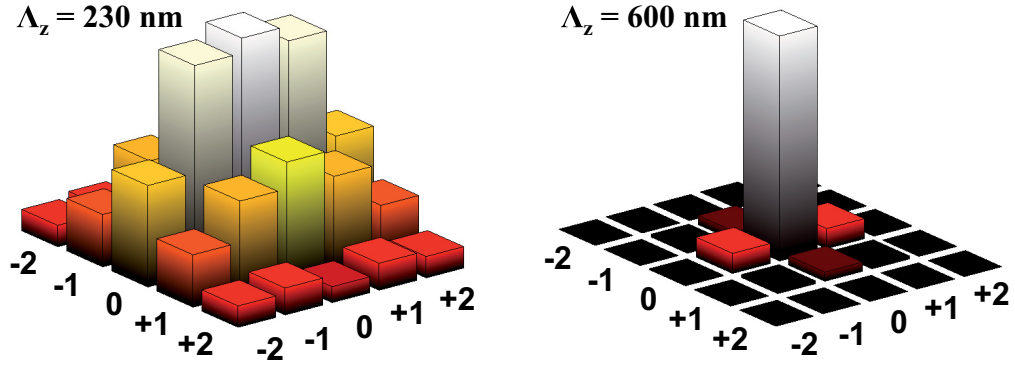


Figure 4.18: Comparison of the lateral field amplitude distribution of the FM of the Swiss cross structure in terms of its Fourier harmonics (denoted by the integer numbers). Both representations are normalized to the zeroth-order Fourier harmonic. The frequency is set to 170 THz.

Impact on the parameter retrieval procedure. Finally, it appears to be worthwhile to compare two different approaches to assign effective wave parameters to a MM. To this end, the Bloch modal approach is compared with the parameter retrieval procedure [TP05, 124]. The retrieval procedure applied to a single layer of the current Swiss cross structure determines an effective propagation constant $k_{z,\text{retr}}$ and an effective impedance Z_{retr} . Inherently, the parameter retrieval procedure assumes reflection and transmission at the interfaces as well as propagation through the slab to be exclusively determined by the FM^{‡‡} of both media. Of course, the pure application of the method itself does not require these assumptions to be fulfilled.

In case of the here considered Swiss cross MM, the pure bulk propagation through the thin MM slab was verified to be fully determined by the FM of the Swiss cross structure across the entire parameter range $200 \text{ nm} \leq \Lambda_z \leq 800 \text{ nm}$. This is consistent with the assumptions of the retrieval procedure. Hence, it remains to investigate the influence of multiple mode coupling, that is when the FMA according to Eqs. (3.29)-(3.30) is not justified, to the retrieved effective parameters. For that purpose, both retrieved parameters are compared with the propagation constant k_z and the impedance Z_B of the FM in Fig. 4.17. The results of both approaches converge to each other for $\Lambda_z \gtrsim 500 \text{ nm}$. This value perfectly matches to the FMA's limit of validity as it was discussed before. On the contrary, both retrieved parameters $k_{z,\text{retr}}$ and Z_{retr} start to deviate from the Bloch modal data for $\Lambda_z \lesssim 500 \text{ nm}$. Then, they cannot be linked to any modal property anymore. Note that even $k_{z,\text{retr}}$ becomes different from k_z . Importantly, these inaccuracies are only caused by the incorrect treatment of the boundary conditions within the parameter retrieval procedure which does not account

^{‡‡}In context of the parameter retrieval procedure the FMs are usually treated as (effective) plane waves.

for multiple mode coupling. Thus, the rather complicated mathematical interrelation of the effective parameters in the retrieval procedure leads to deviations of both of them, although one might have suggested that only the effective impedance is affected. A relevant scenario where this effect can be exemplarily observed is a weakly (or non-) absorbing slab of a specific MM. There, artificial features (resonances and anti-resonances) can be observed in the effective (material) parameters [166] whenever the overall reflection of the slab exhibits a zero (Fabry-Perot minimum). These artificial features can be attributed to a non-vanishing contribution of higher-order Bloch modes for the reflection and transmission process at the slab's boundaries.

However, a detailed analysis of the peculiarities of the parameter retrieval method is not a subject of this thesis, but a short summary is given here for convenience. Restricting the discussion to lossy systems, it can be shown that both parameters, $k_{z,\text{retr}}$ and Z_{retr} , are always converging with an increasing slab thickness (number of functional layers) although the FMA might not be justified. Then, the effective propagation constant converges to the propagation constant of the FM [TP06, 141], i.e. $k_{r,\text{retr}} \rightarrow k_z$. The effective impedance Z_{retr} converges to the impedance of the half-space [TP01, 141], however, it cannot be related to a single Bloch mode.

4.5.2 Interface between two dissimilar metamaterials

Going beyond the limitations of the FMA, the Bloch modal formalism in its most general form can also be used to describe the coupling of light between MMs in a regime where the MMs cannot be considered to be homogenous. A simplification, however, can always be introduced by considering only a few Bloch modes to be involved in the process. This will be demonstrated in the following section. In Sec. 3.2 the procedure to deal with the most general case of coupling between two MMs has already been outlined. Thus, in the current section we want to demonstrate the power and versatility of this approach. For that purpose one has to remember that Eqs. (3.23)-(3.24) provide the rigorously calculated reflection and transmission coefficients in terms of the profiles of all Bloch modes supported by media \mathcal{L} and \mathcal{R} . Again concentrating on the reflection and transmission coefficients into the FMs, it is expected that these coefficients are well defined by a finite number of Bloch modes only (see discussion in Sec. 3.2). The precise number will depend, of course, on the mode-mismatch between both media. A moderate mismatch between the modal basis of both media at the interface will result in a quite small number and vice versa.

Now, to continue with the specification of the particular setup, the interface between a bulk Swiss cross MM and a bulk fishnet MM serves as an example. The fishnet structure is sketched in the inset of Fig. 4.19 and the corresponding parameters are given in the figure's

caption. The Swiss cross structure is identical to that used in the previous section and the

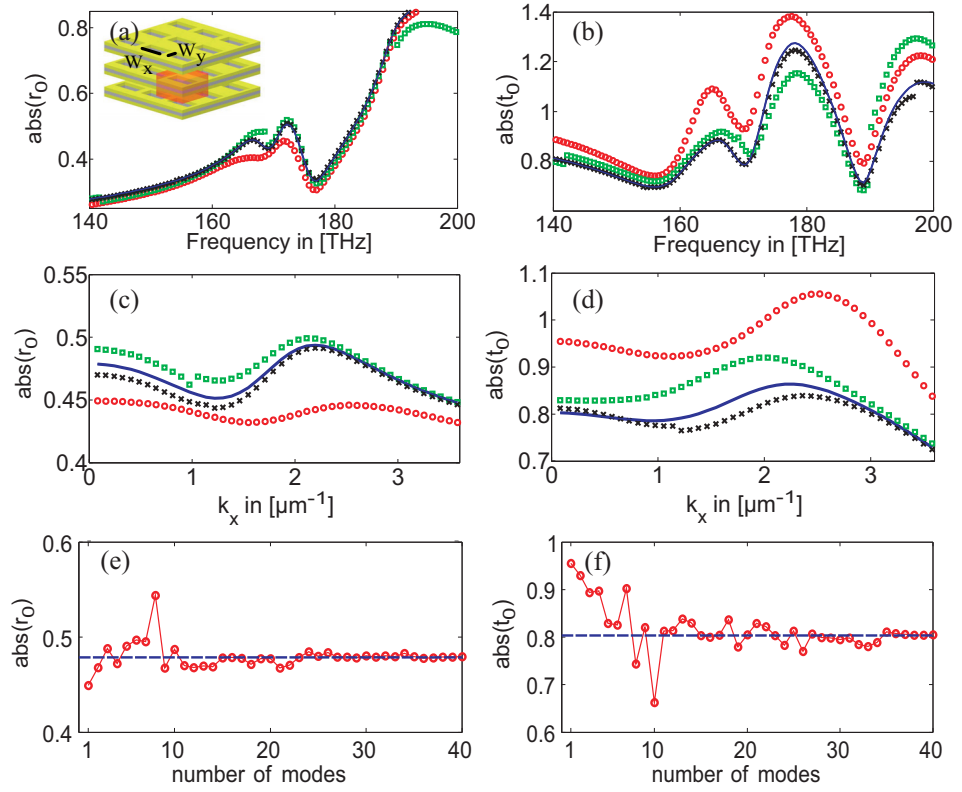


Figure 4.19: Reflection and transmission at a planar interface between a Swiss cross and a fishnet MM. Modulus of r_0 (a) and t_0 (b) for normal incidence as a function of frequency as well as the modulus of r_0 (c) and t_0 (d) at a frequency of 170 THz as a function of the lateral Bloch vector component k_x of the incident mode. The blue, solid lines are the rigorous results. The symbols represent approximate solutions taking into account a different number of modes; circles - 1 (1), squares - 5 (9), crosses - 15 (21). The numbers in brackets are those for oblique incidence. The fishnet's functional element consists of an Ag – MgO – Ag stack completely embedded in a host material ($n = 1.4$). The geometrical parameters are as follows – thickness of the thick (thin) wire: $W_y = 255$ nm ($W_x = 445$ nm); permittivity of Ag: see Mat. [M.1]; refractive index of MgO: 1.73; thickness of Ag (MgO) layer: 48 nm (42 nm); lateral period: 600×600 nm²; z -period $\Lambda_z = 200$ nm. Finally, the dependence of the reflection (e) and transmission (f) coefficient with respect to the number of Bloch modes considered for their calculation is displayed. The frequency amounts to 170 THz and $\mathbf{k}_\perp = (0, 0)$. The red, solid lines are only guides to the eyes and the blue dashed lines are the associated rigorous values taking all modes into account.

longitudinal period was set to $\Lambda_z = 230$ nm. Again the frequency is chosen to be in the left-handed domain of the Swiss cross MM which is operated at the resonance frequency of 170 THz. The fishnet's design is chosen such that a similar resonance occurs at the same frequency. Thus, we study here the light scattering between two left-handed media.

The relevant results, i.e. $|r_0|$ and $|t_0|$, are displayed in Fig. 4.19 for both situations; normal incidence as a function of the frequency (see Figs. 4.19a and 4.19b) and at a fre-

quency of 170 THz as a function of the lateral Bloch vector component $\mathbf{k}_\perp = (k_x, 0)^T$ (see Figs. 4.19c and 4.19d). It has to be mentioned, that r_0 and t_0 represent the data of the FMs only, but the number of modes which are used to calculate them [according to Eqs. (3.23)-(3.28)] will be subject to variations in the following discussion. For that reason, let us shortly remember the underlying procedure how to calculate r_0 and t_0 in different levels of approximation. Thus, it must be first mentioned, that the rigorous solution according to the matrix equations (3.23) and (3.24) provides a vector (with N elements) of all transmission and reflection coefficients into all eigenmodes taken into account during the numerical realization. However, we are interested in the first entries only, that is r_0 and t_0 . Consequentially, one may calculate a reduced set of transmission and reflection coefficients by just shrinking the size of matrices \hat{a} , \hat{c} , \hat{d} and \hat{f} (see Sec. 3.2) to an arbitrary size $\tilde{N} \times \tilde{N}$ ($\tilde{N} < N$) which is nothing else than neglecting a certain number of modes for the specification of the reflection and transmission process. By that procedure, one can clearly and systematically identify the importance of each mode with respect to light coupling at the interface. In that picture, the FMA corresponds to a matrix size reduction down to 1×1 (scalar quantities), i.e. all higher-order Bloch modes are neglected.

Now, concentrating on the results displayed in Fig. 4.19, it can be recognized that the FMA (red circles) only qualitatively reproduces the main features of the reflection and transmission spectra, but the very data may differ from each other by up to 25%. By taking into account an increasing number of Bloch modes to built up the matrices according to Eqs. (3.25)-(3.28), it can be observed that the results are converging across the entire spectral region against the rigorous results (blue solid lines). For that purpose, Figs. 4.19a - 4.19d show a selection of different reflection and transmission spectra (colored symbols). For normal incidence, the spectra are associated with a total number of considered Bloch modes amounting to 1 (red circles), 5 (green squares) and 15 (black crosses). For oblique incidence the symmetry with respect to the x -direction is broken resulting in a larger number of modes in both media participating in the coupling process. For that reason, a comparable convergence requires a larger number of modes as compared to the normal incident case. At first glance, these numbers seem to be quite large. However, using a plane wave basis [90] rather than the Bloch mode approach, typically hundreds of plane waves would be required to get the same accuracy.

Finally, it has to be admitted that the accuracy of the solution does not increase strictly monotonically with the number of Bloch modes taken into account. This might be attributed to the particular arrangement of the Bloch modes one has chosen, because there is no *a priori* information about the importance of a particular mode with respect to coupling. For the presented results, the Bloch modes were sorted with respect to the modulus of the imaginary

part of the associated propagation constant. For that purpose, Figs. 4.19e and 4.19f show the detailed convergence behavior of r_0 and t_0 for a chosen set of parameters, i.e. $\mathbf{k}_\perp = (0, 0)$ and a frequency of 170 THz. In particular, the transmission coefficient shows some sparks but, nevertheless, the overall convergence is always ensured.

4.6 Chapter summary and concluding remarks

The first part of this chapter was dedicated to the peculiar characteristics of light beams propagating through a bulk MM. In particular, it was shown that the dispersion relation of the fundamental Bloch mode, i.e. the mode which prevails against all other modes in terms of attenuation, can be exploited to describe diffraction and refraction of beams accurately. Consequentially, all physical observations are solely linked to wave properties of the underlying eigenmodes of the structure without making any assumptions to the constitutive relations of the *effective* medium. Exemplarily, a fishnet MM was thoroughly analyzed. Its dispersion relation was shown to be highly non-trivial. This denies the description of the considered MM on grounds of local, effective material parameters. Exemplarily, it was shown that the refractive and diffractive properties can alter dramatically. Only slight variations in the operating wavelength turned the refraction characteristics of the fishnet from initially being negative to become positive although the phase velocity remained negative (left-handed behavior) in all considered cases.

Based on the results and experiences that were obtained for the fishnet MM, a new design approach was presented and discussed in the second part of this chapter. It focused on the systematic modification and tailoring of the MM's dispersion relation. Here, a super-cell fishnet MM was suggested. In that context, two adapted fishnet structures were successfully designed. The first one exhibits a circular angular dispersion relation mimicking the properties of an isotropic, homogeneous left-handed material. The second fishnet was adapted to support the formation of self-collimated beams rendering the structure amenable to a light tunneling scheme. Especially for these complex MM structures, only the dispersion relation of the fundamental Bloch mode was shown to be the sole and pivotal quantity.

Up to this point, all considerations were performed only by relying on the dispersion relation of modes, but the concrete modal field distribution must not be taken into account. This situation changes, when one gets interested in the quantitative determination of the reflection and transmission coefficients at MM boundaries. To this end, the last part of this chapter was devoted to the single interface between, at first, a homogeneous dielectric and a MM and, secondly, that of two dissimilar MMs. Emphasis was put on the first case because it is of high practical relevance. On the example of a Swiss cross MM it was elaborated that

the introduction of effective wave parameters, especially a modal and scalar impedance, is only justified when the mutual cross-coupling between different Bloch modes at the MM's interface can be reliably neglected. Only in that case, the coupling into the fundamental Bloch mode is exclusively determined by itself and we speak about the fundamental mode approximation (FMA). In this context, techniques were discussed and presented that allow to evaluate exactly this criterium. In case of the considered Swiss cross MM, it was shown that the increase of the longitudinal period, while simultaneously maintaining the layout of the functional element (meta-atom), allowed to suppress the mutual cross coupling of modes. Only in this limit, effective wave properties as retrieved from an inversion of the reflection and transmission coefficients perfectly agree with the Bloch mode properties. Most notably, the well-established parameter retrieval method was shown to provide the wave parameters of the fundamental Bloch mode only under the condition that the FMA is justified. In all other cases the retrieved parameters may assume arbitrary values that do not reflect a modal property anymore. Eventually, the most general formalism which is able to account for mutual cross coupling between multiple modes was applied to the problem of reflection/transmission between to dissimilar MMs.

5 Higher harmonic generation by plasmonic nanostructures

Most likely, the first investigations for the potential of MMs with respect to nonlinear wave propagation in the optical domain started with second-order nonlinear wave interactions in generic left-handed materials. Here it has to be mentioned, that no potentially new and unprecedented nonlinear properties of MMs were at the focus of research, but it was rather the effect of a (linear) left-handed behavior and its influence on three-wave mixing processes, i.e. parametric amplification and second-harmonic generation (SHG) [17–19, 167]. In particular, SHG (in the stationary as well as pulsed regime) as the most fundamental second-order nonlinear process attracted a considerable share of interest, because (semi-)analytical descriptions are accessible there [17, 34, 168–170]. By that, new and interesting features, like backward SHG [17] and phase-locked SHG [168, 169] were revealed.

At the same time, a second branch in research was engaging realistic, metallic nanostructures. Here, the excitation of surface plasmon-polaritons, which goes along with a considerable confinement/enhancement of the electromagnetic field in the nano-structure's vicinity, promises to enhance the conversion efficiencies of nonlinear light-matter interactions [TP11, TP12, 171–178]. In that sense, one can say that the focus of interest for that branch of research lies in the study of efficient 'nonlinear materials' being composed of metallo-dielectric nanostructures. It has to be mentioned that this topic has a long standing history already well before the proposal of MMs (see e.g. Refs. [179–181]). However, the possibilities to produce large scale samples of metallic nanostructures in a deterministic fashion arose side by side with the implementation of MMs.

The combination of metallic nanostructures, which sustain the excitation of plasmon polaritons, and nonlinear dielectric materials is an appealing approach to significantly enhance the conversion efficiency in nano-optical devices [174, 175]. In particular, the integration of nonlinear dielectrics into a plasmonic system may be especially useful to solve one of the most pertinent problems in current nano-optics being the dominance of dissipation in the metallic components. Optical parametric amplification may be at least one possible route to compensate at least partially for these losses.

Previously, several methods were developed to simulate the nonlinear interaction of light with nano-structures. Besides some very general methods as FDTD or FEM, there are specialized methods for a large variety of different geometries, e.g. circular shapes [182], one-dimensional layered systems [183, 184] and radially symmetric nano-structures acting as scatterers on top of surfaces [185]. However, it is the aim of this work to deal with periodic nano-structures. Therefore, one can find suitable derivatives of classical methods based on the differential or integral formalism [186–188]. Most notably, also the Fourier modal method (FMM) was applied for this purpose, in particular to analyze SHG. It was continuously developed further, starting from two-dimensional structures [189], going over three-dimensional, single-layer structures [190] and finally towards higher-harmonic generation at three-dimensional, multi-layer structures [TP13].

The Fourier modal approach presented in the following will summarize the material already published in Ref. [TP13]. Hence, in what follows the focus will be on metal-dielectric systems where the nonlinear polarization can be represented by a power series expansion with respect to the electrical field. Such a description is typical for the dipolar contributions of bound electrons of a bulk material. Nevertheless, the formulation may be also extended towards other kinds of nonlinearities where the response stems from the conduction electrons of the metallic components [TP11]. Furthermore, the method relies on the undepleted pump approximation (UPA) [191] that ignores the feedback of the nonlinearly induced field on the pump field. In most practical cases this approximation holds, since the intensity of the nonlinearly induced field is much less than the pump field intensity. Therefore, the presented method may be immediately applied to higher harmonics generation processes as, e.g., SHG and third-harmonic generation (THG).

The chapter is divided into three sections. As already mentioned, the first section is devoted to the concise description of the extended FMM. In two further sections, this outlined computational scheme will be used to investigate the nonlinear optical response from two different setups. The first one is a metallic nano-wire structure where localized plasmon-polariton resonances are excited and the influences on SHG will be analyzed. The second one is a coupled metallic-dielectric system where peculiar characteristics in the generated third-harmonic signal will be investigated.

5.1 Statement of the problem

The fundamental geometry equals that of the linear problem and it was already introduced in Sec. 2.1.2. A schematic is shown in Fig. 2.1. The domain of the incident field (region $i = -1$, i.e. the cladding) and the transmitted field (region $i = L$, i.e. the substrate)

are assumed to be semi-infinitely extended half-spaces being composed of a homogeneous, isotropic and *linear* material. The multi-layer structure ($i = 0, 1, \dots, L - 1$) may contain isotropic, but now also nonlinear materials. All individual layers share a common periodicity $\Lambda_x \times \Lambda_y$ in the lateral dimensions but exhibit translational invariance along the propagation direction z .

The rigorous electromagnetic treatment of that problem is again derived from Maxwell's equations according to Eqs. (2.1). Once again, the constituent materials are assumed to be non-magnetic. However, they are allowed to possess nonlinear optical properties as well. For that reason, the dielectric displacement now reads as

$$\mathbf{D}(\mathbf{r}, \omega) = \epsilon_0 \epsilon(\mathbf{r}, \omega) \mathbf{E}(\mathbf{r}, \omega) + \mathbf{P}^{\text{NL}}(\mathbf{r}, \omega), \quad (5.1)$$

with $\mathbf{P}^{\text{NL}}(\mathbf{r}, \omega)$ being the nonlinear polarization. So, all linear dispersive properties of the medium are still described by the permittivity, whereas the nonlinear ones are collected within $\mathbf{P}^{\text{NL}}(\mathbf{r}, \omega)$.

The nonlinear polarization. In the following it is assumed that the nonlinear polarization can be represented by a power series expansion with respect to the electrical field. The nonlinear optical properties of all constituent materials are then solely characterized by nonlinear susceptibility tensors of different orders depending on the frequencies of the interacting fields. Consequentially, the nonlinear polarization in frequency domain is generally represented by [191]

$$\begin{aligned} \mathbf{P}^{\text{NL}}(\omega) = & \epsilon_0 \int_{-\infty}^{\infty} d\omega' \hat{\chi}^{(2)}(-\omega; \omega', \omega - \omega') : \mathbf{E}(\omega') \mathbf{E}(\omega - \omega') + \\ & \epsilon_0 \int_{-\infty}^{\infty} \int_{-\infty}^{\infty} d\omega' d\omega'' \hat{\chi}^{(3)}(-\omega; \omega', \omega'', \omega - \omega' - \omega'') : \mathbf{E}(\omega') \mathbf{E}(\omega'') \mathbf{E}(\omega - \omega' - \omega'') + \dots \end{aligned} \quad (5.2)$$

where the colon operators denote tensorial products. The spatial dependency of all quantities was omitted here, but of course the electrical field, the nonlinear susceptibilities and the nonlinear polarization will depend on \mathbf{r} in general. The superscript attached to the nonlinear susceptibility shows the order of the respective quantity. However, it will be omitted in the following for the sake of clarity, because it is likewise determined by the rank of the associated tensor.

Interaction between two monochromatic fields. In what follows the focus will be on SHG and THG, respectively. It is assumed that the entire electromagnetic field consists of two monochromatic fields, the pump field at frequency $\omega_1 > 0$ and the generated harmonic field at $\omega_2 > 0$, respectively. Hence, it can be written as

$$\begin{aligned}\mathbf{E}(\mathbf{r}, t) &= \sum_{n=1}^2 \mathbf{E}_n(\mathbf{r}) \exp(-i\omega_n t) + c.c., \\ \mathbf{E}(\mathbf{r}, \omega) &= \sum_{n=1}^2 \mathbf{E}_n(\mathbf{r}) \delta(\omega - \omega_n) + \mathbf{E}_n^*(\mathbf{r}) \delta(\omega + \omega_n),\end{aligned}\tag{5.3}$$

where analogue expressions are assumed to hold for \mathbf{D} , \mathbf{H} , \mathbf{B} and, in particular, the nonlinear polarization \mathbf{P}^{NL} , too. The quantities $\mathbf{E}_n(\mathbf{r})$ denote the complex amplitudes of the field at frequency ω_n .

Now, by substituting Eqs. (5.1)-(5.3) into Eqs. (2.1), and again introducing a re-normalized magnetic field $\tilde{\mathbf{H}}_n = \sqrt{\mu_0/\epsilon_0} \mathbf{H}_n$ one obtains ($n = 1, 2$)

$$\begin{aligned}\nabla \times \mathbf{E}_n &= +ik_n \tilde{\mathbf{H}}_n, \\ \nabla \times \tilde{\mathbf{H}}_n &= -ik_n (\epsilon_n \mathbf{E}_n + \epsilon_0^{-1} \mathbf{P}_n^{\text{NL}})\end{aligned}\tag{5.4}$$

and (the asterisk denotes the complex conjugate)

$$\begin{aligned}\nabla \times \mathbf{E}_n^* &= -ik_n \tilde{\mathbf{H}}_n^*, \\ \nabla \times \tilde{\mathbf{H}}_n^* &= +ik_n (\epsilon_n^* \mathbf{E}_n^* + \epsilon_0^{-1} (\mathbf{P}_n^{\text{NL}})^*).\end{aligned}\tag{5.5}$$

$k_n = \omega_n/c$ denotes the vacuum wavenumber at the given frequency. Equations (5.5) are the complex conjugated form of Eqs. (5.4), so their solution is redundant. Equations (5.4) represent a coupled system of partial differential equations. In particular, the nonlinear polarization is responsible for a coupling between fields at different frequencies, i.e. between the fields at indices $n = 1$ and $n = 2$. Eventually, the tilde above the magnetic field will be omitted in the following assuming the exclusive usage of the re-normalized field in all equations below.

Second- and third-harmonic generation. In order to keep the description quite general it is now assumed that the pump field at frequency ω_1 interacts with a medium exhibiting a nonlinear polarization of order $N = 2$ or $N = 3$, respectively. Thus, there are fields generated at frequency $\omega_2 = M\omega_1$ with $M \leq N$. We exclude the effect of self-phase modulation ($M = 1$) and optical rectification ($M = 0$). A representative example is the Kerr effect ($N = 3, M = 1$) when dealing with third-order nonlinear processes where the

pump field itself is phase-modulated. A reasonable approach towards this issue can be found for example in Ref. [192]. Leaving these cases aside, the focus will be on SHG ($N = M = 2$) and THG ($N = M = 3$) that are subject to the present studies.

Undepleted pump approximation. In what follows the physical problems under consideration are assumed to be well described within the low-depletion limit, such that the undepleted pump approximation (UPA) is justified. Hence, $\mathbf{P}_1^{\text{NL}}(\omega_1)$ is neglected and the mutual cross-coupling between different frequencies vanishes. Consequentially, the pump field at frequency ω_1 can be entirely treated on linear grounds. On the contrary, the nonlinear polarization \mathbf{P}_2^{NL} at $\omega_2 = N\omega_1$ cannot be neglected and in component form it may be written as

$$P_{2,i}^{\text{NL}}(N\omega_1) = \epsilon_0 \sum_{j_1, \dots, j_N} \chi^{ij_1 \dots j_N}(-N\omega_1; \omega_1, \dots, \omega_1) \cdot E_{1,j_1} \cdot \dots \cdot E_{1,j_N} \quad (5.6)$$

with $(i, j_1, \dots, j_N = 1, 2, 3)$ running over the Cartesian components. The argument of the susceptibility $\chi^{ij_1 \dots j_N}$ contains N times the frequency ω_1 . Provided that the nonlinear susceptibility tensor χ is known, the only quantities entering Eqn. (5.6) are the electric field components $E_{1,j}$ at fundamental harmonic (FH) frequency ω_1 . Hence, Eqs. (5.4) represent a linear but inhomogeneous system of partial differential equations. Finally, summarizing all the stated aspects the entire problem can be solved in three steps:

- ▶ Calculate the pump field with the standard FMM for the linear structure as described in Sec. 2.2.
- ▶ Use the pump field distribution to construct the nonlinear source term \mathbf{P}_2^{NL} at second-harmonic (SH) or third-harmonic (TH) frequency.
- ▶ Solve the field at SH or TH frequency by using an extended FMM which solves Eqs. (5.4) by transforming it into a linear but inhomogeneous algebraic system of equations in Fourier domain. This approach will be outlined in the next section.

With that, all quantities of relevance such as the forward and backward generated fields at SH or TH frequency are accessible.

5.2 Extended Fourier modal method

For the sake of readability we will omit the frequency related subscripts in the remaining derivation. In contrast to that, bare quantities are associated with the pump field at ω_1

and those with a bar on top are associated with the generated field at frequency ω_2 . The layer index l will be likewise omitted in order to avoid confusion with the remaining sub- and superscripts.

5.2.1 The nonlinear source term

Once having calculated the pump field in a specific layer, the nonlinear source term \mathbf{P}^{NL} can be constructed by using the general expression according to Eqn. (5.6). Owing to the periodicity of the nonlinear susceptibility tensor it can be expanded into a Fourier series, i.e.

$$\bar{\chi}^{i,j_1,\dots,j_N}(\mathbf{r}) = \sum_{m,n} \bar{\chi}_{mn}^{i,j_1,\dots,j_N} \exp [i(mK_x x + nK_y y)]. \quad (5.7)$$

Now, one has to remember that the concrete field distribution of the pump field is represented by a superposition of forward and backward propagating modes of a certain layer, having eigenvalues γ_s and $-\gamma_s$ (see Sec. 2.2.1). Due to the completeness of the numerical solution, these modes are linearly independent so that the forward and backward propagating modes may be divided into two disjoint subsets, namely Σ^+ and Σ^- , each containing S elements. Then, let s denote the mode index in the following running through the complete set of solutions, that is $\Sigma^+ \cup \Sigma^-$. Remembering that h is the thickness of the considered layer, then by defining

$$d_s = \begin{cases} 0 & \text{mode } \#s \in \Sigma^+ \\ h & \text{mode } \#s \in \Sigma^- \end{cases}, \quad \tilde{\gamma}_s = \begin{cases} \gamma_s & \#s \in \Sigma^+ \\ -\gamma_s & \#s \in \Sigma^- \end{cases}, \quad \nu_s = \begin{cases} a_s & \#s \in \Sigma^+ \\ b_s & \#s \in \Sigma^- \end{cases} \quad (5.8)$$

and substituting Eqn. (5.7) and the pump field distribution according to Eqn. (2.25) into Eqn. (5.6), one obtains

$$\bar{P}_i^{\text{NL}} = \epsilon_0 \sum_{\substack{\{s\} = \\ s_1, \dots, s_N}}^{2S, \dots, 2S} \sum_{m,n} \bar{P}_{imn}^{\{s\}} \exp \left[i \sum_{t=1}^N \tilde{\gamma}_{s_t} (\tilde{z} - d_{s_t}) \right] \exp [i(\bar{\alpha}_m x + \bar{\beta}_n y)], \quad (5.9)$$

where

$$\begin{aligned} \bar{\alpha}_m &= N\alpha_0 + mK_x \equiv \bar{\alpha}_0 + mK_x, \\ \bar{\beta}_n &= N\beta_0 + nK_y \equiv \bar{\beta}_0 + nK_y. \end{aligned} \quad (5.10)$$

In the above equation, the sum over indices m, n runs across the Fourier coefficients, whereas the sum over the set s_1, \dots, s_N accounts for all possible summands/combinations appearing when the electrical field (which is a sum over $2S$ eigensolutions) is raised to the power of

N . The coefficients $P_{imn}^{\{s\}}$ are defined according to

$$\bar{P}_{imn}^{\{s\}} = \prod_{t=1}^N \nu_{s_t} \cdot \sum_{\substack{p_1, \dots, p_N \\ q_1, \dots, q_N}} \bar{\chi}_{m-\sum_t p_t, n-\sum_t q_t}^{i, j_1, \dots, j_N} E_{j_1 p_1 q_1 s_1} \cdot \dots \cdot E_{j_N p_N q_N s_N}. \quad (5.11)$$

The indices in Eqn. (5.11) (especially those of the electrical field) are rather subtle, but one has to keep in mind that there are always four indices – the Cartesian component, the two Fourier domain indices and the eigenmode index. The quantity N designates the order of the generated higher harmonics field. As already mentioned, h is the thickness of the respective layer keeping in mind, that \bar{P}_i^{NL} according to Eqn. (5.9) also depends on the layer index l because both the nonlinear susceptibility $\hat{\chi}$ and the pump field depend on l . The quantities $E_{j p q s}$ and ν_s in Eqn. (5.11) denote the eigenvector components and the modal amplitudes of the pump field in the corresponding layer, no matter whether they belong to Σ^+ or Σ^- . The Fourier coefficients of the z -component E_3 of the electrical field entering Eqn. (5.11) which are not element of the actual eigenvector according to Eqn. (2.14) can be explicitly calculated by

$$\mathbb{E}_3 = -\frac{1}{k_0} \hat{\eta}(\hat{\alpha} \mathbb{H}_2 - \hat{\beta} \mathbb{H}_1) \quad (5.12)$$

where $\hat{\alpha}$ and $\hat{\beta}$ are Toeplitz matrices composed of the coefficients α_m and β_n [see Eqs. (2.9)-(2.10)] and η is defined according to Eqn. (2.20).

Finally, a short comment is required regarding the complexity of Eqs. (5.9) and (5.11). As already mentioned above, Eqn. (5.9) represents the Fourier expansion of the nonlinear polarization where it is written as a modal superposition of all eigenmodes. Eqn. (5.11) is a multiple convolution between the nonlinear susceptibility and the components of the pump field.

5.2.2 Solution within a single layer

After elucidating the rather sophisticated structure of the nonlinear polarization, the formal solution of the field at the higher-harmonic frequency ω_2 appears on the agenda. Due to the fact that the underlying linear properties, i.e. $\bar{\epsilon}(\omega)$, as well as the nonlinear polarization $\bar{\mathbf{P}}^{\text{NL}}$ are periodic or pseudo-periodic functions in the x - y -plane, the components of the electromagnetic field in a specific layer l will again obey the Bloch theorem, i.e.

$$\bar{f}_i(\mathbf{r}) = \sum_{m,n} \bar{f}_{imn}(\tilde{z}) \exp [i(\bar{\alpha}_m x + \bar{\beta}_n y)]. \quad (5.13)$$

Again, the layer index is omitted in the following formulas. Now, the procedure is similar to that in the linear case. By introducing Eqn. (5.13) into the inhomogeneous Maxwell's equations (5.4) and by applying the correct Fourier factorization rules as outlined in Sec. 2.2 the result is a system of first-order differential equations, i.e.

$$-i \frac{\partial}{\partial \tilde{z}} \bar{\mathbb{X}}(\tilde{z}) = \hat{M} \bar{\mathbb{X}}(\tilde{z}) + \bar{\mathbb{Q}}(\tilde{z}). \quad (5.14)$$

The matrix \hat{M} is exactly the one used in Eqn. (2.12) except that all quantities should carry bars on top, meaning that they are evaluated at frequency $\omega_2 = N\omega$. The vector $\bar{\mathbb{X}} = (\bar{\mathbb{E}}_1, \bar{\mathbb{E}}_2, \bar{\mathbb{H}}_1, \bar{\mathbb{H}}_2)^T$ includes the Fourier components of the four field vector components. The term $\bar{\mathbb{Q}}$ writes as

$$\bar{\mathbb{Q}}(\tilde{z}) = \sum_{\{s\}} \begin{pmatrix} -\hat{\alpha} \hat{\eta} \bar{\mathbb{P}}_3^{\{s\}} \\ -\hat{\beta} \hat{\eta} \bar{\mathbb{P}}_3^{\{s\}} \\ -\bar{k}_0 \bar{\mathbb{P}}_2^{\{s\}} \\ \bar{k}_0 \bar{\mathbb{P}}_1^{\{s\}} \end{pmatrix} \exp [i \sum_t \tilde{\gamma}_{st} (\tilde{z} - d_{st})] \equiv \sum_{\{s\}} \bar{\mathbb{Z}}^{\{s\}} \exp [i \sum_t \tilde{\gamma}_{st} (\tilde{z} - d_{st})]. \quad (5.15)$$

The definition of $\hat{\eta}$ is again given in Eqn. (2.20), and $\hat{\alpha}$ and $\hat{\beta}$ are nothing else than Toeplitz matrices composed of the elements $\bar{\alpha}_m$ and $\bar{\beta}_n$, respectively.

The solution to Eqn. (5.14) consists of a general solution $\bar{\mathbb{X}}^H$ of the homogeneous equation and a particular solution $\bar{\mathbb{Y}}(\tilde{z})$. The homogeneous equation is nothing else than Eqn. (2.12) so that its solution is given by $\bar{\mathbb{X}}^H(\tilde{z}) = \hat{W} \hat{\phi}(\bar{\mathbf{a}}, \bar{\mathbf{b}})^T$ [see Eqn. (2.25)]. For the sake of brevity, the derivation of the particular solution will not be shown here explicitly, instead the interested reader is referred to Ref. [TP13].

5.2.3 The boundary conditions

Once the particular solution inside each layer is known, the enforcement of the boundary conditions, i.e. the tangential electromagnetic field components must be continuous on the layers' boundaries, will lead to the solution of the still unknown modal amplitudes of the homogeneous solution $\bar{\mathbb{X}}^H$. As an example, let us consider the interface between layer l to layer $l+1$ in the following. Then, the continuous transition of the lateral (tangential) field components implies

$$\hat{W}^{(l)} \begin{pmatrix} \bar{\mathbf{a}}^{(l)} \\ \bar{\mathbf{b}}^{(l)} \end{pmatrix} + \bar{\mathbb{Y}}^{(l)}(h^{(l)}) = \hat{W}^{(l+1)} \begin{pmatrix} \bar{\mathbf{a}}^{(l+1)} \\ \bar{\mathbf{b}}^{(l+1)} \end{pmatrix} + \bar{\mathbb{Y}}^{(l+1)}(0), \quad (5.16)$$

where the elements of the underlined vectors are defined as $\underline{\bar{a}}_q^{(l)} = \bar{a}_q^{(l)} \exp(i\bar{\gamma}_q^{(l)} h^{(l)})$ and $\underline{\bar{b}}_q^{(l)} = \bar{b}_q^{(l)} \exp(i\bar{\gamma}_q^{(l)} h^{(l)})$. In contrast to the fundamental field, Eqn. (5.16) additionally contains the terms of the particular solutions on both sides of the interface. Of course, assuming that $\bar{\Upsilon}^{(l)}$ and $\bar{\Upsilon}^{(l+1)}$ are exactly zero, then the solution to the boundary conditions can be achieved by a standard S-matrix scheme as it was presented in Sec. 2.2.2. In that sense, the aim of the following derivation is to end up with an extended scattering matrix solution scheme which contributes for the existence of the additional terms appearing in Eqn. (5.16). Henceforth, the subsequently outlined approach will be used. It finally allows to determine the overall scattering matrix of an arbitrary multi-layer structure.

- ▶ Determine the transfer matrix (T-matrix) for the transition of the fields at the interface between any arbitrary layer l and $l + 1$.
- ▶ Determine the transfer matrix for the propagation of the fields through an arbitrary layer l , in particular from $\tilde{z} = 0$ to $\tilde{z} = h$.
- ▶ Determine the transformation rules of a T-matrix into an S-matrix.
- ▶ Determine the concatenation rules for two different S-matrices.

The first step, that is the determination of the interface T-matrix, is quite simple. By solving Eqn. (5.16) for the modal field amplitudes of layer $(l + 1)$ it follows

$$\begin{aligned} \begin{pmatrix} \bar{\mathbf{a}}^{(l+1)} \\ \underline{\bar{\mathbf{b}}}^{(l+1)} \end{pmatrix} &= \left(\hat{W}^{(l+1)} \right)^{-1} \hat{W}^{(l)} \begin{pmatrix} \bar{\mathbf{a}}^{(l)} \\ \underline{\bar{\mathbf{b}}}^{(l)} \end{pmatrix} + \left(\hat{W}^{(l+1)} \right)^{-1} [\bar{\Upsilon}^{(l)}(h^{(l)}) - \bar{\Upsilon}^{(l+1)}(0)] \\ &\equiv \bar{\tau}_{\text{layer}} \begin{pmatrix} \underline{\bar{a}}_q^{(l)} \\ \underline{\bar{b}}_q^{(l)} \end{pmatrix} + \bar{\mathbf{v}}_{\text{layer}}. \end{aligned} \quad (5.17)$$

Thus, the calculation of the modal field amplitudes of layer $l + 1$ follows directly from ordinary matrix operations from the corresponding coefficients in layer l . The second step, that is to describe the propagation through a particular layer l from 0 to $h^{(l)}$, consists in the multiplication of the modal field amplitudes by the propagation kernel $\bar{\phi}^{(l)}(h^{(l)})$ which results in

$$\begin{pmatrix} \bar{\mathbf{a}}^{(l)} \\ \underline{\bar{\mathbf{b}}}^{(l+1)} \end{pmatrix} = \hat{\phi}^{(l)}(h^{(l)}) \begin{pmatrix} \bar{\mathbf{a}}^{(l)} \\ \underline{\bar{\mathbf{b}}}^{(l)} \end{pmatrix} \equiv \hat{\tau}_{\text{free}} \begin{pmatrix} \bar{\mathbf{a}}^{(l)} \\ \underline{\bar{\mathbf{b}}}^{(l)} \end{pmatrix} + \bar{\mathbf{v}}_{\text{free}}. \quad (5.18)$$

The empty vector $\bar{\mathbf{v}}_{\text{free}} = 0$ has been added to keep the structural form of the equation equal to that of Eqn. (5.17). Eventually, Eqs. (5.17) and (5.18) are already the basic relations which allow to impose the boundary conditions for an arbitrary multi-layer structure. In principle, establishing the concatenation between different transfer matrices would allow

for the determination of the overall transfer matrix of the complete structure. However, due to known numerical instabilities of this solution scheme, the entire description has to be transformed into a scattering matrix formulation circumventing these drawbacks. Due to the limited amount of space available for the major part of this thesis, the detailed transformation and concatenation rules are omitted here, but they are documented in Ref. [TP13].

5.3 Second-harmonic generation at a single-wire structure

The following structure under investigation is deliberately chosen to be quite simple. It is a periodic arrangement of metallic nano-wires deposited on a film of a nonlinear dielectric material. Figure 5.1a shows the pertinent structure. The metallic wires consist of gold,

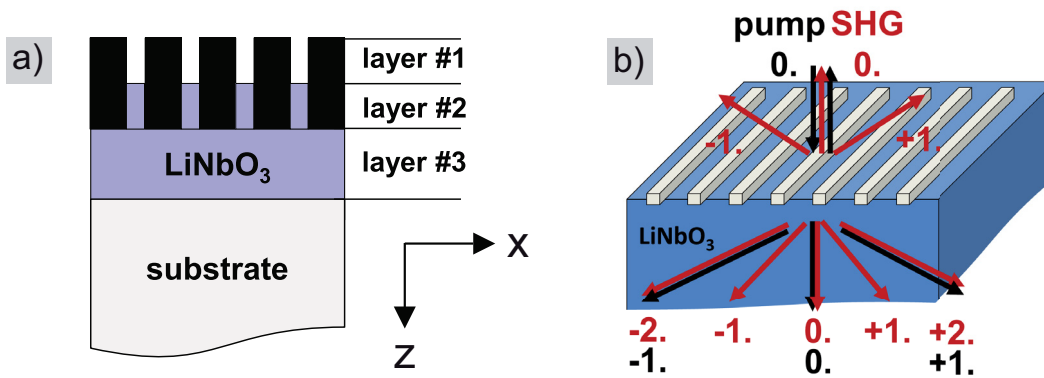


Figure 5.1: Schematic (a) of the structure. Three separate layers are indicated and labeled. Sketch of the eigenmodes (b) propagating within the homogeneous LiNbO₃ layer which corresponds to layer #3.

they are 400 nm in width and 30 nm in height. The film material (layer #3) is assumed to be lithium niobate (LiNbO₃) which exhibits a strong second-order susceptibility. The period of the metallic wires is 0.61 μm and the voids are assumed to be partially filled by LiNbO₃ of height 15 nm. To bury the nano-wires is beneficial if the large field enhancement close to the metal surface shall be exploited. The actual substrate material is assumed to be linear and isotropic with its dielectric properties identical to that of LiNbO₃ (more precisely the ordinary dielectric coefficient of LiNbO₃ is chosen). On the one hand, this configuration is necessary because the algorithm requires linear substrate/cladding media. On the other hand, it minimizes interfering Fabry-Perot-oscillations that will appear due to the finite thickness of the LiNbO₃ film (#3 in Fig. 5.1a) and therewith it helps to keep the physics as simple as possible.

Now, in the following investigations we wish to evaluate the influence of the localized plasmon-polariton resonance (supported by the small metallic nano-wires) on SHG. In the following, only the dielectric film material is assumed to contribute to the nonlinear conversion process and the contribution of the metallic components is neglected. This assumption appears to be quite realistic since the pure metal itself does not support a dipolar second-order nonlinearity of bound lattice electrons which is forbidden due to the crystallographic symmetry [191]. Other contributions, such as a quadrupolar response of valence electrons [193, 194] and also those of the conduction electrons of the metal [TP11, 178, 193, 195, 196] are very small and can be neglected in comparison to the LiNbO₃ [TP11].

To excite a localized plasmon-polariton resonance supported by the metallic nano-wires, the illuminating field has to be polarized along the x -direction. The cladding material is air and the structure is illuminated under normal incidence with a plane wave. To distinguish between the contribution from the plasmonic nano-structure and from the remaining bulk material, the thickness of layer #3 is systematically varied and its impact on SHG is analyzed. For a better understanding of the physical processes in the chosen example it appears to be advantageous to be clear about the eigenmodes of the structure, especially those for the nonlinear dielectric film, i.e. layer #3. Due to the fact that layer #3 is a simple homogeneous film, the excitable modes (at FH and SH frequency) are plane waves; nothing else than the diffraction orders of the metallic grating defined by the nano-wires. Thus, the lateral Bloch vector components k_x of these modes are determined by an integer multiple of the reciprocal lattice vector, i.e. $k_x = 2\pi q/\Lambda_x$ ($q = 0, \pm 1, \pm 2, \dots$), and the associated longitudinal components are given by $k_z = \sqrt{n_{\text{LiNbO}_3}^2(\omega_{1/2})\omega_{1/2}^2/c^2 - k_x^2}$. Here, n_{LiNbO_3} denotes the refractive index experienced by the associated eigenmode* and $\omega_{1/2}$ is the FH frequency and SH frequency, respectively. A schematic overview of the propagating modes at both frequencies is provided by Fig. 5.1b. Assuming a weak material dispersion of LiNbO₃, it becomes obvious that the even modes ($q = 0, \pm 2, \dots$) at SH frequency have *co-propagating* modes at FH frequency of order $q/2$. On the contrary, the odd modes at SH frequency ($q = \pm 1, \pm 3, \dots$) are not accompanied by a co-propagating mode existing at FH frequency. From that picture, and without having examined the numerical results up to this point, it is expected that the material dispersion of LiNbO₃ leads to a small phase mismatch between co-propagating modes at SH and FH frequency within layer #3. Thus, the bulk contribution will lead to a sinusoidal dependence of the even modes at SH frequency. As will be shown later, the contribution of the metallic nano-structure appears as an offset in the generated signal. On the contrary, the SH signal generated within the odd modes will turn

*Due to the anisotropy of the LiNbO₃ crystal this value is not constant and depends on the direction of propagation. However, to establish a qualitative picture of the physical scenario this fact is of minor importance.

out to be solely determined by the near field contribution of the metallic nano-structure. Due to the large phase mismatch to the neighboring modes at FH frequency, an efficient frequency conversion process within the homogeneous nonlinear layer #3 is not achievable. Now, a precise description of the material components of the system is provided. The LiNbO₃ crystal establishing the film is aligned in a z -cut configuration (the optical axis of the crystal coincides with the z -axis). In this configuration the non-vanishing elements of the second-order susceptibility tensor are [191] $\chi^{113} = \chi^{131} = \chi^{223} = \chi^{232} = \chi^{311} = \chi^{322} = -5.44 \times 10^{-12}$ m/V, $\chi^{222} = -\chi^{211} = -\chi^{112} = -\chi^{121} = 2.76 \times 10^{-12}$ m/V and $\chi^{333} = -31.8 \times 10^{-12}$ m/V. The linear permittivity tensor is diagonal, with its entries $\epsilon^{11} = \epsilon^{22} = \epsilon_o$ and $\epsilon^{33} = \epsilon_e$. Here, ϵ_o and ϵ_e denote the ordinary and extraordinary dielectric coefficients of the uniaxial LiNbO₃ crystal. The material dispersion characteristics were directly taken from literature [M.3]. It has to be mentioned, that the following calculation completely takes into account the anisotropic properties of the LiNbO₃ structure, whereas the numerical procedure presented in Sec. 5.1 only dealt with isotropic constituents. However, an extension to anisotropic material properties is straightforward [TP13] and does not considerably change the numerical scheme as it was presented.

Results and discussion. Now, let us first consider the linear transmission spectrum of the pump field. The spectrum was recorded for a pump field between $1.2 - 1.6 \mu\text{m}$ illuminated under normal incidence with an amplitude of $|E| = 10^6$ V/m. The polarization was linear along the x -direction and 101 Fourier orders were used in the calculation. Figure 5.2a shows the zeroth-order transmission coefficient (blue, dashed curve). The height of the nonlinear LiNbO₃ film was set to be 1 mm, which corresponds to the usual thickness of commercially available wafers of that material. The transmission minimum which is connected to the fundamental plasmonic resonance of the nano-wire is centered around $\lambda_0 = 1.41 \mu\text{m}$. The manifold small features below $1.3 \mu\text{m}$ are caused by the appearance of a new propagating diffraction order in transmission such that the structure is no longer sub-wavelength with respect to the pump wavelength. Looking at the SHG process, Fig. 5.2a shows the normalized forward generated (transmitted) field[†] into the zeroth (red, dashed-dot) and the first diffraction order (green, solid) SH field. On the one hand, the first-order SH field clearly takes advantage of the plasmonic resonance of the pump field such that a local maximum can be identified within the spectrum. In contrast to that, the zeroth-order SH field is dramatically smaller and obviously cannot benefit from the excited plasmon polariton. Moreover, it exhibits a broad dip in the transmission spectrum (hardly to see at the chosen scale)

[†]The amplitude transmission coefficients are normalized to the input pump field which has an amplitude of $|E| = 10^6$ V/m.

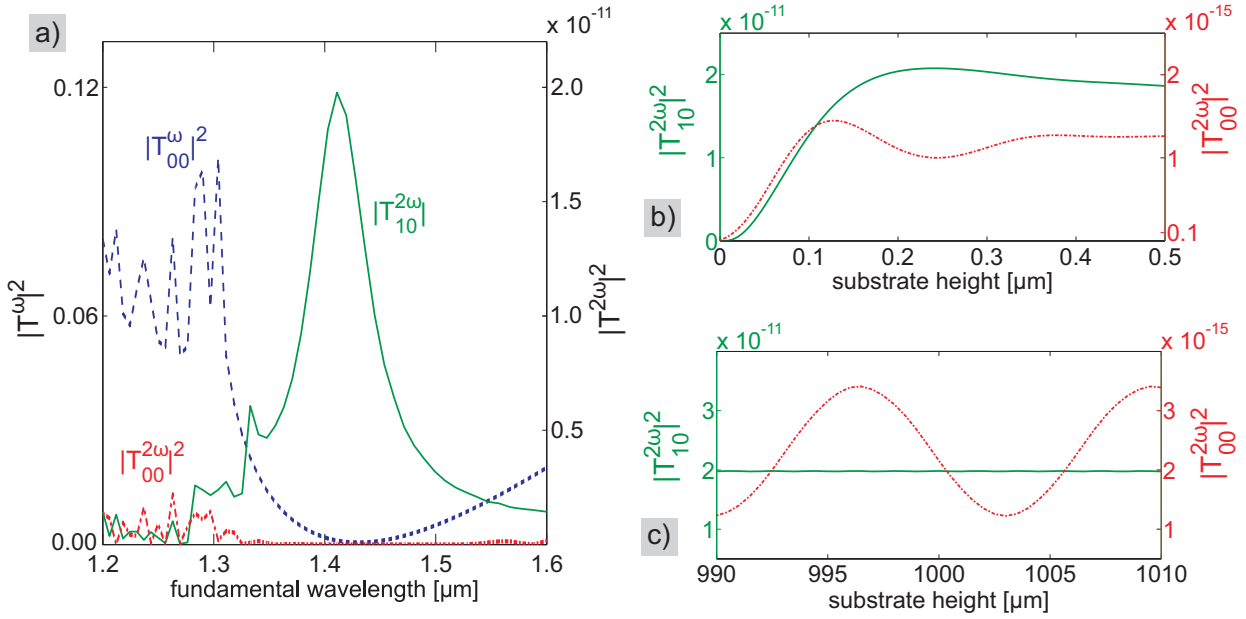


Figure 5.2: Transmission spectra (a) of the zeroth-order FH (blue, dashed), the zeroth-order SH (red, dash-dot) and the first-order SH fields (green, solid) under normal incidence. Forward generated (transmitted) SH field (b and c) of the zeroth (red, dash-dot) and first-order (green, solid) SH field at $1.41\mu\text{m}$. The dependence on the assumed nonlinear substrate height (layer #3) is explicitly shown. These graphs show the very near field behavior (b) from 0 to $0.5\mu\text{m}$ and also the characteristics far away from the nano-structure (c) around a layer thickness of $1000\mu\text{m}$.

which is linked to the associated dip in the transmission of the pump field. The reason why the first order shows a much stronger signal, can be most likely attributed to the z -cut geometry where the χ^{333} component is largest. However, the related nonlinear source field at SH frequency must not radiate into z -direction but may stipulate radiation into higher diffraction orders.

To further elucidate the nonlinear frequency conversion process, the SH conversion efficiency depending on the thickness of the nonlinear LiNbO_3 film is also studied. Figures 5.2b and 5.2c show the results for a fixed wavelength of $1.41\mu\text{m}$ which corresponds to the plasmonic resonance position of the pump field. At first, there is a strong increase of the generated SH signal (see Fig. 5.2b) within a distance of $100 - 200\text{nm}$ near the plasmonic structure which saturates for higher thicknesses of the LiNbO_3 film. This behavior indicates the near field of the metallic nano-wires to be responsible for that amount of SHG. Thus, in the present case the zeroth and first-order SH field converge towards values of 1.2×10^{-15} and 2.0×10^{-11} , respectively. But what happens over larger distances? At first, the first-order SH field (blue, solid curve) shows a constant signal (see Fig. 5.2c) indicating that no further SHG process does contribute. This fact appears to be reasonable since the

first-order SH field has no co-propagating counterpart of the pump field within the LiNbO_3 film (the first-order pump overlaps the second-order SH field) such that an efficient nonlinear frequency conversion is not possible. Consequentially, the entire spectral contribution within this order is generated in the vicinity of the nano-structure. It explicitly takes advantage of the electric field enhancements around the metallic nano-wires. On the other hand, inspecting the zeroth-order SH field, it undergoes strong oscillations (see Fig. 5.2c) when inspected over large distances. The oscillation period exactly corresponds to the coherence length of LiNbO_3 at that wavelength [191]. It is caused by the phase mismatch between the zeroth-order pump and SH field.

In conclusion, once the SH has experienced a strong increase over very small distances around the metallic nano-structure, the ordinary bulk SHG process takes over and determines the frequency conversion process. Most notably, the near field contribution represents an additional amount of generated SH which is not again annihilated by the ordinary bulk conversion process. In particular, this means that the phase-mismatch evoked oscillations do not cause the signal to go down to zero again, instead the minimum value is determined by the near field contribution which can be addressed to the impact of the employed metallic nano-wires.

5.4 Third-harmonic generation at a coupled plasmonic-dielectric structure

In the following section, the focus will turn to THG assisted by metallic nano-structures. In that case, the situation with respect to the origin of the nonlinear response gets more involved. In contrast to SHG, the nonlinear properties will be influenced by the dielectric as well as metallic constituents of a certain realistic, metallic nano-structure. In particular, the metallic components do exhibit a reasonable third-order, dipolar nonlinearity stemming from the bound electrons that cannot be neglected anymore [178, 191, 194].

The upcoming investigation is closely related to a genuine experimental study of THG assisted by metallic nano-structures [TP12]. The experiments were performed by *T. Utikal* and co-workers at the *University of Stuttgart*. The system under consideration is a hybrid plasmonic dielectric configuration, namely an array of gold nano-wires that are completely embedded into a dielectric slab waveguide. Particularly to note, the peculiar influence of the employed dielectric waveguide material on the THG process was at the heart of interest such that different materials with different (nonlinear) properties were employed. However, the following theoretical study will concentrate on a single and carefully chosen geometrical

layout. The influence of the different constituent materials on the overall nonlinear response by means of numerical calculations can be simply investigated by a manipulation of the material's nonlinear properties; a way which is of course experimentally not feasible. However, this strategy is not just a simple ruse/trick, instead it appears to be highly preferable since it simultaneously allows to maintain the linear optical properties.

A sketch of a single unit cell of the pertinent structure is depicted in the inset of Fig. 5.3a. The precise specification is the following. The substrate of the structure is established by

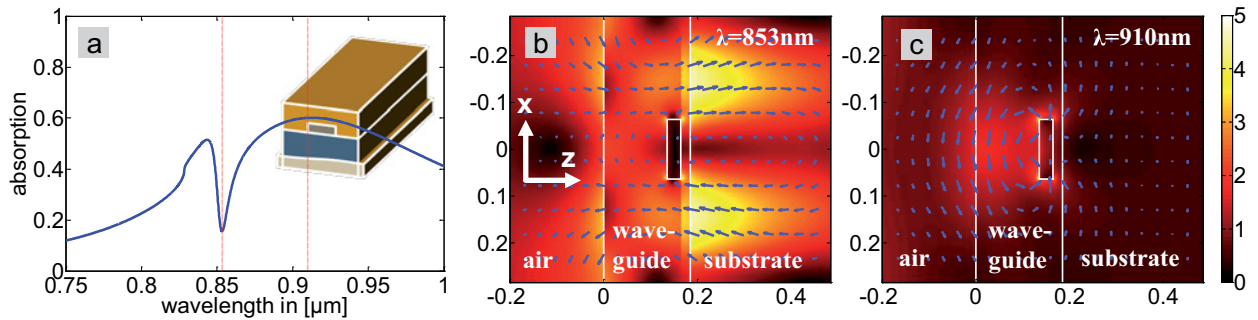


Figure 5.3: a) Linear absorption spectrum of the structure. The inset shows the structure layout. b&c) Field distribution within a single period of the electrical field at two different wavelengths evaluated at the thin red lines in the left picture. The color scale encodes the amplitude of the total electrical field. The arrows indicate the direction and strength of the field. The axis values are given in 10^{-6} m.

a fused silica wafer [M.4] (bottom grey layer) which is coated (manufacturer-provided) by a 20 nm indium thin oxide (ITO) layer (dark blue layer). For the numerical simulation the actual fused silica substrate is divided into two sections – an analogue strategy was already discussed in context of SHG in the previous section. The 20 nm ITO layer is followed by a 300 nm layer of fused silica where third-order nonlinear properties are taken into account. Then, the actual substrate material is exclusively linear with its properties according to fused silica. The metallic wires (dark gray stripes) consist of gold [M.6] and they are directly located on top of the wafer. They were deposited by a sputtering technique. Their width and height amount to 128 nm and 30 nm. The period of the arrangement is 570 nm. Finally, the wires are embedded in a second ITO layer (brown layer) with a thickness of 135 nm which was again deposited on top of the sample by a sputtering procedure. Hence, the overall thickness of the ITO waveguide amounts to 185 nm. The linear optical properties of the two ITO layers are treated slightly different which accounts for the different techniques used for their deposition. Consequently, the material dispersion of the 20 nm ITO layer is modeled by data provided by the manufacturer [M.5] whereas the sputtered film has a constant permittivity of 4.0^{\ddagger} . However, this discrimination is of marginal importance for the understanding of the

[‡]The permittivity of the sputtered film was extracted from experiments.

physical processes, but of course it will slightly influence the quantitative results. Finally, the incident field is assumed to be a plane wave which impinges perpendicular to the structure's surface. The polarization state is linear with the electrical field perpendicular to the metallic wires such that localized plasmon polaritons can be excited. On the other hand, for the chosen geometrical parameters the periodic arrangement of the wires simultaneously allows coupling of the external illuminating field to photonic waveguide modes in the dielectric ITO slab. In the strong coupling regime the localized plasmonic mode hybridizes with the waveguide mode to form two so-called *waveguide plasmon polaritons*. These polaritons are characterized by two absorption maxima in the linear spectrum with an absorption dip in between [101, 197–199]. For the chosen example, the two spectral maxima are located at wavelengths of $0.84 \mu\text{m}$ and $0.91 \mu\text{m}$ and the dip position is $0.853 \mu\text{m}$ (see Fig. 5.3a).

In order to gain more insight into the elementary processes especially for the nonlinear conversion processes as discussed later, the electrical field distributions were exemplarily calculated in the linear optical regime for $\lambda = 0.853 \mu\text{m}$ and $\lambda = 0.910 \mu\text{m}$. These wavelengths correspond to the dip and the long wavelength maximum positions. The field distributions are shown in Figs. 5.3b and 5.3c. Characteristically, one observes a strong field concentration in the waveguide and in the substrate for $\lambda = 0.853 \mu\text{m}$, whereas the field is mainly concentrated around the metal for $\lambda = 0.910 \mu\text{m}$. In the first case, the field distribution resembles that of an ideal slab waveguide which is, however, slightly disturbed due to the presence of the metallic nano-wires. Thus, the field shows two bumps along the x -direction which can be attributed to the interference pattern between two equally excited waveguide modes propagating in $\pm x$ -direction. Furthermore, the field evanescently penetrates into the substrate and cladding, where the characteristic depth of penetration into the substrate clearly overwhelms that into air which is caused by the higher substrate's permittivity. In the second case, the field distribution reveals that of an elementary dipole which clearly emphasizes the resonance to be linked to the fundamental localized plasmonic mode of the metallic nano-wire.

Results and discussion. In the following, the local third-order nonlinear polarization was assumed to be described by $\mathbf{P}^{\text{NL}}(3\omega, \mathbf{r}) = \epsilon_0 \hat{\chi}(-3\omega; \omega, \omega, \omega, \mathbf{r}) : \mathbf{E}^3(\omega, \mathbf{r})$ fully taking into account the dipolar bulk contributions of the involved materials. A simultaneously emerging Kerr nonlinearity leading to an additional nonlinear polarization at frequency ω was not taken into account. There are two reasons for that. On the one hand, the consideration of a Kerr nonlinearity is beyond the numerical model as it was presented here and it was not implemented into the software used for the present calculations (however it is possible; see e.g. Ref. [192]). On the other hand and even more important, the experimental inves-

tigations have shown a negligible influence of the applied input intensity on the measured spectra at FH frequency ω .

Now concentrating on the THG process, all materials were assumed to be isotropic with a cubic lattice such that the complete susceptibility tensor is determined by a single value/entry [191, 200], w.l.o.g. it is χ^{1111} . The precise values were taken from literature [191, 201–203] and they amount to $\chi_{\text{Au}}^{1111} = 7.5 \times 10^{-19} \text{ m}^2/\text{V}^2$ for gold, $\chi_{\text{ITO}}^{1111} = 1.0 \times 10^{-20} \text{ m}^2/\text{V}^2$ for ITO and $\chi_{\text{glas}}^{1111} = 2.0 \times 10^{-22} \text{ m}^2/\text{V}^2$ for fused silica. Now, to investigate the influences of the different constituent materials (gold, ITO, fused silica) on the nonlinear frequency conversion process a switch on/off technique was used, meaning that only one of these susceptibilities was taken into account during the numerical calculation whereas the remaining ones were set to zero. At first, the calculations have revealed that the influence of the substrate ($\chi_{\text{glas}}^{1111}$) can be neglected because the corresponding TH signal intensity is 2-3 orders of magnitude smaller than that generated by the remaining materials. Moreover, the shape of the spectral response, which will be subsequently discussed in detail, nicely resembles that induced by the dielectric waveguide material. Thus, in the real experiment they are hardly distinguishable. To discuss the effects of the remaining materials, let us start with

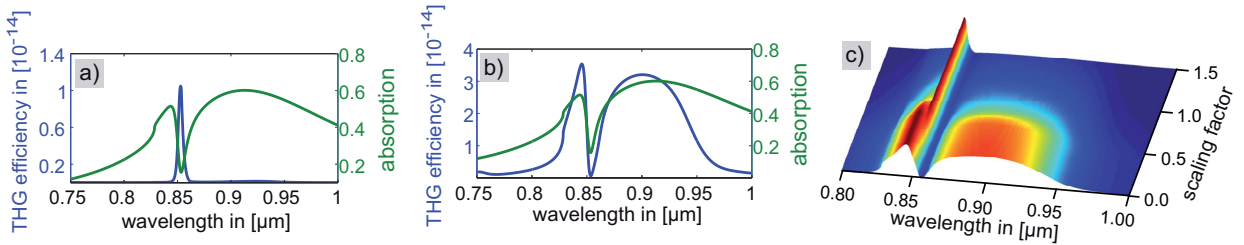


Figure 5.4: Forward, normalized THG efficiency (blue, solid curve) evaluated over all propagating diffraction orders. In the first case (a) only the dielectric waveguide material contributes to the nonlinear response, i.e. $\chi_{\text{ITO}}^{1111} \neq 0$ and $\chi_{\text{Au}}^{1111} = 0$. In the second case (b) only the metallic wires contribute to the nonlinear response, i.e. $\chi_{\text{ITO}}^{1111} = 0$ and $\chi_{\text{Au}}^{1111} \neq 0$. In the last case (c) both components contribute to the nonlinear response. Additionally, the relative strength between χ_{ITO}^{1111} and χ_{Au}^{1111} is subject to variations. Therefore, the ITO's nonlinear coefficient is scaled by a factor $10^{f_{\text{ITO}}}$ leading to a manipulated strength of the third-order nonlinearity, i.e. $\chi_{\text{ITO}}^{1111} \rightarrow 10^{f_{\text{ITO}}} \chi_{\text{ITO}}^{1111}$. For the sake of visibility the spectra are individually normalized for every value of f_{ITO} .

the dielectric component, namely the ITO waveguide layer. Consequentially, it is assumed that $\chi_{\text{ITO}}^{1111} \neq 0, \chi_{\text{Au}}^{1111} = 0$. Figure 5.4a shows the corresponding results. The generated TH signal strength (blue curve) in forward direction (into the substrate) is plotted as a function of the wavelength of the pump field. Hence, the actual wavelength of the TH signal is one third of the displayed values. The THG efficiency is determined by the intensity

of the generated field into all diffraction orders normalized to the intensity of the input field which has an amplitude of $|\mathbf{E}| = 10^6$ V/m. For comparison, Fig. 5.4a also displays the linear absorption spectrum at the pump field frequency. Thus, it can be seen that the THG induced by the waveguide material is characterized by a sharp peak which is located exactly at the dip position of the linear absorption spectrum. Remembering the exemplary field distributions provided by Figs. 5.3b and 5.3c, then it can be concluded that this THG peak must be linked to the peculiar distribution of the pump field which takes here the form of two counter-propagating waveguide modes as discussed above. On the contrary, when looking at the influence of the gold nano-wires (now: $\chi_{\text{ITO}}^{1111} = 0, \chi_{\text{Au}}^{1111} \neq 0$) it becomes obvious that the associated THG process leads to a spectral shape of the signal which nicely follows the linear absorption curve of the pump field exciting the nano-structure. In particular, there are two distinct maxima observable which are connected to the excitation of the waveguide plasmon polariton states in the nano-structure. Thus, this fact indicates that the underlying frequency conversion process takes advantage of the plasmonic nature of the resonance as suggested by Fig. 5.3c. Eventually, a last note is necessary with respect to the strengths of the contributions from both materials. They can be seen to be of the same order of magnitude[§]. Thus, the question arises what happens when both of them contribute to the overall nonlinear response and what is the influence of slight variations in their relative strength (now: $\chi_{\text{ITO}}^{1111} \rightarrow 10^{f_{\text{ITO}}} \chi_{\text{ITO}}^{1111} \neq 0, \chi_{\text{Au}}^{1111} \neq 0$). To realize this investigation the absolute value of χ_{ITO}^{1111} will be subject to variations in the following. It will be modified by an additional factor $10^{f_{\text{ITO}}}$. Finally, performing the numerical calculations once again leads to the results as displayed by Fig. 5.4c which shows the normalized THG efficiency depending on the wavelength as well as the scaling factor's exponent f_{ITO} . For $f_{\text{ITO}} = 0$ one can see the final response to be dominated by the nano-wire's contribution attributed to the nonlinear susceptibility of gold. However, increasing the strength of the ITO's susceptibility only by one order of magnitude then the ITO's contribution takes over. Worth to mention, there appears a smooth and continuous transition between the characteristic features of both limiting spectra. In particular, there are no coupling or interfering effects between both contributions observable in the transition region around $f_{\text{ITO}} = 0.5$.

5.5 Chapter summary and concluding remarks

The first part of this chapter was devoted to the brief presentation of a numerical scheme, namely an adapted Fourier modal method, allowing for the rigorous calculation of SHG

[§]The precise strengths of both spectra are less reliable since they strongly depend on the concrete numerical value assumed for the nonlinear susceptibility. Here, the exact parameters are only vaguely known due to the very limited number of available experiments performed to determine them.

and THG at periodic nano-structures in context of the undepleted pump approximation. This method was then used to analyze SHG and THG for two specific example structures. The first structure was a periodic arrangement of metallic nano-wires on top of a dielectric wafer. The dielectric material was chosen to exhibit a large second-order, nonlinear susceptibility. The presence of the metallic nano-wires was verified to affect and enhance the SH conversion efficiency. Moreover, it was demonstrated how to distinguish between ordinary bulk contributions and the peculiar near field contributions attributed to the effect of localized plasmon polariton resonances. The second structure under investigation was a hybrid metallo-dielectric system. The focus was on THG. In the considered case, several material components of the entire nano-structure contributed to the overall frequency conversion process due to their third-order nonlinear susceptibility. Using a switch on/off technique it was possible to show that all different materials induced unique characteristic features in the recorded TH signal. Conversely, this means that the measured spectral features may allow to identify the actual source of the TH response in a real experiment [TP12].

6 Summary and conclusion

Summary

The major aim of this thesis was the study of concepts to describe light propagation in periodic, inhomogeneous nano-structures, i.e. metamaterials (MMs). Though the feature size of typical optical MMs is clearly sub-wavelength, it is still too large to describe them entirely in terms of effective homogeneous media. Thus, the exact description of light propagation within optical MMs typically requires three-dimensional, full-vectorial, numerical models. However, independent from the chosen method and following the concepts of solid state physics, the description of light propagation within periodic MMs can be confidently developed relying on the eigenmodes, i.e. the Bloch modes, of such media. In fact, the last sentence exactly points out the essence of the current thesis. It was devoted to the modification of concepts for electronic transport in solid state physics [89] and to apply it to the propagation of light in MMs. In particular, the concept of the eigenmodes' dispersion relation was introduced and widely exploited where the challenge, e.g., in contrast to photonic crystals [21] was mainly attributed to the absorbing nature of contemporary MMs. After a concise summary of the numerical procedure, namely the Fourier modal method, used for intended, rigorous numerical calculations, Chap. 3 was devoted to the very general properties of Bloch modes in absorbing, periodic media. At first, orthogonality relations were derived and the peculiarities and differences in comparison to purely dielectric media (e.g. photonic crystals) were elaborated. It was then shown how to use the orthogonality relations for the decomposition of arbitrary field distributions (e.g. beams) into the Bloch eigenmodes. This concept, as it was discussed later on, finally allowed for the characterization of diffraction in and refraction at MMs thoroughly by means of the dispersion relation of the Bloch eigenmodes of the underlying medium. Apart from light propagation within pure bulk MMs, also the coupling/scattering of light at the interface between two, dissimilar MMs was treated. Hence, in analogy to the Fresnel coefficients for ordinary homogeneous media, self-consistent expressions for the reflection and transmission coefficients in terms of the Bloch modes of both media were derived and presented. Most notably, the fundamental mode approximation was then introduced which allowed for the derivation of simplified, analytic expressions.

The elaborated, formal concepts were then applied in Chap. 4 to the specific analysis of contemporary, realistic MM structures. Emphasis was put on *left-handed* MMs, in particular, on the large class of fishnet MMs. In a first part, the dispersion relation of a given fishnet structure was presented and thoroughly analyzed. Most important, it was shown that a negative phase velocity (or negative phase index) is neither necessary nor sufficient to achieve negative refraction or anomalous diffraction – the most appealing properties promised by *left-handed* media. These predictions were confirmed by rigorous numerical calculations performed, amongst others, to evaluate the imaging capabilities of a flat fishnet MM slab. Hence, the fishnet was shown to support ordinary refraction while simultaneously providing a negative phase velocity.

In the second part of Chap. 4 a new and innovative design approach for MMs, namely a super-cell structure, was presented. It suggested the purposive use of heterogeneous multi-layer MMs to suitably tailor the dispersion relation of the Bloch eigenmodes. Hence, two novel fishnet MMs were presented to demonstrate the strength and versatility of that approach; one which exhibits an isotropic optical response (possessing a circular angular dispersion relation) and the second one which enables the propagation of self-collimated beams. In the third and last part of Chap. 4 the focus moved towards the description of light reflection and transmission at MM interfaces. Using the fundamental mode approximation, an important criterium, namely the proper dilution of meta-atoms or meta-atom layers, was formulated which must be considered as a prerequisite for a successful homogenization of layered MMs. The Swiss cross MM was chosen to serve as an example and to demonstrate the physical implications.

The final chapter was dedicated to nonlinear optics or, to be more precise, to second- and third-harmonic generation (SHG and THG). Apart from the presentation of an extended Fourier modal method allowing for the rigorous description of SHG and THG at periodic nano-structures, the special interest lay on the specific synthesis of the frequency converted signal in metal-dielectric nano-structures. The first investigated structure was composed of metallic nano-wires on top of a dielectric wafer. It was exemplarily shown how to distinguish between ordinary bulk contributions and the peculiar near field contributions attributed to the effect of localized plasmon polariton resonances. The second structure was a so-called hybrid metallo-dielectric system. Here, the peculiar contributions of different material components to the overall nonlinear response helped to reveal different resonant mechanisms which are responsible for the enhancement of THG in that case.

Perspective

This thesis has presented fundamental concepts to treat light propagation in periodic MMs. However, it only covers a limited domain from a huge framework, so there are several points that might be subject to further research in the future. First of all, the technical framework of Bloch modes in absorptive media is very general and it can be applied to any kind of periodic nano-photonics system comprising attenuation in all its manifestations. Moreover, the description of amplified modes is covered by this framework, too, so that it can be adopted to the emerging item of MM research which is attributed to loss compensation by integrating active materials. Here, the Bloch modal concept evidently appears to be appropriate since the evaluation of the eigenmodes and their dispersion relation fundamentally allows to distinguish between the impact on pure bulk properties and those related to coupling at the interfaces.

Second, the presented research concentrated on explaining the propagation of light beams in MMs. This treatment can be straightforwardly extended to pulse propagation or spatio-temporal propagation effects in general. Thus, effects like group velocity dispersion can be thoroughly investigated for realistic MMs or even plasmonic nano-structures and there might be new and yet unseen conclusions which exert influence even on the field of nonlinear optics, e.g. solitary wave propagation.

Third, the presented super-cell approach which was used to tailor the angular dispersion relation of a fishnet MM is basically very general. It might be applied to other MM geometries, too. Moreover and even more interesting, it may also be used to tailor the response of MMs with respect to completely different functionalities. One similar example, e.g., is presented in Ref. [26] where a multi-element MM was used to mimic a perfect black body emitter.

Last but not least, the rich field of nonlinear optics in combination with plasmonic nano-structures and MMs still finds itself in an initial stage. On the one hand, there are still open questions concerning the fundamental origin of optical nonlinearities in metals [TP12, 196, 204, 205]. On the other hand, most contemporary practical investigations concentrate on higher-harmonic generation, but there is an urgent need to go beyond these scenarios. One example are three-wave mixing processes, i.e. sum- and difference frequency generation, which appears to be an alternative route for loss-compensation in MMs or any kind of functional metallic nano-structure [18]. The presented Fourier modal method in Chap. 5 can be straightforwardly adapted to this kind of scenario such that it might be a useful tool when such worthwhile processes have to be analyzed.

Acknowledgements

Now, retrospectively the writing of this thesis and by working on the current lines, I realize that this work in its final version would never exist without a lot of direct and indirect support and assistance from other persons. Most of all I would like to thank Prof. Dr. Falk Lederer and Prof. Dr. Carsten Rockstuhl for kindly housing me as a PhD student at the Institute of Condensed Matter Theory and Solid State Optics at the Friedrich-Schiller-Universität Jena.

Especially I want to thank Prof. Dr. Carsten Rockstuhl who has "affiliated" me and became my supervisor after an initial period of orientation and self-discovery. I notably appreciate the "free-space" you provided me during all these years without letting me lose the way in the broad expanse of the physical and, maybe even more important, the numerical universe. Every time you had an open mind for all of my concerns; sometimes even ideas. Special thanks for your persistence with respect to my manuscripts, especially the earlier ones.

I would like to thank all members of the Photonics group for their presence and support. I would like to thank Christoph Menzel for the fruitful and also the less fruitful discussions that led to so many collaborations. I enjoyed our business trips very much, except the parts with the rental cars. I would like to thank Stephan Fahr for his perpetual nagging about my sparse programming codes and for introducing me into the magic world of POV-Ray. To tell the truth, I never had understood it really. I would like to thank Stefan Mühlig, too. Actually, we only had a small intersection in our topics, however, it was a nice time. Thank you guys for the cake, the beer, the sausages and the discussions about our employment deficits. Last but not least, I have to thank Dr. Lutz Leine for his involved "administration" and his support with respect to the computational infrastructure. Thank you for letting me run my MATLAB code. I know it was hard for you.

I also appreciate the meta-meetings – a regular brainstorming with the group of T. Pertsch. To tell the truth, sometimes they were exciting, sometimes boring. Thank you for sharing your ideas and familiarizing me with the experimentalists perspective.

Many thanks also to W. Śmigaj and P. Lalanne (Institut d'Optique, Paris, France) and to T. Utikal from the group of H. Giessen (Uni Stuttgart, Germany) for the nice and fruitful collaboration.

I gratefully acknowledge the careful reading and evaluation of this thesis by all referees.

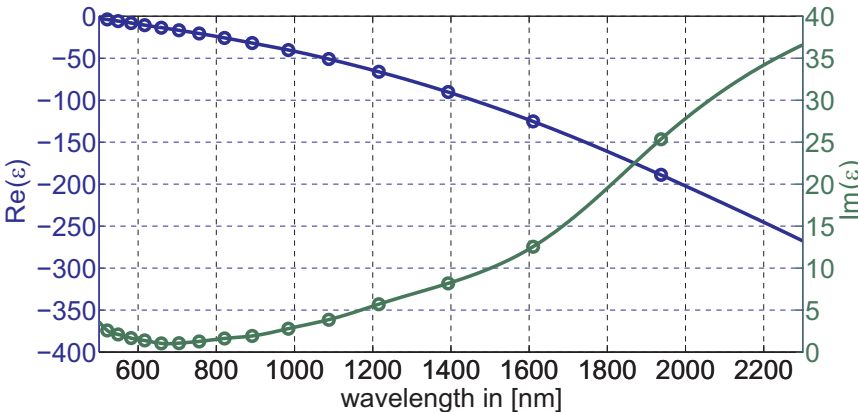
Last but not least, I thank all my family, especially Sylvia and my daughter Elisa, and all my friends that supported me during the last years. Thanks for the "sideline and amusement" irrespective of the hard work.

Material parameters

Material M.1: Frequency dispersion of the permittivity of silver according to a Drude formula. The frequency has to be inserted in rad/s. The constants are [150]: $\omega_p = 1.37 \times 10^{16}$ rad/s, $\gamma = 8.5 \times 10^{13}$ rad/s.

$$\epsilon = 1 - \frac{\omega_p^2}{\omega^2 + i\gamma\omega}$$

Material M.2: Wavelength dispersion of the permittivity of gold according to Ref. [206]. The symbols correspond to tabulated values.



Material M.3: Frequency and temperature (T) dispersion of the permittivity of lithium niobate according to Ref. [207]. The wavelength has to be inserted in [μm] and the temperature in [$^{\circ}\text{C}$]. The temperature is assumed to be 25°C throughout all performed simulations. The constants are: $B_1 = 0.1173 \mu\text{m}^2$, $C_1 = 1.65 \times 10^{-8} \mu\text{m}^2/\text{C}^2$, $D_1 = 0.212 \mu\text{m}$, $E_1 = 2.7 \times 10^{-8} \mu\text{m}/\text{C}^2$, $F_1 = 2.78 \times 10^{-2} \mu\text{m}^{-2}$; $B_2 = 0.097 \mu\text{m}^2$, $C_2 = 2.70 \times 10^{-8} \mu\text{m}^2/\text{C}^2$, $D_2 = 0.201 \mu\text{m}$, $E_2 = 5.4 \times 10^{-8} \mu\text{m}/\text{C}^2$, $F_2 = 2.24 \times 10^{-2} \mu\text{m}^{-2}$, $G_2 = 2.605 \times 10^{-7} \text{C}^{-2}$.

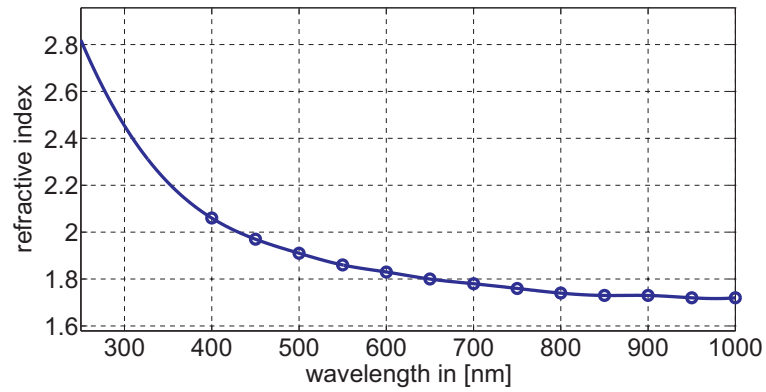
$$\epsilon_o = 4.9130 + \frac{B_1 + C_1 T^2}{\lambda^2 - (D_1 + E_1 T^2)^2} - F_1 \lambda^2; \quad \lambda = 2\pi c_0/\omega$$

$$\epsilon_{\text{ex}} = 4.5567 + \frac{B_2 + C_2 T^2}{\lambda^2 - (D_2 + E_2 T^2)^2} - F_2 \lambda^2 + G_2 T^2$$

Material M.4: Frequency dispersion of the permittivity of fused silica. The wavelength has to be inserted in [μm]. The constants are: $B_1 = 6.96166300 \times 10^{-1}$, $B_2 = 4.07942600 \times 10^{-1}$, $B_3 = 8.97479400 \times 10^{-1}$, $C_1 = 4.67914826 \times 10^{-3} \mu\text{m}^2$, $C_2 = 1.35120631 \times 10^{-2} \mu\text{m}^2$, $C_3 = 9.79340025 \times 10^{+1} \mu\text{m}^2$.

$$\epsilon = 1 + \frac{B_1 \lambda^2}{\lambda^2 - C_1} + \frac{B_2 \lambda^2}{\lambda^2 - C_2} + \frac{B_3 \lambda^2}{\lambda^2 - C_3}; \quad \lambda = 2\pi c_0/\omega$$

Material M.5: Wavelength dispersion of the refractive index of indium tin oxide. The symbols correspond to tabulated/measured values.



Material M.6: Frequency dispersion of the permittivity of gold according to a Drude formula. The frequency has to be inserted in rad/s. The constants are: $\omega_p = 1.137 \times 10^{16}$ rad/s, $\gamma = 3 \times 1.8838 \times 10^{14}$ rad/s.

$$\epsilon = 1 - \frac{\omega_p^2}{\omega^2 + i\gamma\omega}$$

Zusammenfassung

Die vorliegende Arbeit beschäftigt sich mit der Beschreibung und Charakterisierung der Ausbreitung (Propagation und Streuung) von Licht innerhalb von optischen, periodischen Metamaterialien sowie an deren Grenzflächen. Metamaterialien sind künstlich generierte Medien, wobei die charakteristische Größe der zugrundeliegenden Bausteine im Subwellenlängenbereich liegt. Die Beschreibung der Wechselwirkung von Metamaterialien mit Licht erfolgt im Rahmen dieser Arbeit streng rigoros – die Basis der Beschreibung stellen die Blochmoden des unendlich ausgedehnten, periodischen, strukturierten Mediums dar. Dazu wird in Kapitel 2 die sog. Fourier-Modal-Methode vorgestellt, die zur numerischen Berechnung der Blochmoden herangezogen werden kann. Kapitel 3 beschäftigt sich mit den Eigenschaften dieser Moden. Hier werden z.B. Orthogonalitätsrelationen abgeleitet, es wird die Bedeutung der Dispersionsrelation besprochen und welche Aussagen dieser zur Beschreibung von Beugung und Brechung von Lichtbündeln zu entnehmen sind. Des Weiteren werden geschlossene Ausdrücke für die Reflexions- und Transmissionskoeffizienten an einer Grenzfläche zwischen zwei Metamaterialien abgeleitet. Diese können als Verallgemeinerung der Fresnel'schen Koeffizienten an einer ebenen Grenzfläche zwischen zwei homogenen Materialien angesehen werden. Kapitel 4 widmet sich der Anwendung der in Kapitel 3 entwickelten, formalen Konzepte auf linkshändige Metamaterialien. Im Vordergrund steht hierbei die Beschreibung sog. Fishnet-Strukturen und deren Eigenschaften bezüglich der Ausbreitung von Lichtbündeln. Dabei kann im Rahmen dieser Arbeit gezeigt werden, dass eine negative Phasengeschwindigkeit weder ein notwendiges noch ein hinreichendes Kriterium ist, um negative Brechung bzw. anormale Beugung beobachten zu können. Dieser Umstand kann auf die Tatsache zurückgeführt werden, dass die behandelten Fishnetstrukturen nicht als effektives, lokales und homogenes Medium betrachtet werden können. Im weiteren Verlauf wird das Konzept für sog. Supercell-Fishnet-Strukturen vorgeschlagen und vorgestellt, welches ein gezieltes Design der optischen Eigenschaften von Metamaterialien erlaubt. Abschließend behandelt Kapitel 4 die Reflexion und Transmission an ebenen Grenzflächen. Hierbei wird hauptsächlich die Grenzfläche zwischen Luft und einem Swiss-Cross Metamaterial behandelt. Im Vordergrund steht die Untersuchung der gegenseitigen Kopplung zwischen verschiedenen Moden bzw. der Grenzfall, sodass nur noch die Grundmoden beider Medien

die Transmissions- und Reflexionseigenschaften bestimmen. Dabei hat sich die Swiss-Cross-Struktur als potentes Metamaterial erwiesen, welches einerseits ein linkshändiges Verhalten zeigt und dessen Eigenschaften ausschließlich auf Basis seiner Grundmode determiniert sind. Kapitel 5 widmet sich schließlich Themen der nichtlinearen Wechselwirkung zwischen Licht und Metamaterialien. Im Speziellen steht die Erzeugung von zweiter und dritter Harmonischer an metallischen Nanostrukturen im Vordergrund. Zu diesem Zweck wird im ersten Teil des Kapitels eine adaptierte und erweiterte Version der Fourier-Modal-Methode vorgestellt. Anschließend wird diese verwendet, um die nichtlineare Antwort zweier Beispielsysteme zu berechnen. Besondere Beachtung findet ein gekoppeltes System aus dielektrischem Wellenleiter sowie metallischer Nanodrähte an welchem die Erzeugung der dritten Harmonischen analysiert wird. Hierbei wird gezeigt werden, dass die spezifischen Charakteristika des nichtlinearen Fernfeldsignals Aufschluß über die eigentlichen Quellen der Nichtlinearität in der gekoppelten Nanostruktur geben können.

Ehrenwörtliche Erklärung

Hiermit erkläre ich ehrenwörtlich, dass ich die vorliegende Arbeit selbstständig, ohne unzulässige Hilfe Dritter und ohne Benutzung anderer als der angegebenen Hilfsmittel und Literatur angefertigt habe. Die aus anderen Quellen direkt oder indirekt übernommenen Daten und Konzepte sind unter Angabe der Quelle gekennzeichnet.

Weitere Personen waren an der inhaltlich-materiellen Erstellung der vorliegenden Arbeit nicht beteiligt. Insbesondere habe ich hierfür nicht die entgeltliche Hilfe von Vermittlungs- bzw. Beratungsdiensten (Promotionsberater oder andere Personen) in Anspruch genommen. Niemand hat von mir unmittelbar oder mittelbar geldwerte Leistungen für Arbeiten erhalten, die im Zusammenhang mit dem Inhalt der vorgelegten Dissertation stehen.

Die Arbeit wurde bisher weder im In- noch im Ausland in gleicher oder ähnlicher Form einer anderen Prüfungsbehörde vorgelegt.

Die geltende Promotionsordnung der Physikalisch-Astronomischen Fakultät ist mir bekannt.

Ich versichere ehrenwörtlich, dass ich nach bestem Wissen die reine Wahrheit gesagt und nichts verschwiegen habe.

Jena, May 15, 2012

Unterschrift

Publications

All publications in peer reviewed journals that are directly relevant for this thesis will appear in **bold** letters in the following.

Contribution to book chapters

1. C. Rockstuhl, **T. Paul**, T. Pertsch, and F. Lederer, "Computational Photonics - Grid Computing in der Nanooptik" in *Grid-Computing* pp. 367-384, D. Fey, ed. (Springer, Berlin-Heidelberg, 2010)

Peer reviewed journals

1. **T. Paul**, C. Menzel, W. Śmigaj, C. Rockstuhl, P. Lalanne, and F. Lederer, "Reflection and transmission of light at periodic layered metamaterial films," *Phys. Rev. B* 84, 115142 (2011)
2. T. Utikal, T. Zentgraf, **T. Paul**, C. Rockstuhl, F. Lederer, M. Lippitz, and H. Giessen, "Towards the Origin of the Nonlinear Response in Hybrid Plasmonic Systems," *Phys. Rev. Lett.* 106, 133901 (2011)
3. **T. Paul**, C. Rockstuhl, and F. Lederer, "Integrating Cold Plasma Equations into the Fourier Modal Method to Analyze Second Harmonic Generation at Metallic Nanostructures," *Journ. Mod. Opt.* 58, 438 (2011)
4. W. Śmigaj , P. Lalanne, J. Yang , **T. Paul** , C. Rockstuhl , F. Lederer, "Closed-form expression for the scattering coefficients at an interface between two periodic media," *Appl. Phys. Lett.* 98, 111107 (2011)
5. J. Yang, C. Sauvan, **T. Paul**, C. Rockstuhl, F. Lederer, and P. Lalanne, "Retrieving the effective parameters of metamaterials from single interface scattering problems," *Appl. Phys. Lett.* 97, 061102 (2010)

6. J. Petschulat, A. Chipouline, A. Tünnermann, T. Pertsch, C. Menzel, C. Rockstuhl, T. Paul, and F. Lederer, "A simple and versatile analytical approach for planar metamaterials," *Phys. Rev. B* **82**, 075102 (2010)
7. T. Paul, C. Menzel, C. Rockstuhl, and F. Lederer, "Advanced Optical Metamaterials," *Advanced Materials* **22**, 2354-2357 (2010)
8. T. Paul, C. Rockstuhl, and F. Lederer, "A numerical approach for analyzing higher harmonics generation in multilayer nanostructures," *J. Opt. Soc. Am. B* **27**, 1118-1130 (2010)
9. C. Menzel, T. Paul, C. Rockstuhl, T. Pertsch, S. Tretyakov, and F. Lederer, "Validity of effective material parameters for optical fishnet metamaterials," *Phys. Rev. B* **81**, 035320 (2010)
10. T. Paul, C. Rockstuhl, C. Menzel, and F. Lederer, "Anomalous refraction, diffraction and imaging in metamaterials," *Phys. Rev. B* **79**, 115430 (2009)
11. C. Rockstuhl, C. Menzel, T. Paul, and F. Lederer, "Optical activity in chiral media composed of three-dimensional metallic meta-atoms," *Phys. Rev. B* **79**, 035321 (2009)
12. C. Menzel, C. Rockstuhl, T. Paul, and F. Lederer, "Retrieving effective parameters for quasi-planar chiral metamaterials," *Appl. Phys. Lett.* **93**, 233106 (2008)
13. C. Rockstuhl, C. Menzel, T. Paul, T. Pertsch, and F. Lederer, "Light propagation in a fishnet metamaterial," *Phys. Rev. B* **78**, 155102 (2008).
14. C. Menzel, C. Rockstuhl, T. Paul, T. Pertsch, and F. Lederer, "Retrieving effective parameters for metamaterials at oblique incidence," *Phys. Rev. B* **77**, 195328 (2008)
15. T. Paul, C. Rockstuhl, C. Menzel, and F. Lederer, "Resonant Goos-Hänchen and Imbert-Fedorov shift at photonic crystal slabs," *Phys. Rev. A* **77**, 053802 (2008)
16. C. Rockstuhl, T. Paul, T. Zentgraf, T. P. Meyrath, T. Pertsch, H. Giessen, and F. Lederer, "Transition from thin-film to bulk properties of metamaterials," *Phys. Rev. B* **77**, 035126 (2008)
17. C. Menzel, C. Rockstuhl, T. Paul, S. Fahr and F. Lederer, "The Imbert-Fedorov-Shift at metamaterial interfaces," *Phys. Rev. A* **77**, 013810 (2008)

Conference Papers

1. T. Kaiser, C. Helgert, T. Paul, S. Bin Hasan, F. Lederer, C. Rockstuhl, and T. Pertsch, "Resonant coupling of dielectric waveguides with plasmonic metaatoms", SPIE, **Vol. 8093**, 809322, (2011)
2. C. Rockstuhl, C. Etrich, C. Helgert, C. Menzel, T. Paul, S. Fahr, T. Pertsch, J. Dorfmueller, R. Esteban, W. Khunsin, R. Vogelgesang, K. Kern, A. Dmitriev, K. Bittkau, T. Beckers, R. Carius and F. Lederer, "Large scale simulations in the realm of nanooptics", SPIE, **Vol. 7604**, 7604D, (2010)
3. J. Petschulat, A. Chipouline, E. Pshenay-Severin, A. Tünnermann, T. Pertsch, C. Menzel, C. Rockstuhl, T. Paul, and F. Lederer, "Analytical Modelling of linear and nonlinear properties of metamaterials based on multipole expansion", SPIE, **Vol. 7353**, 7353D, (2009)
4. C. Rockstuhl, C. Menzel, T. Paul, C. Helgert, E. Pshenay-Severin, J. Petschulat, A. Chipouline, T. Pertsch, and F. Lederer, "Bulk properties of metamaterials", SPIE, **Vol. 6987**, 69871O, (2008)

Keynote Talks

1. F. Lederer, C. Rockstuhl, C. Menzel, and T. Paul, and T. Pertsch, "On the dispersion relation and refractive index of optical metamaterials - from thin film to bulk ", **International Conference on Computational & Experimental Engineering and Sciences 2008**, Honolulu, Hawaii, USA

Invited Talks

1. C. Rockstuhl, T. Paul, S. Bin Hasan, C. Menzel, T. Kaiser, W. Smigaj, T. Pertsch, P. Lalanne, and F. Lederer, "The impedance of metamaterials and nanoplasmonic structures", **Metamaterials' 2011**, Barcelona, Spain
2. C. Rockstuhl, C. Menzel, T. Paul F. Lederer, E. Pshenay-Severin, M. Falkner, C. Helgert, A. Chipouline, W. Śmigaj, J. Yang, and P. Lalanne, "Effective properties of metamaterials " **SPIE Optics + Photonics 2011**, San Diego, USA

3. C. Rockstuhl, C. Menzel, T. Paul, A. Andryieuski, R. Malureanu, A. Lavrinenko and F. Lederer, "Isotropic optical metamaterials", **Metamaterials' 2010**, Karlsruhe, Germany
4. C. Rockstuhl, C. Menzel, T. Paul, A. Andryieuski, R. Malureanu, A. Lavrinenko and F. Lederer, "Isotropic optical metamaterials", **MediNano 2010**, Belgrade, Serbia
5. F. Lederer, T. Paul, C. Rockstuhl, and C. Menzel, "Light Propagation in Optical Metamaterials", **CIMTEC 2010**, Montecatini Terme, Italy
6. C. Rockstuhl, C. Menzel, T. Paul, S. Fahr, F. Lederer, C. Etrich, C. Helgert and T. Pertsch, "Large scale simulations in the realm of nanooptics", **SPIE Photonics West 2010**, San Francisco, USA
7. F. Lederer, C. Rockstuhl, C. Menzel, and T. Paul, "The dispersion relation in metamaterials - from thin film to bulk", **Metamaterials' 2008**, Pamplona, Spain
8. C. Rockstuhl, C. Menzel, T. Paul, J. Petschulat, E. Pshenay-Severin, C. Helgert, A. Chipouline, T. Pertsch, and F. Lederer "Properties of bulk metamaterials", **SPIE Photonics Europe 2008**, Strasbourg, France

Conference contributions

1. P. Lalanne, W. Śmigaj, J. Yang, T. Paul, C. Rockstuhl, and F. Lederer, "Treating the scattering problem at the interface between two metamaterials", **Metamaterials' 2011**, Barcelona, Spain
2. S. Mühlig, C. Menzel, T. Paul, C. Rockstuhl, and F. Lederer, "Cloaking dielectric spheres by a shell of metallic nanoparticles", **Metamaterials' 2011**, Barcelona, Spain
3. T. Kaiser, C. Helgert, T. Paul, S. Bin Hasan, F. Lederer, C. Rockstuhl, and T. Pertsch, "Resonant coupling of dielectric waveguides with plasmonic metaatoms" **SPIE Optics + Photonics 2011**, San Diego, USA
4. W. Śmigaj, P. Lalanne, J. Yang, T. Paul, C. Rockstuhl, and F. Lederer, "Calcul approximatif des coefficients de transmission et réflexion aux interfaces entre milieux périodiques", **Colloque National Métamatériaux 2011**, Orsay, France
5. T. Kaiser, C. Helgert, T. Paul, R. Wolf, C. Rockstuhl, F. Lederer, and T. Pertsch, "Metamaterials in Waveguide Geometries", **CLEO Europe 2011 Munich**, Germany

6. T. Utikal, T. Zentgraf, T. Paul, C. Rockstuhl, F. Lederer, M. Lippitz, and H. Giessen, "Towards the Origin of Optical Nonlinearities in Hybrid Plasmonic Systems", Nanometa 2011, Seefeld, Austria
7. T. Paul, C. Rockstuhl, F. Lederer, and P. Lalanne, "The Impedance of Metamaterials", Nanometa 2011, Seefeld, Austria
8. T. Paul, C. Rockstuhl, and F. Lederer, "A Bloch Mode Picture for Understanding Nonlinear Metamaterials", Nanometa 2011, Seefeld, Austria
9. S.B. Hasan, J. Reinhold, T. Paul, C. Helgert, A. Chipouline, C. Rockstuhl, T. Pertsch, "Intrinsic and Extrinsic Nonlinearities of Nanooptical Systems", Ultrafast Nano Optics 2 2010, Bad Dürkheim, Germany
10. J. Petschulat, A. Chipouline, C. Menzel, T. Paul, C. Rockstuhl, A. Tünnermann, F. Lederer, and T. Pertsch, "Assembling metamaterials - A building block approach for conductively or near-field coupled plasmonic entities", Metamaterials' 2010, Karlsruhe, Germany
11. J. Yang, C. Sauvan, P. Lalanne, T. Paul, C. Rockstuhl and F. Lederer, "Single interface between a bulk metamaterial and a homogeneous half space", Metamaterials' 2010, Karlsruhe, Germany
12. C. Menzel, T. Paul, C. Rockstuhl, R. Iliw, A. Andryieuski, R. Malureanu, A. V. Lavrinenko, and F. Lederer, "Optical Isotropic Negative Index Metamaterials", META 2010 Tucson, Arizona, USA
13. C. Menzel, C. Rockstuhl, T. Paul, C. Helgert, J. Petschulat, E.-B. Kley, F. Eilenberger, T. Pertsch, and F. Lederer, "Asymmetric Transmission of Linearly Polarized Light through Low Symmetry Metamaterials", CLEO/QELS 2010 San Jose, California, USA
14. S. Fahr, T. Paul, S. Mühlig, C. Rockstuhl, and F. Lederer, "Absorption enhancement in thin film solar cells by nanophotonic structures", PhoNa International Workshop 2010, Jena, Germany
15. C. Menzel, C. Rockstuhl, S. Mühlig, T. Paul, and F. Lederer, "Chirality as a bulk property retrieved from the dispersion relation", PhoNa International Workshop 2010, Jena, Germany
16. J. Reinhold, T. Paul, C. Helgert, J. Petschulat, C. Rockstuhl, E.-B. Kley, F. Lederer, and T. Pertsch, "Enhancing nonlinear effects in lithium niobate exploiting plasmonic

- resonances in metallic nanostructures”, PhoNa International Workshop 2010, Jena, Germany
17. T. Paul, S. Bin Hasan, C. Rockstuhl and F. Lederer, ”Enhanced second and third harmonic generation using plasmonic metamaterials”, PhoNa International Workshop 2010, Jena, Germany
 18. T. Paul, C. Menzel, S. Fahr, S. Mühlig, C. Rockstuhl, and F. Lederer, ”Anomalous diffraction and refraction in negative-index metamaterials”, PhoNa International Workshop 2010, Jena, Germany
 19. T. Paul, C. Menzel, C. Rockstuhl, S. Bin Hasan, and F. Lederer, ”Enhancing higher harmonics generation using plasmonic nanostructures”, 74. Annual Meeting of the Deutsche Physikalische Gesellschaft 2010, Regensburg, Germany
 20. C. Rockstuhl, C. Menzel, T. Paul, T. Pertsch, S. Tretyakov, and F. Lederer, ”How feasible are effective material parameters for metamaterials?”, META 10 2010, Cairo, Egypt
 21. J. Petschulat, A. Chipouline, A. Tünnermann, T. Pertsch, C. Menzel, C. Rockstuhl, T. Paul, and F. Lederer, ”Multipole Metamaterials: A Mesoscopic Investigation towards Effective Linear and Nonlinear Optical Material Interaction”, Frontiers in Optics 2009, San Jose, California
 22. T. Paul, C. Menzel, C. Rockstuhl, and F. Lederer, ”Isotropic optical metamaterials”, Metamaterials’ 2009, London, UK
 23. C. Rockstuhl, C. Menzel, T. Paul, and F. Lederer, ”Chirality as a bulk property retrieved from the dispersion relation”, CLEO Europe 2009 Munich, Germany
 24. T. Paul, M. Geiselmann, T. Utikal, T. Zentgraf, H. Giessen, C. Rockstuhl, and F. Lederer, ”Enhanced Third Harmonic Generation Using Plasmonic Metamaterials”, CLEO Europe 2009 Munich, Germany
 25. C. Menzel, C. Rockstuhl, T. Paul, T. Pertsch, and F. Lederer, ”Effective Parameters For Anisotropic Metamaterials”, CLEO/QELS 2009 Baltimore, Maryland, USA
 26. C. Rockstuhl, S. Fahr, T. Paul, C. Menzel, F. Lederer, K. Bittkau, T. Beckers, and R. Carius ”Photon Management in Thin Film Solar Cells”, CLEO/QELS 2009 Baltimore, Maryland, USA

27. S. Fahr, C. Menzel, T. Paul, C. Rockstuhl, and F. Lederer, "Periodic arrays of metallic nanoparticles as efficient intermediate reflectors in aSi:H- μ cSi solar cells", OWTNM 2009, Jena, Germany
28. T. Paul, C. Menzel, S. Fahr, C. Rockstuhl, and F. Lederer, "Adapted Fourier modal method for the analysis of higher harmonic generation in arbitrary bi-periodic multi-layer structures", OWTNM 2009, Jena, Germany
29. C. Menzel, T. Paul, C. Rockstuhl and F. Lederer, "Retrieving Effective Parameters of Anisotropic Metamaterials", OWTNM 2009, Jena, Germany
30. A. Chipouline, J. Petschulat, E. Pshenay-Severin, A. Tünnermann, T. Pertsch, C. Menzel, C. Rockstuhl, T. Paul, and F. Lederer, "Analytical modelling of linear and nonlinear properties of metamaterials based on multipole expansion", SPIE Photonics Europe 2009, Prague, Czech Republic
31. F. Lederer, C. Rockstuhl, R. Singh, C. Menzel, T. Paul, and W. Zhang, "Resonances in THz Metamaterials and Nanoantennas", PECS VIII 2009, Sydney, Australia
32. C. Rockstuhl, C. Menzel, T. Paul, F. Lederer, R. Singh and W. Zhang, "Resonances of Coupled Split-Ring-Resonators with Broken Symmetry", Nanometa 2009, Seefeld, Austria
33. C. Rockstuhl, C. Menzel, T. Paul, F. Lederer, J. Petschulat, C. Helgert, E. Pshenay-Severin, A. Chipouline, and T. Pertsch, "Three Dimensional Chiral Meta-Atoms", Nanometa 2009, Seefeld, Austria
34. J. Petschulat, A. Chipouline, E. Pshenay-Severin, A. Tünnermann, T. Pertsch, C. Menzel, C. Rockstuhl, T. Paul, and F. Lederer, "Linear and Nonlinear Properties of Metamaterials: Analytical Modelling Based on Multipole Expansion", Nanometa 2009, Seefeld, Austria
35. C. Menzel, C. Rockstuhl, T. Paul, and F. Lederer, "On the reliability of effective parameters for anisotropic metamaterials", Nanometa 2009, Seefeld, Austria
36. T. Paul, C. Rockstuhl, C. Menzel, and F. Lederer, "Anomalous diffraction and refraction in negative-index metamaterials", Nanometa 2009, Seefeld, Austria
37. T. Paul, C. Rockstuhl, C. Menzel, and F. Lederer, "Anomalous Diffraction and Imaging Properties of Metamaterials", OSA topical meeting 2008: Photonic Metamaterials: From Random to Periodic, Rochester, USA

38. T. Paul, C. Helgert, J. Reinhold, E.B. Kley, J. Petschulat, T. Pertsch, C. Rockstuhl, and F. Lederer "Enhancing nonlinear effects in lithium niobate exploiting plasmonic resonances in metallic nanostructures", 416. WE-Heraeus-Seminar on Ultrafast Nanooptics 2008, Bad Honnef, Germany
39. C. Menzel, C. Rockstuhl, T. Paul and F. Lederer "Quantifying Chirality of Metamaterials", Metamaterials' 2008, Pamplona, Spain
40. C. Menzel, T. Paul, C. Rockstuhl, T. Pertsch, and F. Lederer, "Angle-Dependent Effective Properties of Metamaterials - Material vs. Wave Parameters", CLEO/QELS 2008 San Jose, California, USA
41. T. Paul, C. Rockstuhl, C. Menzel, and F. Lederer, "The Imbert-Fedorov and Goos-Hänchen shift at metamaterial interfaces", CLEO/QELS 2008 San Jose, California, USA
42. C. Rockstuhl, T. Paul, C. Menzel, T. Pertsch, and F. Lederer, "Dispersion Relation of Light in Metamaterials", CLEO/QELS 2008 San Jose, California, USA
43. C. Rockstuhl, C. Menzel, T. Paul, T. Pertsch, and F. Lederer, "On the dispersion relation of light in metamaterials", 72. Annual Meeting of the Deutsche Physikalische Gesellschaft 2008, Berlin, Germany
44. T. Paul, C. Menzel, C. Rockstuhl, and F. Lederer, "The Goos-Hänchen and Imbert-Fedorov shift at metamaterial interfaces", 72. Annual Meeting of the Deutsche Physikalische Gesellschaft 2008, Berlin, Germany
45. C. Menzel, T. Paul, C. Rockstuhl, T. Pertsch, and F. Lederer, "Retrieving angle dependent effective parameters of metamaterials", 72. Annual Meeting of the Deutsche Physikalische Gesellschaft 2008, Berlin, Germany

Bibliography

- [1] E.-H. Schmitz, "Handbuch zur Geschichte der Optik, Band 1: Von der Antike bis Newton" (Wayenborgh, Bonn [u.a.], 1981)
- [2] Abū 'Alī al-Ḥasan Ibn-al-Ḥasan Ibn-al-Haiṭam (†1035), "The optics of Ibn al-Haytham: books I-III "On direct vision": part 1&2," A. I. Sabra, ed. (Studies of the Warburg Institute; 40,1&2, London, 1989)
- [3] J.B. Pendry, "Negative Refraction Makes a Perfect Lens," *Phys. Rev. Lett.* **85**, 3966-3969 (2000)
- [4] V. Veselago, "The electrodynamics of substances with simultaneously negative values of ϵ and μ ," *Sov. Phys. Usp.* **10**, 509-514 (1968)
- [5] J.B. Pendry, D. Schurig, and D.R. Smith, "Controlling Electromagnetic Fields," *Science* **312**, 1780-1782 (2006)
- [6] U. Leonhardt, "Optical Conformal Mapping," *Science* **312**, 1777-1780 (2006)
- [7] U. Leonhardt, and T. G. Philbin, "Transformation Optics and the Geometry of Light," *Prog. Opt.* **53**, 69-152 (2009).
- [8] H. Chen, C. T. Chan, and P. Sheng, "Transformation optics and metamaterials," *Nat. Mat.* **9**, 387-396 (2010).
- [9] J. Valentine, J. Li, T. Zentgraf, G. Bartal, and X. Zhang, "An optical cloak made of dielectrics," *Nat. Mat.* **8**, 568-571 (2009).
- [10] Y. Lai, H. Chen, Z.-Q. Zhang, and C. T. Chan, "Complementary Media Invisibility Cloak that Cloaks Objects at a Distance Outside the Cloaking Shell," *Phys. Rev. Lett.* **102**, 093901 (2009)
- [11] T. Ergin, N. Stenger, P. Brenner, J. B. Pendry, M. Wegener, "Three-Dimensional Invisibility Cloak at Optical Wavelengths," *Science* **328**, 337-339 (2010).

- [12] Y. Lai, J. Ng, H. Chen, D. Han, J. Xiao, Z.-Q. Zhang, and C. T. Chan, "Illusion Optics: The Optical Transformation of an Object into Another Object," *Phys. Rev. Lett.* **102**, 253902 (2009)
- [13] K. Wu, and G. P. Wang, "Hiding objects and creating illusions above a carpet filter using a Fourier optics approach," *Opt. Expr.* **18**, 19894-19901 (2010)
- [14] C. Li, X. Meng, X. Liu, F. Li, G. Fang, H. Chen, and C. T. Chan, "Experimental Realization of a Circuit-Based Broadband Illusion-Optics Analogue," *Phys. Rev. Lett.* **105**, 233906 (2010)
- [15] W. X. Jiang, H. F. Ma, Q. Cheng, and T. J. Cui, "Illusion media: Generating virtual objects using realizable metamaterials," *Appl. Phys. Lett.* **96**, 121910 (2010)
- [16] W. X. Jiang, H. F. Ma, Q. Cheng, and T. J. Cui, "Virtual conversion from metal object to dielectric object using metamaterials," *Opt. Expr.* **18**, 11276-11281 (2010)
- [17] I. V. Shadrivov, A. A. Zharov, and Y. S. Kivshar, "Second-harmonic generation in nonlinear left-handed metamaterials," *J. Opt. Soc. Am. B* **23**, 529-534 (2006)
- [18] A. K. Popov, and V. M. Shalaev, "Compensating losses in negative-index metamaterials by optical parametric amplification," *Opt. Lett.* **31**, 2169-2171 (2006)
- [19] A. K. Popov, and V. M. Shalaev, "Negative-index metamaterials: second-harmonic generation, ManleyRowe relations and parametric amplification," *Appl. Phys. B* **84**, 131-137 (2006)
- [20] N. Lazarides, and G. P. Tsironis, "Coupled nonlinear Schrödinger field equations for electromagnetic wave propagation in nonlinear left-handed materials," *Phys. Rev. E* **71**, 036614 (2005)
- [21] K. Sakoda, "Optical properties of photonic crystals" (Springer, Berlin [u.a.], 2001)
- [22] J. D. Joannopoulos, "Molding the flow of light," 2nd ed. (Princeton Univ. Press, Princeton, NJ [u.a.], 2008)
- [23] Z. Jacob, L. V. Alekseyev, and E. Narimanov, "Optical Hyperlens: Far-field imaging beyond the diffraction limit," *Opt. Expr.* **14**, 8247-8256 (2006)
- [24] Z. Liu, H. Lee, Y. Xiong, C. Sun, and X. Zhang, "Far-Field Optical Hyperlens Magnifying Sub-Diffraction-Limited Objects," *Science* **315**, 1686 (2007).

- [25] N. I. Landy, S. Sajuyigbe, J. J. Mock, D. R. Smith, and W. J. Padilla, "Perfect Metamaterial Absorber," *Phys. Rev. Lett.* **100**, 207402 (2008).
- [26] X. Liu, T. Tyler, T. Starr, A. F. Starr, N. M. Jokerst, and W. J. Padilla, "Taming the Blackbody with Infrared Metamaterials as Selective Thermal Emitters," *Phys. Rev. Lett.* **107**, 045901 (2011)
- [27] G. Dolling, M. W. Klein, M. Wegener, A. Schädle, B. Kettner, S. Burger, and S. Linden, "Negative beam displacements from negative-index photonic metamaterials," *oe***15**, 14219-14227 (2007)
- [28] J. Valentine, S. Zhang, T. Zentgraf, E. Ulin-Avila, D. A. Genov, G. Bartal, X. Zhang, "Three-dimensional optical metamaterial with a negative refractive index," *Nature* **455**, 376-379 (2008)
- [29] G. Dolling, C. Enkrich, M. Wegener, C. M. Soukoulis, and S. Linden, "Simultaneous Negative Phase and Group Velocity of Light in a Metamaterial," *Science* **312**, 892-894 (2006).
- [30] K. Aydin, I. Bulu, and E. Ozbay, "Subwavelength resolution with a negative-index metamaterial superlens," *Appl. Phys. Lett.* **90**, 254102 (2007)
- [31] N. Fang, H. Lee, C. Sun, and X. Zhang, "SubDiffraction-Limited Optical Imaging with a Silver Superlens," *Science* **308**, 534-537 (2005)
- [32] J. K. Gansel, M. Thiel, M. S. Rill, M. Decker, K. Bade, V. Saile, G. v. Freymann, S. Linden, and M. Wegener, "Gold helix photonic metamaterial as broadband circular polarizer," *Science* **325**, 1513-1515 (2009).
- [TP00] C. Rockstuhl, C. Menzel, T. Paul, and F. Lederer, "Optical activity in chiral media composed of three-dimensional metallic meta-atoms," *Phys. Rev. B* **79**, 035321 (2009).
- [33] C. Menzel, C. Helgert, C. Rockstuhl, E.-B. Kley, A. Tünnermann, T. Pertsch, and F. Lederer, "Asymmetric Transmission of Linearly Polarized Light at Optical Metamaterials," *Phys. Rev. Lett.* **104**, 253902 (2010)
- [34] V. M. Agranovich, Y. R. Shen, R. H. Baughman, and A. A. Zakhidov, "Linear and nonlinear wave propagation in negative refraction metamaterials," *Phys. Rev. B* **69**, 165112 (2004)

- [35] V. M. Agranovich, and V. L. Ginzburg, "Crystal optics with spatial dispersion, and excitons," N. Weinstein, transl. (Springer, Berlin [u.a.], 1984)
- [36] M. A. McCord, and M. J. Rooks, "Electron Beam Lithography" in *Handbook of microlithography, micromachining, and microfabrication, Vol. 1*, P. Rai-Choudhury, ed. (SPIE Optical Engineering Press, Bellingham, Wash., 1997), pp. 139-250 [ISBN: 0-8194-2378-5]
- [37] J. Orloff, M. Utlaut, L. Swanson, "High resolution focused ion beams : FIB and its applications" (Kluwer Academic/Plenum, New York, NY, 2003) [ISBN: 0-306-47350-X]
- [38] J. A. Fan, C. Wu, K. Bao, J. Bao, R. Bardhan, N. J. Halas, V. N. Manoharan, P. Nordlander, G. Shvets, and F. Capasso, Self-Assembled Plasmonic Nanoparticle Clusters," *Science* **328**, 1135-1138 (2010)
- [39] D. A. Pawlak, S. Turczynski, M. Gajc, K. Kolodziejak, R. Diduszko, K. Rozniatowski, J. Smalc, and I. Vendik, "How Far Are We from Making Metamaterials by Self-Organization? The Microstructure of Highly Anisotropic Particles with an SRR-Like Geometry," *Advanced Functional Materials* **20**, 11161124 (2010)
- [40] B. Liu, X. Zhao, W. Zhu, W. Luo, and X. Cheng, "Multiple Pass-Band Optical Left-Handed Metamaterials Based on Random Dendritic Cells," *Advanced Functional Materials* **18**, 35233528 (2008)
- [41] B. Gong, and X. Zhao, "Numerical demonstration of a three-dimensional negative-index metamaterial at optical frequencies," *Opt. Express* **19**, 289-296 (2011)
- [42] A. R. Tao, D. P. Ceperley, P. Sinsersuksakul, A. R. Neureuther, and P. Yang, "Self-Organized Silver Nanoparticles for Three-Dimensional Plasmonic Crystals," *Nano Letters* **8**, 4033-4038 (2008)
- [43] K. Aydin, K. Guven, N. Katsarakis, C. Soukoulis, and E. Ozbay, "Effect of disorder on magnetic resonance band gap of split-ring resonator structures," *Opt. Express* **12**, 5896-5901 (2004)
- [44] M. V. Gorkunov, S. A. Gredeskul, I. V. Shadrivov, and Y. S. Kivshar, "Effect of microscopic disorder on magnetic properties of metamaterials," *Phys. Rev. E* **73**, 056605 (2006)

- [45] N. Papasimakis, V. A. Fedotov, Y. H. Fu, D. P. Tsai, and N. I. Zheludev, "Coherent and incoherent metamaterials and order-disorder transitions," *Phys. Rev. B* **80**, 041102 (2009)
- [46] C. Helgert, C. Rockstuhl, C. Etrich, C. Menzel, E.-B. Kley, A. Tnnermann, F. Lederer, and T. Pertsch, "Effective properties of amorphous metamaterials," *Phys. Rev. B* **79**, 233107 (2009)
- [47] C. Helgert, C. Rockstuhl, C. Etrich, E.-B. Kley, A. Tnnermann, F. Lederer, and T. Pertsch, "Effects of anisotropic disorder in an optical metamaterial," *Applied Physics A: Materials Science & Processing*, DOI: 10.1007/s00339-010-6190-2 (2010)
- [48] A. Taflove, S. Hagness, "Computational Electrodynamics: The Finite-Difference Time-Domain Method," 3rd edn. (Artech House, Boston, Mass. 2005) [ISBN: 978-1-580-53832-9]
- [49] Y. Hao; R. Mittra, "FDTD modeling of metamaterials : theory and applications" (Artech House, Boston, Mass. 2009) [ISBN: 1-596-93160-4]
- [50] J. P. A. Bastos, N. Sadowski, "Electromagnetic modeling by finite element methods" (Dekker: New York, NY, 2003) [ISBN: 0-8247-4269-9]
- [51] J. Jin, "The finite element method in electromagnetics," 2nd edn. (Wiley, New York, NY, 2002) [ISBN: 0-471-43818-9]
- [52] COMSOL Multiphysics GmbH: Papers & Presentations, <http://www.comsol.de/papers/> (online resource, visited at 05/03/2011)
- [53] J. Niegemann, M. König, K. Stannigel, and K. Busch, "Higher-order time-domain methods for the analysis of nano-photonic systems," *Photonics and Nanostructures - Fundamentals and Applications* **7**, 2-11 (2009)
- [54] K. Stannigel, M. König, J. Niegemann, and Kurt Busch, "Discontinuous Galerkin time-domain computations of metallic nanostructures," *Opt. Express* **17**, 14934-14947 (2009)
- [55] D. Maystre, and M. Neviere, "Electromagnetic theory of crossed gratings," *J. Optics* **9**, 301-306 (1978)
- [56] P. Vincent, "Differential Methods" in *Electromagnetic theory of gratings*, R. Petit, ed. (Springer, Berlin, 1980), pp. 101-121

- [57] E. Popov, and M. Neviere, "Differential theory for diffraction gratings: a new formulation for TM polarization with rapid convergence," *Opt. Lett.* **25**, 598-600 (2000)
- [58] E. Popov, and M. Neviere, "Grating theory: new equations in Fourier space leading to fast converging results for TM polarization," *J. Opt. Soc. Am. A* **17**, 1773-1784 (2000)
- [59] E. Popov, and M. Neviere, "Maxwell equations in Fourier space: fast-converging formulation for diffraction by arbitrary shaped, periodic, anisotropic media," *J. Opt. Soc. Am. A* **18**, 2886-2894 (2001)
- [60] D. Maystre, "Integral Methods" in *Electromagnetic theory of gratings*, R. Petit, ed. (Springer, Berlin, 1980), pp. 63-100
- [61] D. Maystre, "Rigorous vector theories in diffraction gratings" in *Progress in Optics*, Vol. **XXI**, E. Wolf, ed. (Elsevier, Amsterdam, 1984), pp. 1-67
- [62] Gunther Schmidt, and B. H. Kleemann, "Integral equation methods from grating theory to photonics: an overview and new approaches for conical diffraction," *J. Mod. Opt.* **58**, 407423 (2011)
- [63] J. Chandezon, G. Raoult, and D. Maystre, "A new theoretical method for diffraction gratings and its numerical application," *J. Optics* **11**, 235-241 (1980)
- [64] T. W. Preist, N. P. K. Cotter, and J. R. Sambles, "Periodic multilayer gratings of arbitrary shape," *J. Opt. Soc. Am. A* **12**, 1740-1748 (1995)
- [65] L. Li, G. Granet, J. P. Plumey, and J. Chandezon, "Some topics in extending the C method to multilayer gratings of different profiles," *Pure Appl. Opt.* **5**, 141-156 (1996)
- [66] T. Delort, and D. Maystre, "Finite-element method for gratings," *J. Opt. Soc. Am. A* **10**, 2592-2601 (1993)
- [67] K. Knop, "Rigorous diffraction theory for transmission phase gratings with deep rectangular grooves," *J. Opt. Soc. Am.* **68**, 1206-1210 (1978)
- [68] M. G. Moharam, and T. K. Gaylord, "Rigorous coupled-wave analysis of planar-grating diffraction," *J. Opt. Soc. Am. A* **71**, 811818 (1981)
- [69] E. Noponen, and J. Turunen, "Eigenmode method for electromagnetic synthesis of diffractive elements with three-dimensional profiles," *J. Opt. Soc. Am. A* **11**, 2494-2502 (1994)

- [70] N. P. K. Cotter, T. W. Preist, and J. R. Sambles, "Scattering-matrix approach to multilayer diffraction," *J. Opt. Soc. Am. A* **12** 1097-1103 (1995)
- [71] L. Li, "Formulation and comparison of two recursive matrix algorithms for modeling layered diffraction gratings," *J. Opt. Soc. Am. A* **13** 1024-1035 (1996)
- [72] L. Li, "Note on the S-matrix propagation algorithm," *J. Opt. Soc. Am. A* **20** 655-660 (2003)
- [73] P. Lalanne, and G. M. Morris, "Highly improved convergence of the coupled-wave method for TM polarization," *J. Opt. Soc. Am. A* **13**, 779-784 (1996)
- [74] L. Li, "Use of Fourier series in the analysis of discontinuous periodic structures," *J. Opt. Soc. Am. A* **13**, 1870-1876 (1996)
- [75] P. Lalanne, "Improved formulation of the coupled-wave method for two-dimensional gratings," *J. Opt. Soc. Am. A* **14**, 1592-1598 (1997)
- [76] L. Li, "New formulation of the Fourier modal method for crossed surface-relief gratings," *J. Opt. Soc. Am. A* **14**, 2758-2766 (1997)
- [77] T. Schuster, J. Ruoff, N. Kerwien, S. Rafler, and W. Osten, "Normal vector method for convergence improvement using the RCWA for crossed gratings," *J. Opt. Soc. Am. A* **24**, 2880-2890 (2007)
- [78] R. Antos, "Fourier factorization with complex polarization bases in modeling optics of discontinuous bi-periodic structures," *Opt. Expr.* **17**, 7269-7274 (2009)
- [79] G. Granet, "Reformulation of the lamellar grating problem through the concept of adaptive spatial resolution," *J. Opt. Soc. Am. A* **16**, 2510-2516 (1999)
- [80] G. Granet, and J.-P. Plumey, "Parametric formulation of the Fourier modal method for crossed surface-relief gratings," *J. Opt. A: Pure Appl. Opt.* **4** S145-S149 (2002)
- [81] T. Vallius, and M. Honkanen, "Reformulation of the Fourier modal method with adaptive spatial resolution: application to multilevel profiles," *Opt. Expr.* **10** 24-34 (2002)
- [82] T. Weiss, G. Granet, N. A. Gippius, S. G. Tikhodeev, and H. Giessen, "Matched coordinates and adaptive spatial resolution in the Fourier modal method," *Opt. Expr.* **17**, 8051-8061 (2009)

- [83] S. Essig, and K. Busch, "Generation of adaptive coordinates and their use in the Fourier Modal Method," *Opt. Expr.* **18**, 23258-23274 (2010)
- [84] E. Silberstein, P. Lalanne, J.-P. Hugonin, and Q. Cao, "Use of grating theories in integrated optics," *J. Opt. Soc. Am. A* **18**, 2865-2875 (2001)
- [85] P. Lalanne, "Electromagnetic analysis of photonic crystal waveguides operating above the light cone," *IEEE J. Quant. Elec.* **38**, 800-804 (2002)
- [86] Q. Cao, P. Lalanne, and J.-P. Hugonin, "Stable and efficient Bloch-mode computational method for one-dimensional grating waveguides," *J. Opt. Soc. Am. A* **19**, 335-338 (2002)
- [87] J.-P. Hugonin, and P. Lalanne, "Perfectly matched layers as nonlinear coordinate transforms: a generalized formulation," *J. Opt. Soc. Am. A* **22**, 1844-1849 (2005)
- [88] L. Li, "Fourier modal method for crossed anisotropic gratings with arbitrary permittivity and permeability tensors," *J. Opt. A: Pure Appl. Opt.* **5**, 345-355 (2003)
- [89] N. W. Ashcroft; and N. D. Mermin, "Solid state physics" (Brooks/Cole Thomson Learning, South Melbourne, 2008) [ISBN: 0-03-083993-9]
- [90] G. Lecamp, J. P. Hugonin, and P. Lalanne, "Theoretical and computational concepts for periodic optical waveguides," *Opt. Expr.* **15**, 11042-11057 (2007)
- [91] R. Biswas, Z. Y. Li, and K. M. Ho, "Impedance of photonic crystals and photonic crystal waveguides," *Appl. Phys. Lett.* **84**, 1254-1256 (2004)
- [92] B. Momeni, A. Asghar Eftekhari, and A. Adibi, "Effective impedance model for analysis of reflection at the interfaces of photonic crystals," *Opt. Lett.* **32**, 778-780 (2007)
- [93] B. Momeni, M. Badieirostami, and A. Adibi, "Accurate and efficient techniques for the analysis of reflection at the interfaces of three-dimensional photonic crystals," *J. Opt. Soc. Am. B* **24**, 2957-2963 (2007)
- [94] W. Śmigaj, and B. Gralak, "Validity of the effective-medium approximation of photonic crystals," *Phys. Rev. B* **77**, 235445 (2008)
- [TP01] J. Yang, C. Sauvan, T. Paul, C. Rockstuhl, F. Lederer, and P. Lalanne, "Retrieving the effective parameters of metamaterials from the single interface scattering problem," *Appl. Phys. Lett.* **97**, 061102 (2010)

- [95] L. C. Botten, T. P. White, A. A. Asatryan, T. N. Langtry, C. Martijn de Sterke, and R. C. McPhedran, "Bloch mode scattering matrix methods for modeling extended photonic crystal structures. I. Theory," *Phys. Rev. E* **70**, 056606 (2004)
- [96] T. P. White, L. C. Botten, C. Martijn de Sterke, R. C. McPhedran, A. A. Asatryan, and T. N. Langtry, "Bloch mode scattering matrix methods for modeling extended photonic crystal structures. II. Applications," *Phys. Rev. E* **70**, 056607 (2004)
- [97] F. J. Lawrence, L. C. Botten, K. B. Dossou, C. M. de Sterke, and R. C. McPhedran, "Impedance of square and triangular lattice photonic crystals," *Phys. Rev. A* **80**, 023826 (2009)
- [TP02] W. Śmigaj, P. Lalanne, J. Yang, T. Paul, C. Rockstuhl and F. Lederer, "Closed-form expression for the scattering coefficients at an interface between two periodic media," *Appl. Phys. Lett.* **98**, 111107 (2011)
- [98] B. Gralak, S. Enoch, and G. Tayeb, "From scattering or impedance matrices to Bloch modes of photonic crystals," *J. Opt. Soc. Am. A* **19**, 1547-1554 (2002)
- [99] Z.-Y. Li, and K.-M. Ho, "Application of structural symmetries in the plane-wave-based transfer-matrix method for three-dimensional photonic crystal waveguides," *Phys. Rev. B* **68**, 245117 (2003)
- [100] L. C. Botten, N. A. Nicorovici, R. C. McPhedran, C. Martijn de Sterke, and A. A. Asatryan, "Photonic band structure calculations using scattering matrices," *Phys. Rev. E* **64**, 046603 (2001)
- [101] K. Busch, G. von Freymann, S. Linden, S.F. Mingaleev, L. Tkeshelashvili, and M. Wegener, "Periodic nanostructures for photonics," *Phys. Rep.* **444**, 101-202 (2007)
- [TP03] T. Paul, W. Śmigaj, C. Menzel, C. Rockstuhl, P. Lalanne, and F. Lederer, "Light reflection and transmission at metamaterial interfaces and the consequences for homogenization," *Phys. Rev. B* **84**, 115142 (2011)
- [102] A. W. Snyder, and J. D. Love, "Optical waveguide theory," (Chapman & Hall, London, 1990) [ISBN: 0-412-09950-0]
- [103] P. Y. Chen, R. C. McPhedran, C. M. de Sterke, C. G. Poulton, A. A. Asatryan, L. C. Botten, and M. J. Steel, "Group velocity in lossy periodic structured media," *Phys. Rev. A* **82**, 053825 (2010)

- [104] L. C. Botten, M. S. Craig, R. C. McPhedran, J. L. Adams, and J. R. Andrewartha, "The Finitely Conducting Lamellar Diffraction Grating," *J. Mod. Opt.* **28**, 1087 - 1102 (1981)
- [105] P. C. Clemmow, "The plane wave spectrum representation of electromagnetic fields," (IEEE series on electromagnetic wave theory, NY, 1996) [ISBN: 0-7803-3411-6]
- [106] E. Istrate, and E. H. Sargent, "Photonic crystal heterostructures and interfaces" *Rev. Mod. Phys.* **78**, 455481 (2006)
- [107] P. St. J. Russell, "Optics of Floquet-Bloch Waves in Dielectric Gratings," *Appl. Phys. B* **39**, 231-246 (1986)
- [108] X. Yu, and S. Fan, "Anomalous reflections at photonic crystal surfaces" *Phys. Rev. E* **70**, 055601 (2004)
- [109] W. Jiang, R. T. Chen, and X. Lu, "Theory of light refraction at the surface of a photonic crystal," *Phys. Rev. B* **71**, 245115 (2005)
- [110] S. Foteinopoulou, and C. M. Soukoulis, "Electromagnetic wave propagation in two-dimensional photonic crystals: A study of anomalous refractive effects," *Phys. Rev. B* **72**, 165112 (2005)
- [111] B. Momeni, and A. Adibi, "An Approximate Effective Index Model for Efficient Analysis and Control of Beam Propagation Effects in Photonic Crystals," *J. Light-wave Technol.* **23**, 1522-1532 (2005)
- [112] T. Pertsch, T. Zentgraf, U. Peschel, A. Bräuer, and F. Lederer, "Anomalous Refraction and Diffraction in Discrete Optical Systems," *Phys. Rev. Lett.* **88**, 093901 (2002)
- [113] M. Born, and E. Wolf, "Principles of Optics," 7. (expanded) ed. (Cambridge Univ. Press, Cambridge, 1999) [ISBN: 0-521-64222-1]
- [114] G. Dolling, M. W. Klein, M. Wegener, Achim Schädle, Benjamin Kettner, Sven Burger, and Stefan Linden, "Negative beam displacements from negative-index photonic metamaterials," *Opt. Lett.* **32**, 14219-14227 (2007)
- [115] G. Dolling, M. Wegener, and S. Linden, "Realization of a three-functional-layer negative-index photonic metamaterial," *Opt. Lett.* **32**, 551-553 (2007)

- [116] C. García-Meca, J. Hurtado, J. Martí, A. Martínez, W. Dickson, and A. V. Zayats, "Low-Loss Multilayered Metamaterial Exhibiting a Negative Index of Refraction at Visible Wavelengths," *Phys. Rev. Lett.* **106**, 067402 (2011)
- [117] N. Liu, H. Guo, L. Fu, S. Kaiser, H. Schweizer, and H. Giessen, "Three-dimensional photonic metamaterials at optical frequencies," *Nature Mat.* **7**, 31-37 (2008)
- [118] M. S. Rill, C. Plet, M. Thiel, I. Staude, G. von Freymann, S. Linden, and M. Wegener, "Photonic metamaterials by direct laser writing and silver chemical vapour deposition," *Nat. Mat.* **7**, 543-546 (2008)
- [119] L. D. Landau, and E. M. Lifschitz, "Lehrbuch der theoretischen Physik," Vol. **8**: Elektrodynamik der Kontinua, in dt. Sprache hrsg. von Gerd Lehmann (Akademie Verlag, Berlin, 1985)
- [TP04] C. Menzel, T. Paul, C. Rockstuhl, T. Pertsch, S. Tretyakov, and F. Lederer, "Validity of effective material parameters for optical fishnet metamaterials," *Phys. Rev. B* **81**, 035320 (2010)
- [120] L. Jelinek, R. Marques, and J. Machac, "Fishnet Metamaterials – Rules for refraction and limits of homogenization," *Opt. Expr.* **18**, 17940-17949 (2010)
- [121] C. R. Simovski, "Material parameters of metamaterials (a Review)," *Optics and Spectroscopy* **107**, 726-753 (2009)
- [122] A. M. Nicholson, and G. F. Ross, "Measurement of the Intrinsic Properties of Materials by Time-Domain Techniques," *IEEE Trans. Instrum. Meas.* **19**, 377-382 (1970)
- [123] W. B. Weir, "Automatic measurement of complex dielectric constant and permeability at microwave frequencies," *Proc. of the IEEE*, **62**, 33-36 (1974)
- [124] D. R. Smith, S. Schultz, P. Markos, and C. M. Soukoulis, "Determination of effective permittivity and permeability of metamaterials from reflection and transmission coefficients," *Phys. Rev. B* **65**, 195104 (2002)
- [TP05] C. Menzel, C. Rockstuhl, T. Paul, and F. Lederer, "Retrieving effective parameters for metamaterials at oblique incidence," *Phys. Rev. B* **77**, 195328 (2008)
- [125] A. Andryieuski, R. Malureanu, and A. V. Lavrinenko, "Wave propagation retrieval method for metamaterials: Unambiguous restoration of effective parameters," *Phys. Rev. B* **80**, 193101 (2009)

- [126] D. R. Smith and J. B. Pendry, "Homogenization of metamaterials by field averaging (invited paper)," *J. Opt. Soc. Am. B* **23**, 391-403 (2006)
- [127] M. G. Silveirinha, "Metamaterial homogenization approach with application to the characterization of microstructured composites with negative parameters," *Phys. Rev. B* **75**, 115104 (2007)
- [128] M. G. Silveirinha, "Time domain homogenization of metamaterials," *Phys. Rev. B* **83**, 165104 (2011)
- [TP06] C. Rockstuhl, T. Paul, F. Lederer, T. Pertsch, T. Zentgraf, T. P. Meyrath, and H. Giessen "Transition from thin-film to bulk properties of metamaterials," *Phys. Rev. B* **77**, 035126 (2008)
- [129] D. Seetharamdoo, R. Sauleau, K. Mahdjoubi, and A.-C. Tarot, "Effective parameters of resonant negative refractive index metamaterials: Interpretation and validity," *J. Appl. Phys.* **98**, 063505 (2005)
- [130] H. Guo, N. Liu, L. Fu, H. Schweizer, S. Kaiser, and H. Giessen, "Thickness dependence of the optical properties of split-ring resonator metamaterials," *Phys. Stat. Sol. b* **244**, 1256-1261 (2007)
- [131] A. Minovich, D. N. Neshev, D. A. Powell, I. V. Shadrivov, M. Lapine, I. McKerracher, H. T. Hattori, H. H. Tan, C. Jagadish, and Y. S. Kivshar, "Tilted response of fishnet metamaterials at near-infrared optical wavelengths," *Phys. Rev. B* **81**, 115109 (2010)
- [132] C. Menzel, C. Helgert, J. Üpping, C. Rockstuhl, E.-B. Kley, R. B. Wehrspohn, T. Pertsch, and F. Lederer, "Angular resolved effective optical properties of a Swiss cross metamaterial," *Appl. Phys. Lett.* **95**, 131104 (2009)
- [133] C. Menzel, C. Rockstuhl, R. Iliew, F. Lederer, A. Andryieuski, R. Malureanu, and A. V. Lavrinenko, "High symmetry versus optical isotropy of a negative-index metamaterial" *Phys. Rev. B* **81**, 195123 (2010)
- [134] V. A. Markel, and J. C. Schotland, "On the sign of refraction in anisotropic non-magnetic media," *J. Opt.* **12**, 015104 (2010)
- [135] N. Wellander, and G. Kristensson, "Homogenization of the Maxwell Equations at Fixed Frequency," *SIAM J. on Appl. Math.* **64**, 170-195 (2003)

- [136] J. Zhou, Th. Koschny, M. Kafesaki, E. N. Economou, J. B. Pendry, and C. M. Soukoulis, "Saturation of the Magnetic Response of Split-Ring Resonators at Optical Frequencies," *Phys. Rev. Lett.* **95**, 223902 (2005)
- [137] V. M. Shalaev, "Optical negative-index metamaterials," *Nat. Photonics* **1**, 41-48 (2007)
- [138] C. M. Soukoulis, S. Linden, and M. Wegener, "Negative Refractive Index at Optical Wavelengths," *Science* **315** 47-49 (2007)
- [TP07] C. Rockstuhl, C. Menzel, T. Paul, T. Pertsch, and F. Lederer, "Light propagation in a fishnet metamaterial," *Phys. Rev. B* **78**, 155102 (2008)
- [TP08] C. Menzel, C. Rockstuhl, T. Paul, and F. Lederer, "Retrieving effective parameters for quasi-planar chiral metamaterials," *Appl. Phys. Lett.* **93**, 233106 (2008)
- [139] M. Davanço, Y. Urzhumov, and G. Shvets, "The complex Bloch bands of a 2D plasmonic crystal displaying isotropic negative refraction," *Opt. Expr.* **15**, 9681-9691 (2007)
- [140] X. Zhang, M. Davanço, Y. Urzhumov, G. Shvets, and S. R. Forrest, "From Scattering Parameters to Snells Law: A Subwavelength Near-Infrared Negative-Index Metamaterial," *Phys. Rev. Lett.* **101**, 267401 (2008)
- [TP09] T. Paul, C. Rockstuhl, C. Menzel, and F. Lederer, "Anomalous refraction, diffraction, and imaging in metamaterials," *Phys. Rev. B* **79**, 115430 (2009)
- [TP10] T. Paul, C. Rockstuhl, C. Menzel, and F. Lederer, "Advanced Optical Metamaterials," *Advanced Materials* **22**, 23542357 (2010)
- [141] C. Menzel, "Characterization of Optical Metamaterials – Effective Parameters and Beyond," *Dissertation thesis*, Friedrich-Schiller-Universität Jena, 2011
- [142] S. Zhang, W. Fan, K. J. Malloy, S.R. Brueck, N. C. Panoiu, and R. M. Osgood, "Near-infrared double negative metamaterials," *Opt. Expr.* **13**, 4922-4930 (2005)
- [143] S. Zhang, W. Fan, N. C. Panoiu, K. J. Malloy, R. M. Osgood, and S. R. J. Brueck, "Experimental Demonstration of Near-Infrared Negative-Index Metamaterials," *Phys. Rev. Lett.* **95**, 137404 (2005)
- [144] D. J. Cho, F. Wang, X. Zhang, and Y. R. Shen, "Contribution of the electric quadrupole resonance in optical metamaterials," *Phys. Rev. B* **78**, 121101 (2008)

- [145] Na Liu, Liwei Fu, Stefan Kaiser, Heinz Schweizer, and Harald Giessen, "Plasmonic Building Blocks for Magnetic Molecules in Three-Dimensional Optical Metamaterials," *Advanced Materials* **20**, 38593865 (2008)
- [146] J. Petschulat, C. Menzel, A. Chipouline, C. Rockstuhl, A. Tünnermann, F. Lederer, and T. Pertsch, "Multipole approach to metamaterials," *Phys. Rev. A* **78**, 043811 (2008)
- [147] A. Chipouline, J. Petschulat, A. Tuennermann, T. Pertsch, C. Menzel, C. Rockstuhl, and F. Lederer, "Multipole approach in electrodynamics of metamaterials," *Appl. Phys. A: Materials Science & Processing*, DOI: 10.1007/s00339-011-6339-7 (2011)
- [148] C. García-Meca, R. Ortuño, F. J. Rodríguez-Fortuño, J. Martí, and A. Martínez, "Double-negative polarization-independent fishnet metamaterial in the visible spectrum," *Opt. Lett.* **34**, 1603-1605 (2009)
- [149] C. Helgert, C. Menzel, C. Rockstuhl, E. Pshenay-Severin, E.-B. Kley, A. Chipouline, A. Tünnermann, F. Lederer, and T. Pertsch, "Polarization-independent negative-index metamaterial in the near infrared," *Opt. Lett.* **34**, 704-706 (2009)
- [150] G. Dolling, C. Enkrich, M. Wegener, C. M. Soukoulis, and S. Linden, "Low-loss negative-index metamaterial at telecommunication wavelengths," *Opt. Lett.* **31**, 1800-1802 (2006)
- [151] C. Luo, S. G. Johnson, J. D. Joannopoulos, and J. B. Pendry, "Subwavelength imaging in photonic crystals," *Phys. Rev. B* **68**, 045115 (2003)
- [152] R. Iliew, C. Etrich, and F. Lederer, "Self-collimation of light in three-dimensional photonic crystals," *oe***13**, 7076-7085 (2005)
- [153] P. T. Rakich, M. S. Dahlem, S. Tandon, M. Ibanescu, M. Soljacić, G. S. Petrich, J. D. Joannopoulos, L. A. Kolodziejski, and E. P. Ippen, "Achieving centimetre-scale supercollimation in a large-area two-dimensional photonic crystal," *Nat. Mat.* **5**, 93-96 (2006)
- [154] C. Luo, S. G. Johnson, J. D. Joannopoulos, and J. B. Pendry, "All-angle negative refraction without negative effective index," *Phys. Rev. B* **65**, 201104(R) (2002)
- [155] E. Cubukcu, K. Aydin, E. Ozbay, S. Foteinopoulou, and C. M. Soukoulis, "Electromagnetic waves: Negative refraction by photonic crystals," *Nature* **423**, 604-605 (2003)

- [156] G. P. Agrawal, "Nonlinear fiber optics," 4th ed. (Elsevier/Acad. Press, Amsterdam [u.a.], 2007)
- [157] F. Goos, and H. Hänchen, "Ein neuer und fundamentaler Versuch zur Totalreflexion," *Ann. d. Physik* **436**, 333346 (1947)
- [158] C. Imbert, "L'effet inertial de spin du photon Théorie et preuve expérimentale," *Nouv. Rev. Opt. Appl.* **3**, 199-208 (1972).
- [159] C. Imbert, "Calculation and Experimental Proof of the Transverse Shift Induced by Total Internal Reflection of a Circularly Polarized Light Beam," *Phys. Rev. D* **5**, 787796 (1972).
- [160] T. F. Coleman, and Y. Li, "An Interior Trust Region Approach for Nonlinear Minimization Subject to Bounds ," *SIAM J. Optim.* **6**, 418-445 (1996)
- [161] MathWorks: MATLAB, <http://www.mathworks.de/products/matlab/> (online resource, visited at 09/09/2011)
- [162] P. Lalanne, and J. P. Hugonin, "Bloch-wave engineering for high-Q, small-V microcavities," *IEEE J. of Quant. Electr.* **39**, 1430-1438 (2003)
- [163] C. R. Simovski and S. A. Tretyakov, "Local constitutive parameters of metamaterials from an effective-medium perspective" *Phys. Rev. B* **75**, 195111 (2007)
- [164] C. R. Simovski, "Bloch material parameters of magneto-dielectric metamaterials and the concept of Bloch lattices," *Metamaterials* **1**, 62-80 (2007)
- [165] M. Buresi, D. Diessel, D. van Oosten, S. Linden, M. Wegener, and L. Kuipers, "Negative-Index Metamaterials: Looking into the Unit Cell," *Nano Lett.* **10**, 2480-2483 (2010)
- [166] J. Qi, H. Kettunen, H. Wallén, and A. Sihvola, "Compensation of FabryPérot Resonances in Homogenization of Dielectric Composites," *IEEE Ant. and Wireless Prop. Lett.* **9**, 1057-1060 (2010)
- [167] A. K. Popov, and V. M. Shalaev, "Merging Nonlinear Optics and Negative-Index Metamaterials," *arXiv:1108.0867v1* (2011)
- [168] V. Roppo, M. Centini, C. Sibilìa, M. Bertolotti, D. de Ceglia, M. Scalora, N. Akozbek, Mark J. Bloemer, Joseph W. Haus, O. G. Kosareva, and V. P. Kandidov, "Role of phase matching in pulsed second-harmonic generation: Walk-off and phase-locked twin pulses in negative-index media" *Phys. Rev. A* **76**, 033829 (2007)

- [169] V. Roppo, C. Ciraci, C. Cojocaru, and M. Scalora, "Second harmonic generation in a generic negative index medium," *J. Opt. Soc. Am. B* **27**, 1671-1679 (2010)
- [170] D. de Ceglia, A. D'Orazio, M. De Sario, V. Petruzzelli, F. Prudenzano, M. Centini, M. G. Cappeddu, M. J. Bloemer, and M. Scalora "Enhancement and inhibition of second-harmonic generation and absorption in a negative index cavity," *Opt. Lett.* **32**, 265-267 (2007)
- [171] M. W. Klein, C. Enkrich, M. Wegener, and S. Linden, "Second-Harmonic Generation from Magnetic Metamaterials," *Science* **313**, 502-504 (2006)
- [172] M. W. Klein, N. Feth, M. Wegener, and S. Linden, "Experiments on second- and third-harmonic generation from magnetic metamaterials," *Opt. Exp.* **15**, 5238-5247 (2007)
- [173] E. Kim, F. Wang, W. Wu, Z. Yu, and Y. R. Shen, "Nonlinear optical spectroscopy of photonic metamaterials," *Phys. Rev. B* **78**, 113102 (2008)
- [174] W. Fan, S. Zhang, N.-C. Panoiu, A. Abdenour, S. Krishna, R. M. Osgood, Jr., K. J. Malloy, and S. R. J. Brueck, "Second Harmonic Generation from a Nanopatterned Isotropic Nonlinear Material," *Nano Letters* **6**, 1027-1030 (2006)
- [175] F. B. P. Niesler, N. Feth, S. Linden, J. Niegemann, J. Gieseler, K. Busch, and M. Wegener, "Second-harmonic generation from split-ring resonators on a GaAs substrate," *Opt. Lett.* **34**, 1997-1999 (2009)
- [176] B. K. Canfield, H. Husu, J. Laukkanen, B. Bai, M. Kuittinen, J. Turunen, and M. Kauranen, "Local Field Asymmetry Drives Second-Harmonic Generation in Non-centrosymmetric Nanodimers," *Nano Letters* **7**, 1251-1255 (2007)
- [177] B. K. Canfield, S. Kujala, K. Jefimovs, T. Vallius, J. Turunen, and M. Kauranen, "Polarization effects in the linear and nonlinear optical responses of gold nanoparticle arrays," *J. Opt. A: Pure Appl. Opt.* **7**, 110-117 (2005)
- [178] Y. Zeng, W. Hoyer, J. Liu, S. W. Koch, and J. V. Moloney, "Classical theory for second-harmonic generation from metallic nanoparticles," *Phys. Rev. B* **79**, 235109 (2009)
- [TP11] T. Paul, C. Rockstuhl, and F. Lederer, "Integrating cold plasma equations into the Fourier modal method to analyze second harmonic generation at metallic nanostructures," *J. Mod. Opt.* **58** 438-448 (2011)

- [TP12] T. Utikal, T. Zentgraf, T. Paul, C. Rockstuhl, F. Lederer, M. Lippitz, and H. Giessen, "Towards the Origin of the Nonlinear Response in Hybrid Plasmonic Systems," *Phys. Rev. Lett.* **106**, 133901 (2011)
- [179] C. K. Chen, A. R. B. de Castro, and Y. R. Shen, "Surface-Enhanced Second-Harmonic Generation," *Phys. Rev. Lett.* **46**, 145-148 (1981).
- [180] C. K. Chen, T. F. Heinz, D. Ricard, and Y. R. Shen, "Surface-enhanced second-harmonic generation and Raman scattering," *Phys. Rev. B* **27**, 1965-1979 (1983).
- [181] G. T. Boyd, Th. Rasing, J. R. R. Leite, and Y. R. Shen, "Local-field enhancement on rough surfaces of metals, semimetals, and semiconductors with the use of optical second-harmonic generation," *Phys. Rev. B* **30**, 519-526 (1984).
- [182] C. G. Biris, and N. C. Panoiu, "Second harmonic generation in metamaterials based on homogeneous centrosymmetric nanowires," *Phys. Rev. B* **81**, 195102 (2010)
- [183] M. F. Saleh, L. Dal Negro, and B. E. Saleh, "Second-order parametric interactions in 1-D photonic-crystal microcavity structures," *Opt. Exp.* **16**, 5261-5276 (2008)
- [184] M. Cherchi, "Exact analytic expressions for electromagnetic propagation and optical nonlinear generation in finite one-dimensional periodic multilayers," *Phys. Rev. E* **69**, 066602 (2004)
- [185] L. Cao, N. C. Panoiu, R. D. R. Bhat, and R. M. Osgood, Jr., "Surface second-harmonic generation from scattering of surface plasmon polaritons from radially symmetric nanostructures," *Phys. Rev. B* **79**, 235416 (2009)
- [186] M. Nevière, P. Vincent, D. Maystre, R. Reinisch, and J. L. Coutaz, "Differential theory for metallic gratings in nonlinear optics: second-harmonic generation," *J. Opt. Soc. Am. B* **5**, 330-337 (1988)
- [187] R. Reinisch, and M. Nevière, "Electromagnetic theory of diffraction in nonlinear optics and surface-enhanced nonlinear optical effects," *Phys. Rev. B* **28**, 1870 (1983)
- [188] D. Maystre, M. Nevière, R. Reinisch, and J. L. Coutaz, "Integral theory for metallic gratings in nonlinear optics and comparison with experimental results on second-harmonic generation," *J. Opt. Soc. Am. B* **5**, 338-346 (1988)
- [189] W. Nakagawa, R.-C. Tyan, and Y. Fainman, "Analysis of enhanced second-harmonic generation in periodic nanostructures using modified rigorous coupled-wave analysis in the undepleted-pump approximation," *J. Opt. Soc. Am. A* **19**, 1919-1928 (2002)

- [190] B. Bai, and J. Turunen, "Fourier modal method for the analysis of second-harmonic generation in two-dimensionally periodic structures containing anisotropic materials," *J. Opt. Soc. Am. B* **24**, 1105-1112 (2007)
- [TP13] T. Paul, C. Rockstuhl, and F. Lederer, "A numerical approach for analyzing higher harmonic generation in multilayer nanostructures," *J. Opt. Soc. Am. B* **27**, 1118-1130 (2010)
- [191] R. W. Boyd, "Nonlinear Optics," 2nd ed., (Academic Press, Amsterdam, 2003)
- [192] N. Bonod, E. Popov, and M. Neviere, "Fourier factorization of nonlinear Maxwell equations in periodic media: application to the optical Kerr effect," *Opt. Comm.* **244**, 389-398 (2005)
- [193] N. Bloembergen, R. K. Chang, S. S. Jha, and C. H. Lee, "Optical Second-Harmonic Generation in Reflection from Media with Inversion Symmetry," *Phys. Rev.* **174**, 813-822 (1968)
- [194] J. E. Sipe, D. J. Moss, and H. M. van Driel, "Phenomenological theory of optical second- and third-harmonic generation from cubic centrosymmetric crystals," *Phys. Rev. B* **35**, 1129-1141 (1987)
- [195] G. Auer, K. Sauer, and K. Baumgärtel, "Second-Harmonic Emission at Resonance Absorption," *Phys. Rev. Lett.* **42**, 1744-1746 (1979)
- [196] K. Baumgärtel, and K. Sauer, "Topics on Nonlinear Wave-plasma Interaction, Vol. 4" (Akademie-Verlag: Physical Research, Berlin, 1987)
- [197] S. Linden, J. Kuhl, and H. Giessen, "Controlling the Interaction between Light and Gold Nanoparticles: Selective Suppression of Extinction," *Phys. Rev. Lett.* **86**, 46884691 (2001)
- [198] A. Christ, S. G. Tikhodeev, N. A. Gippius, J. Kuhl, and H. Giessen, "Waveguide-Plasmon Polaritons: Strong Coupling of Photonic and Electronic Resonances in a Metallic Photonic Crystal Slab," *Phys. Rev. Lett.* **91**, 183901 (2003)
- [199] A. Christ, T. Zentgraf, J. Kuhl, S. G. Tikhodeev, N. A. Gippius, and H. Giessen, "Optical properties of planar metallic photonic crystal structures: Experiment and theory," *Phys. Rev. B* **70**, 125113 (2004)

- [200] J. Jerphagnon, S. K. Kurtz, J.-L. Oudar, "Nonlinear dielectric susceptibilities" in *Landolt-Börnstein: Numerical data and functional relationships in science and technology: new series, Vol. 18: Elastic, piezoelectric, pyroelectric, piezooptic, electrooptic constants, and nonlinear dielectric susceptibilities of crystals*, O. Madelung, ed.-in-chief, (Springer, Berlin [u.a.], 1984), pp. 456-506 [ISBN: 3-540-12101-3]
- [201] N. Ueda, H. Kawazoe, Y. Watanabe, M. Takata, M. Yamane, and Kenichi Kubodera, "Third-order nonlinear optical susceptibilities of electroconductive oxide thin films," *Appl. Phys. Lett.* **59**, 502-503 (1991)
- [202] Y. Watanabe, M. Sakai, M. Takata, N. Ueda, and H. Kawazoe, "Third order nonlinear optical susceptibility for transparent tin oxide thin films," *Ferroelectrics* **131**, 111-117 (1992).
- [203] U. Gubler, and C. Bosshard, "Optical third-harmonic generation of fused silica in gas atmosphere: Absolute value of the third-order nonlinear optical susceptibility $\chi^{(3)}$," *Phys. Rev. B* **61**, 10702-10710 (2000)
- [204] T. Hanke, G. Krauss, D. Träutlein, B. Wild, R. Bratschitsch, and A. Leitenstorfer, "Efficient Nonlinear Light Emission of Single Gold Optical Antennas Driven by Few-Cycle Near-Infrared Pulses," *Phys. Rev. Lett.* **103**, 257404 (2009)
- [205] M. Wand, A. Schindlmayr, T. Meier, J. Förstner, "Simulation of the ultrafast nonlinear optical response of metal slabs," *Phys. Stat. Sol. b* **248**, 887-891 (2011)
- [206] P. B. Johnson and R. W. Christy, "Optical Constants of the Noble Metals," *Phys. Rev. B* **6**, 4370 (1972).
- [207] R. S. Weis, T. K. Gaylord, "Lithium Niobate: Summary of Physical Properties and Crystal Structure," *Appl. Phys. A: Mat. Science & Processing* **37**, 191-203 (1985)